



**HAL**  
open science

# Metallic Nanostructure W-shaped for Nano-optic and Numerical Simulation of Tandem Solar Cells on Silicon

Shijian Wang

► **To cite this version:**

Shijian Wang. Metallic Nanostructure W-shaped for Nano-optic and Numerical Simulation of Tandem Solar Cells on Silicon. Micro and nanotechnologies/Microelectronics. Université de Technologie de Troyes, 2019. English. NNT : 2019TROY0015 . tel-03618862

**HAL Id: tel-03618862**

**<https://theses.hal.science/tel-03618862>**

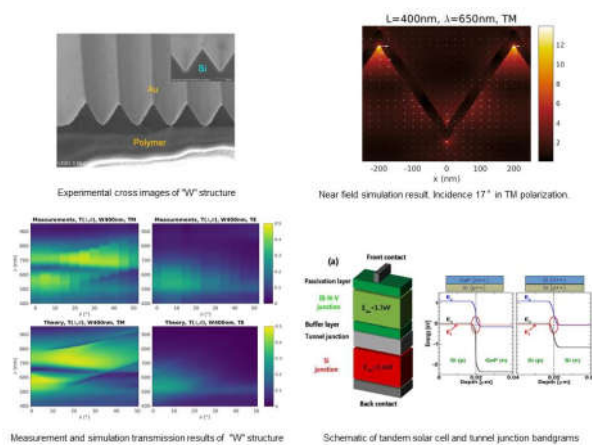
Submitted on 24 Mar 2022

**HAL** is a multi-disciplinary open access archive for the deposit and dissemination of scientific research documents, whether they are published or not. The documents may come from teaching and research institutions in France or abroad, or from public or private research centers.

L'archive ouverte pluridisciplinaire **HAL**, est destinée au dépôt et à la diffusion de documents scientifiques de niveau recherche, publiés ou non, émanant des établissements d'enseignement et de recherche français ou étrangers, des laboratoires publics ou privés.

**Shijian WANG**

# Metallic Nanostructure W-shaped for Nano-optic and Numerical Simulation of Tandem Solar Cells on Silicon



**Champ disciplinaire :**  
**Sciences pour l'Ingénieur**

2019TROY0015

Année 2019

---

---

THESE

*pour l'obtention du grade de*

DOCTEUR

de l'UNIVERSITE DE TECHNOLOGIE DE TROYES

EN SCIENCES POUR L'INGENIEUR

**Spécialité : MATERIAUX, MECANIQUE, OPTIQUE, NANOTECHNOLOGIE**

*présentée et soutenue par*

**Shijian WANG**

*le 13 juin 2019*

---

---

**Metallic Nanostructure W-shaped for Nano-optic and  
Numerical Simulation of Tandem Solar Cells on Silicon**

---

---

JURY

M. P.-M. ADAM	PROFESSEUR DES UNIVERSITES	Président
M. J. CONNOLLY	CHERCHEUR - HDR	Rapporteur
M. A. MORAND	MAITRE DE CONFERENCES - HDR	Rapporteur
Mme Y. SUN	ASSOCIATE PROFESSOR	Examinatrice
M. A. ROLLAND	PROFESSEUR DES UNIVERSITES	Directeur de thèse
M. R. VINCENT	PROFESSEUR ASSOCIE	Directeur de thèse

Personnalités invitées

M. A. BRUYANT	MAITRE DE CONFERENCES - HDR
M. C. BRYLINSKI	PROFESSEUR DES UNIVERSITES



## Contents

Chapter 1 Plasmonic : Periodic W-shaped metallic nanostructure .....	1
1.1 Surface plasmons .....	1
1.2 Modelisation of LSP for metallic nanospheres.....	4
1.2.1 Quasi-static approximation .....	5
1.2.2 Mie theory.....	6
1.3 Energy decay of Localized surface plasmons.....	7
1.4 Influence of factors on LSPR .....	8
1.4.1 Influence of Nanoparticle material on LSPR.....	8
1.4.2 Influence of Nanoparticle shape and size on LSPR .....	8
1.4.3 Influence of interparticle spacing on LSPR.....	10
1.4.4 Influence of substrate on LSPR .....	11
1.4.5 Influence of dielectric environment on LSPR .....	11
1.5 Applications of LSPR.....	12
1.5.1 Photovoltaic devices.....	12
1.5.2 Biosensor .....	14
1.5.3 Surface-enhanced Raman spectroscopy .....	15
1.6 Origin and motivation of "W" structure.....	16
1.7 Primary "W" structure research simulation.....	18
1.8 Summary .....	19
1.9 Introduction of the chapters.....	20
Chapter 2 Experiment.....	21
2.1 W-structure mold fabrication.....	22
2.1.1 Principle of W-structure forming process .....	22
2.1.2 Fabrication of W-structure .....	23
2.2 Influence of BHF etching time .....	27
2.3 Influence factors of etching results .....	29
2.4 Sample alignment methods .....	32
2.4.1 CRM .....	32
2.4.2 ERM .....	35
2.5 Final W-structure mold .....	36
2.6 Metallic W-structure fabrication.....	38
2.8 Summary .....	42
Chapter 3 Optical properties of the 2D-folded metallic nanolayers.....	44
3.1 Introduction .....	44
3.2 Description of the electromagnetic modeling methods.....	45
3.2.1 Properties of the electromagnetic field in periodic media .....	45
3.2.2 Differential method .....	47

3.2.3 Chandezon method.....	48
3.3 Measurements of light transmission through the W-structure in the visible range.....	49
3.3.1 Description of the measurement setup .....	49
3.3.2 Description of the experimental results .....	50
3.4 Far field properties of the gold W-structures obtained by electromagnetic modeling.....	54
3.4.1 Effect of the existence of diffraction orders on the variation of the absorption, reflection and transmission coefficients.....	55
3.4.2 Repartition of the energy between the diffraction orders .....	58
3.5 Local field properties of the gold W-structures obtained by electromagnetic modeling.....	61
3.5.1 Identification of the wavelengths and angles of incidence of interest	62
3.5.2 Theory of wedge resonances.....	64
3.5.3 Local fields in the W-400nm and W-600nm gold nanostructures.....	65
3.6 Conclusion.....	66
Annex.....	69
Chapter 4 Numerical simulation of tandem solar cells on silicon .....	70
4.1 Background.....	70
4.2 Solar cell principle .....	74
4.3 Tandem solar cell structure.....	81
4.4 Solar cell numerical simulation tool .....	83
4.5 Influence of GaAsPN absorbing layer thickness .....	88
4.6 Influence of band offset.....	90
4.7 Study of top cell EQE .....	94
4.8 Study of tunnel junction .....	97
4.9 Tandem solar cell simulation .....	100
4.10 Fitting experimental results .....	101
4.11 Conclusion .....	103
Annex.....	104
Conclusions.....	105
French summary.....	107
Chapitre 1 Plasmonics: Nanostructure métallique en forme de W .....	107
1.1 Plasmons de surface .....	107
1.2 Désintégration d'énergie des plasmons de surface localisés .....	108
1.3 Influence des facteurs sur la LSPR .....	109
1.4 Applications de LSPR .....	109
1.5 Origine et motivation de la structure "W" .....	109
1.6 Simulation de recherche de structure primaire "W" .....	110
Chapitre 2 Expérience .....	112
2.1 Principe du processus de formation de la structure en "W" .....	112
2.2 Fabrication de la structure en "W" .....	113

2.3	Modèle de structure "W" final.....	114
2.4	Fabrication de structures métalliques "W" .....	116
Chapitre 3	Propriétés optiques des nanocouches métalliques pliées en 2D .....	118
3.1	Description des résultats expérimentaux.....	118
3.2	Effet de l'existence d'ordres de diffraction sur la variation des coefficients d'absorption, de réflexion et de transmission .....	120
3.3	Propriétés du champ local des structures en or W obtenues par modélisation électromagnétique.....	122
Chapitre 4	Simulation numérique de cellules solaires tandem sur silicium .....	124
4.1	Structure de cellule solaire tandem .....	124
4.2	Outil de simulation numérique de cellules solaires .....	126
4.3	Influence de l'épaisseur de la couche absorbante de GaAsPN .....	127
4.5	Influence du décalage de bande .....	127
4.6	Etude d'EQE de cellules supérieures.....	129
4.7	Etude de jonction tunnel.....	131
4.8	Simulation de cellules solaires en tandem et ajustement des résultats expérimentaux .....	132
Reference	.....	134

# **Chapter 1 Plasmonic : Periodic W-shaped metallic nanostructure**

The significant feature of metallic nanoparticle is well-known as localized surface plasmon resonance (LSPR), meanwhile the use of devices based on this optical phenomenon and the interest of study in this field keep increasing due to their prominent sensitivities and other significant optical performance, such as near-field enhancement, selected light absorption and scattering, strongly depending on metal nanoparticles size, shape, local dielectric environment.<sup>1-3</sup> Especially, its utilization in chemistry and biology fields for real-time<sup>4,5</sup>, label-free samples analysis<sup>6-8</sup> is attracting more and more interests. In addition, with the development of nanofabrication technologies and in order to meet specific application demands, various size, shape and material devices can be fabricated. What's more, owing to its potential applications, the attention payed in this field becomes more and more. In the following, we will introduce some fundamental aspects of plasmonics.

## **1.1 Surface plasmons**

Surface plasmons, one of the greatest branches of nanophotonics, is an optical phenomenon generated from collective electrons oscillation when the incident electromagnetic act at metal surface. As normal, the collective oscillation of surface electrons in metal conduction band appears while the electrons interact with the incident electromagnetic field, meanwhile under the restoring force of the nuclei, the oscillating electrons return. When the incident electromagnetic has the same phase and frequency as the oscillated wave, the resonance occurs and the field of plasma wave field reaches amplification.

As the incident light can penetrate into metallic materials, but the depth is limited, therefore only a fraction of plasmons at surface are named as surface plasmons. Surface

plasmons have two main categories: one class is that the metal surface is flat and long range, and the plasma wave can propagate along metal surface for few hundred micrometers as shown in Figure 1.1a, and this kind of surface plasmons is always called surface plasmon polaritons (SPPs); The other class is that the metal is nanoparticle whose size is smaller than the incident light wavelength. This case of surface plasmons is often named localized surface plasmons (LSP) as shown in Figure 1. 1b.

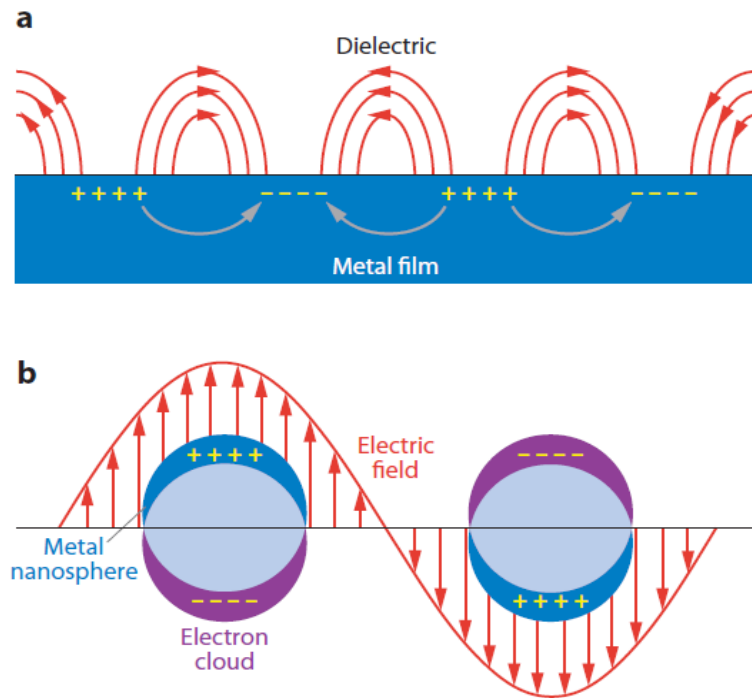


Figure 1.1. (a) Propagating surface plasmons at metal/dielectric surface; (b) localized surface plasmons of a metallic nanoparticle.<sup>9</sup>

As illustrated in Figure 1.1a, SPPs exist at the planar interface forming by two different mediums with opposite signs dielectric constants. As normal, a metal and a dielectric are used to play as the roles. By solving Maxwell's equations, it is confirmed that only under TM polarization can excite the surface modes at the interface. However, when TE polarization acts at interface, no surface modes can be excited. Under the former condition, the surface plasma wave (SPW) propagation constant  $\kappa_{SP}$  is given by following equation:

$$\kappa_{SP} = \kappa \sqrt{\frac{\epsilon_m \epsilon_d}{\epsilon_m + \epsilon_d}} \quad 1-1$$

Where  $\kappa$ : light wave vector,  $\epsilon_m$ : metal relative permittivity,  $\epsilon_d$ : dielectric

relative permittivity

From the equation, it is obvious that SPW propagation constant is bigger than propagation constant of optical wave in dielectric. That means the SPPs can't be excited directly by incident electromagnetic.

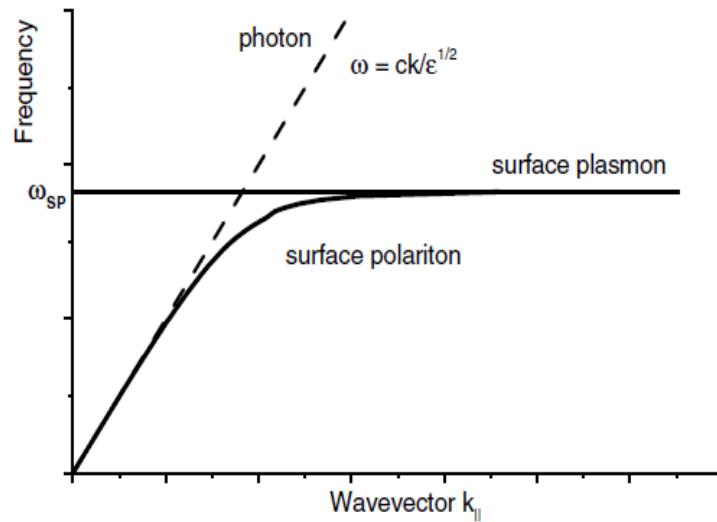


Figure 1.2. Dispersion of surface plasmon polaritons on metal surface. Dash and solid lines are light and surface plasmon dispersions separately.<sup>10</sup>

Therefore, in order to match the SPW propagation constant, incident optical wave propagation constant should to be enhanced. To achieve this goal, a set of methods, including attenuated prism coupling, grating coupling and near-field excitation are adopted to serve it.<sup>11-14</sup>

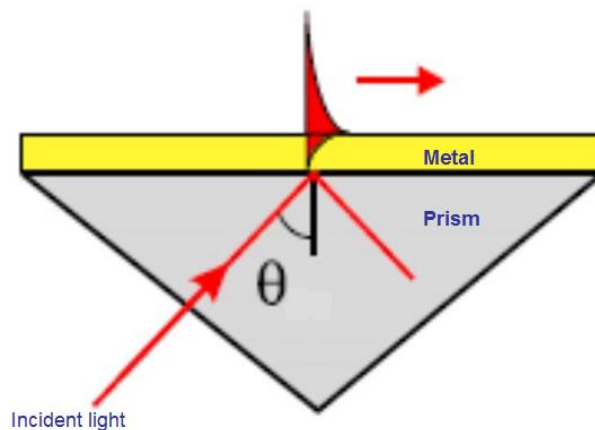


Figure 1.3. Kretschmann configuration geometry.<sup>11</sup>

Just like in Kretschmann configuration, when the incident light angle is greater than the angle of total internal reflection, the light power does not reflect immediately. It can

penetrate into metal for a distance. Under this situation, the light vector  $\kappa_i$  can be expressed as :

$$\kappa_i = \frac{\omega}{c} \sqrt{\varepsilon_{prism}} \sin \theta \quad 1-2$$

Through change the incident angle, when  $\kappa_i$  equals to  $\kappa_{SP}$ , the resonance conditions can be satisfied, and the resonance appears. As a result, the corresponding incident wavelength is absorbed or scattered, the electromagnetic field is enhanced and it is observed in the reflectivity as a minimum value at the corresponding incident wavelength position.

Besides above, SPW has another important feature. When SPW propagates along the interface, at the same time, in out-plane direction, the power exponential decays into metal and dielectric materials. Since metal dielectric constant is always bigger than dielectric permittivity, so the penetration depth in dielectric is longer than that in metal.

In contrast to SPPs, LSP does not need auxiliary accessories, just like prism, to match wave number and frequency. It can be excited directly by incident light. For this kind of SP, the light wavelength is always larger than metallic particle size. But due to the nanoparticle properties, the penetration depth is not as long as SPPs.

Anyway, for these two kinds of surface plasmon, when the resonance conditions are satisfied, the electric fields are enhanced, meantime the corresponding lights are absorbed or scattered strongly. These properties are the resource of their applications. In my thesis, my main work majors in LSP field, so in the following texts, we just tend to pay attention to this branch.

## **1.2 Modelisation of LSP for metallic nanospheres**

Up to now, for analyzing the interaction between spherical metallic particle and electromagnetic field, two analytical models are available: the quasi-static approximation and Mie Theory, before they are developed, humans are puzzled by the optical phenomenon for many centuries. Especially to Mie theory, it is most used to

analyze and explain the results of metallic nanospheres which sizes are similar or bigger than incident wavelength. In the following sections, we will describe simply these two models. They can help us to understand about the metallic nanoparticles properties, and explain the experimental results.

### 1.2.1 Quasi-static approximation

In this model, the metallic particle size is treated as an isotropic sphere with radius  $a$ , much smaller than the incident wavelength, and the surrounding medium dielectric constant is  $\epsilon_d$  (without absorption), meanwhile the electromagnetic field  $E_0$  is constant in space. All of them are shown in the Figure 1.4.

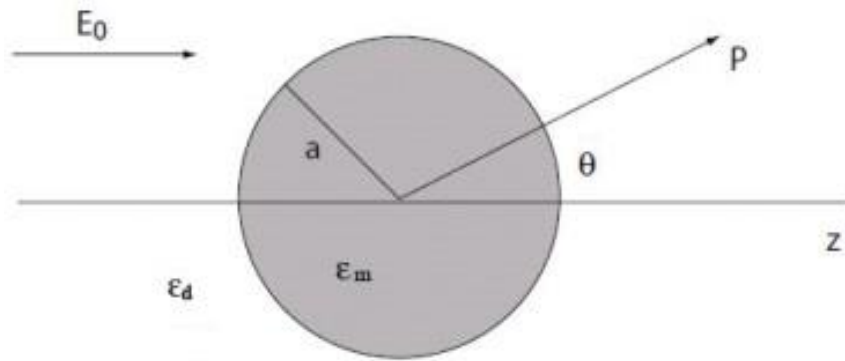


Figure 1.4. Sketch of a homogeneous sphere in electrostatic field.<sup>15</sup>

The spatial potential in electromagnetic field can be got through solving Laplace equation

$$\nabla^2\Phi = 0 \quad 1-3$$

And from which, the electric field can be described as

$$E_0 = -\nabla\Phi \quad 1-4$$

Finally, considering the boundary conditions of metallic sphere, the particle inside potential  $\Phi_{in}$  and outside potential  $\Phi_{out}$ , through solving the precedent Laplace equation, they can be obtained as

$$\Phi_{in} = -\frac{3\epsilon_d}{\epsilon+2\epsilon_d}E_0r\cos\theta \quad 1-5$$

$$\Phi_{out} = -E_0r\cos\theta + \frac{\epsilon-\epsilon_d}{\epsilon+2\epsilon_d}E_0a^3\frac{\cos\theta}{r^2} \quad 1-6$$

As  $\Phi_{\text{out}}$  describes the superposition of particle center dipole field and applied field, so it can be written in new form by introducing dipole moment P

$$\Phi_{\text{out}} = -E_0 r \cos\theta + \frac{P \cdot r}{4\pi\epsilon_0\epsilon_d r^3} \quad 1-7$$

$$P = 4\pi\epsilon_0\epsilon_d a^3 \frac{\epsilon - \epsilon_d}{\epsilon + 2\epsilon_d} E_0 \quad 1-8$$

From the above equations, we can see that a dipole moment is induced by the outside applied field, and scales with  $|E_0|$ . Introducing the polarizability  $\alpha$ , with  $P = \epsilon_0\epsilon_d\alpha E_0$ , then we obtain

$$\alpha = 4\pi a^3 \frac{\epsilon - \epsilon_d}{\epsilon + 2\epsilon_d} \quad 1-9$$

When polarizability  $\alpha$  reaches the maximum value, the resonant enhancement emerges. That requires  $|\epsilon + 2\epsilon_d|$  is a minimum, for the case of  $\text{Im}[\epsilon]$  changes slowly or small, it can be simplified to

$$\text{Re}[\epsilon_m] = -2\epsilon_d \quad 1-10$$

## 1.2.2 Mie theory

As you can see, when quasi-static approximation is applied, the particle is supposed to be small enough compared to the incident wavelength. But for larger particles size, this model is not relevant. Other new analyze methods are needed. In 1908, in order to explain optical properties of relative larger nanoparticles, Mie proposed a theory for metallic sphere, through solving Maxwell's equations<sup>16-18</sup>, now it is well known as Mie theory.

In practice, the nanoparticles are not always nanospheres at all. The extinction spectrum depends on out-of-plane height, in-plane diameter and shape of the nanoparticle. Besides of these, a set of elements act on extinction spectrum, and they will be referred in the next section as many as possible.

Even Mie theory can offer us a right, simple and systematic way to analyze nanosphere, also it is useful for ellipsoidal nanoparticle.<sup>19</sup> But for other geometrical

nanoparticles(triangles, nanorods, stars, etc.), it is not feasible. In terms of this situation, finite difference time domain (FDTD),<sup>20</sup> discrete dipole approximation(DDA),<sup>21</sup> multiple multipole,<sup>22</sup> and T-matrix<sup>23</sup> are developed for modeling. But that does not mean Mie theory is no meaning to us, it is still important and possesses a simple description in mathematical terms. Because Mie theory is analytical it allows interpreting Maxwell's equations for spherical particles embedding in an environment. In addition to that, in some nanofabrication process, the particles are approximate to spheres, this models also can be applied for analyzing their according properties.

### 1.3 Energy decay of Localized surface plasmons

Localized surface plasmons energy decays through mainly three processes: radiative decay, non-radiative decay (absorption) and dynamic depolarization decay. The first two processes are shown in Figure 1.5.

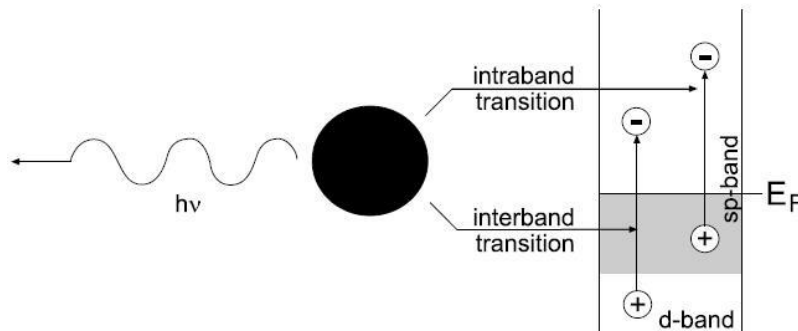


Figure 1.5. Radiative and non-radiative decay of particle plasmons.<sup>15</sup>

Radiative decay is a route of particle plasmon transformation into photons, and it takes the main decay proportion for large volume nanoparticles.<sup>24, 25</sup> Non-radiative decay process arises from the creation of electron-hole pairs via either intraband excitation in the conduction band or interband transitions from low energy band to high band.<sup>26</sup> This process is normal light absorption, so accompanying photons transition and heat generation. When the metallic nanoparticle's volume is small, but the surface/volume ratio of them can't be negligible, non-radiative is the main decay mechanism.<sup>27</sup> Dynamic depolarization decay is due to the scattering of collision surface plasmons, and that makes energy lose. And with the radius of metallic

nanoparticles increase, the more energy loses. And meantime, that causes redshift of plasmon resonance.<sup>28, 29</sup>

## **1.4 Influence of factors on LSPR**

Analyze of Mie theory model tells us that various factors have influence over the LSPR response. Like nanoparticle material, size, shape, surrounding environment and spacing of nanoparticles. And for each case, simple summary research results are cited in the coming text.

### **1.4.1 Influence of Nanoparticle material on LSPR**

Due to prominent field enhancement causing by the interaction between metal and incident electromagnetic, a set of materials are used to form NPs and fulfill LSPR conditions. But different materials have their inherent electron concentrations, and corresponding to different oscillation frequencies, absorption and scattering wavelengths when the interactions emerge. Also with the help of powerful fabrication technique Nanosphere lithography (NSL), LSPR structures have been fabricated from Ag, Au, Al, Co, Fe, Ni, Zn, SiO<sub>x</sub> etc. During of them, transition metals, Fe, Ni and Co, combine with noble metals can enhance magneto-optical effects due to metal LSPR performance.<sup>30-34</sup> Nevertheless, for common NPs fabrication, materials Au and Ag are most used, because when the LSPR occurs, the spectrum drops in the visible range,<sup>35</sup> in addition, a number of detectors with these two material's nanoparticle are broadly applied to probe biomolecules with remarking sensitivity and low cost.<sup>36-39</sup> But, Ag is susceptible to oxide, so Au is preferred to be adapted to apply in our experiment.

### **1.4.2 Influence of Nanoparticle shape and size on LSPR**

It is noticed, that the relationship between nanoparticles shape, size and LSPR, but both of them have an outstanding effect on LSPR. Researchers have succeeded in synthesizing various shapes nanoparticles in lab to observe corresponding properties. Such as spheres, cubes, nanorodes, nanoshells etc. The change of shape and size

metallic nanoparticles results in surface polarizations, further to affects the plasmon resonance.

Figure 1.6 illustrates the previous comparison of simulated results of different Ag nanoparticles structures in water. Compared with Ag sphere (Figure 1.6a), others Ag nanoparticles structures exhibit multiple resonance peaks, meanwhile their main resonance peaks are obvious red-shift. The peaks red-shift contribute to charge separation which diminish the restoring force for electron oscillation, hence, the resonance peaks tend to lower energy.<sup>40</sup> At the same time, it is clear that their peaks intensities are distinct. The peak intensity strongly depends on symmetry of nanoparticles.<sup>41</sup>

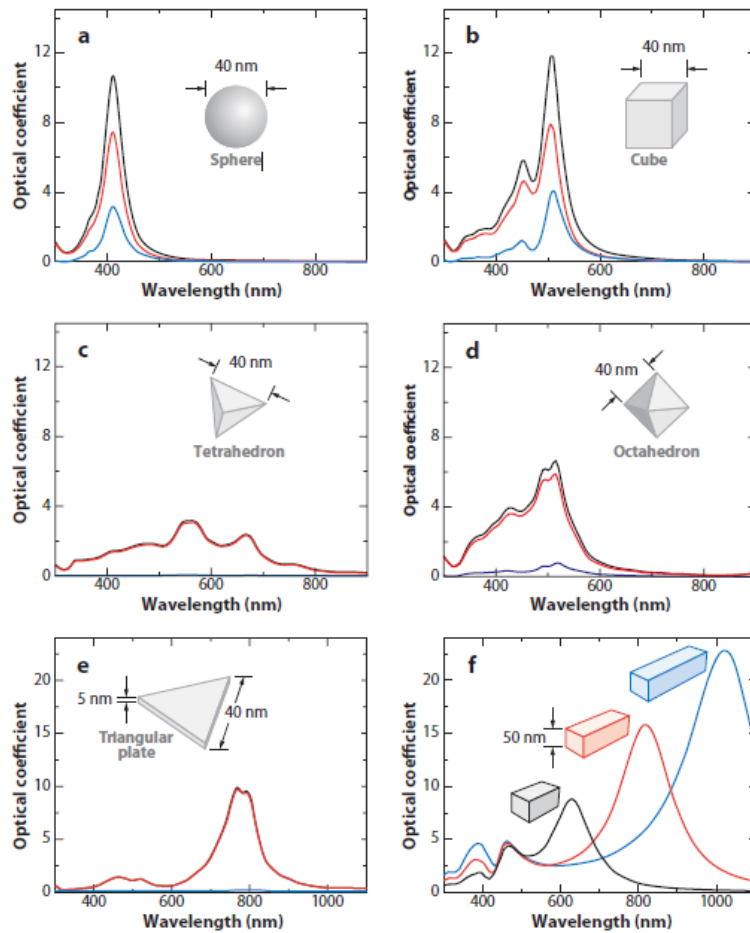


Figure 1. 6. Various shapes of Ag nanoparticles: (a) a sphere, (b) a cube, (c) a tetrahedron, (d) an octahedron, (e) a triangular plate, (f) rectangular bars with aspect ratios of 2 (black), 3 (red), and 4 (blue). Extinction (black), absorption (red), and scattering (blue).<sup>9</sup>

Nanoparticle size plays another important role at LSPR spectral shift as well. The spectral resonance contains absorption and scattering two processes, they are all

influenced by nanoparticle size. When nanoparticle size is small, absorption process has a bigger proportion. While with the increase of nanoparticle size, the proportion of scattering process is enhanced. It is worth mentioning that the ratio of scattering to absorption is not affected by nanoparticle aspect ratio.<sup>42</sup> However, some papers show nanoparticle shape has much stronger effect on spectral shift than nanoparticles size. For instance, The 47 nm red shift is induced by spherical nanoparticle size changing from 10 to 100nm, while change the elliptical nanoparticle aspect ratio from 2.5 to 3.5, that results in a shift of 92nm.<sup>35</sup> Meantime, the refractive index sensitivity of the surrounding medium depends on nanoparticle shape.<sup>43</sup>

In fact, it is not easy to distinguish nanoparticle shape and nanoparticle size effects on LSPR results. People tend to use aspect ratio to instead of them. Large number aspect ratio presents oblate nanoparticle. Precedent research supports that LSPR extinction maximum wavelength shift to red wavelength when nanoparticle aspect ratio increases.<sup>44,45</sup> At the same time, the higher aspect ratio nanoparticle has, the better sensitivity is.<sup>46</sup> Also, combination of changing aspect ratio and geometry can help to change LSPR wavelength.<sup>45</sup>

### **1.4.3 Influence of interparticle spacing on LSPR**

The gap distance between nanoparticles should be considered in LSPR results analyze, to some degree, it is responsible for LSPR spectral shift. When nanoparticles are very close, their oscillations of conduction electron affect each other, and then that have an effect on LSPR extinction maximum wavelength shift and results in an increase in surface-enhanced Raman scattering.<sup>47,48</sup> This phenomenon can be described like this: the near-field dipolar interaction takes a big account when nanoparticles spacing is much smaller than incident light wavelength, by contrast, the far-field dipolar interaction has a big proportion when spacing is approximate to incident light wavelength. Examples of effects of interparticle spacing also have been studied using Au nanoparticles<sup>49</sup> and theoretical simulated between tip to tip of two triangular nanoparticles.<sup>50</sup>

## 1.4.4 Influence of substrate on LSPR

In devices, nanoparticles can't exist individually. They must be fabricated over a substrate. A systematic study is presented in the following references<sup>51, 52</sup>. In Duval Malinsky's study<sup>51</sup>, Ag nanoparticles are fabricated via the Nano-Sphere Lithography (NSL) technic over various substrates. They show that the LSPR peak wavelength shifts to low energy wavelength when substrate refractive index increases, meanwhile LSPR maximum wavelength and refractive index of substrate have a linear relationship scaling with  $\frac{\Delta\lambda_{\max}}{\Delta n_{\text{substrate}}}$ . Other investigations show that plasmonic particle at a distance of a substrate present a LSPR extinction maximum wavelength red shift, as displayed in Figure 1.7.<sup>53</sup> Finally, when the distance is in a few nanometers, the resonance wavelength is split in to two peaks.<sup>53</sup>

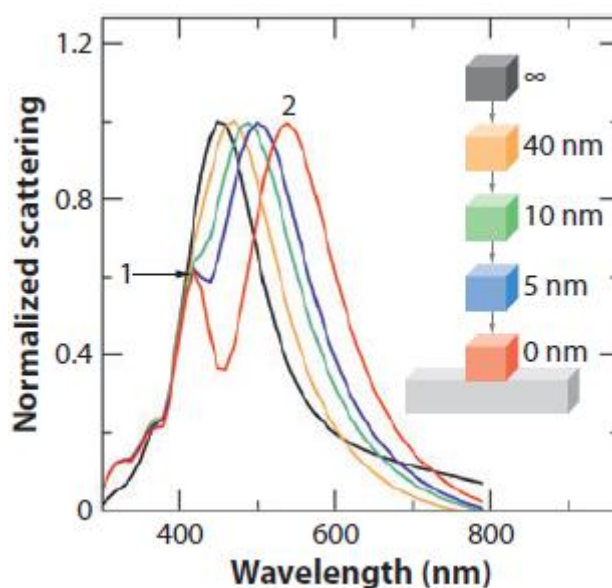


Figure 1.7. The emergence of a second peak as a single nanocube approaches a dielectric substrate.<sup>53</sup>

## 1.4.5 Influence of dielectric environment on LSPR

Besides the elements we mentioned above, the effect of nanoparticle surrounding environment on LSPR wavelength can't be neglected. Especially for spherical nanoparticles, the LSPR wavelength linearly scales with the index of refraction of the surrounding environment.<sup>41</sup> And also in order to prove this conclusion, theoretical simulations and experiment are done, the results are shown in Figure 1.8.<sup>51</sup> The results

show the relationship between LSPR extinction maximum wavelength ( $\lambda_{\max}$ ) and surrounding environment refractive index ( $n_{\text{external}}$ ). Even the experiment results don't have a good fitting with simulation results, but they both follow the same tendency.

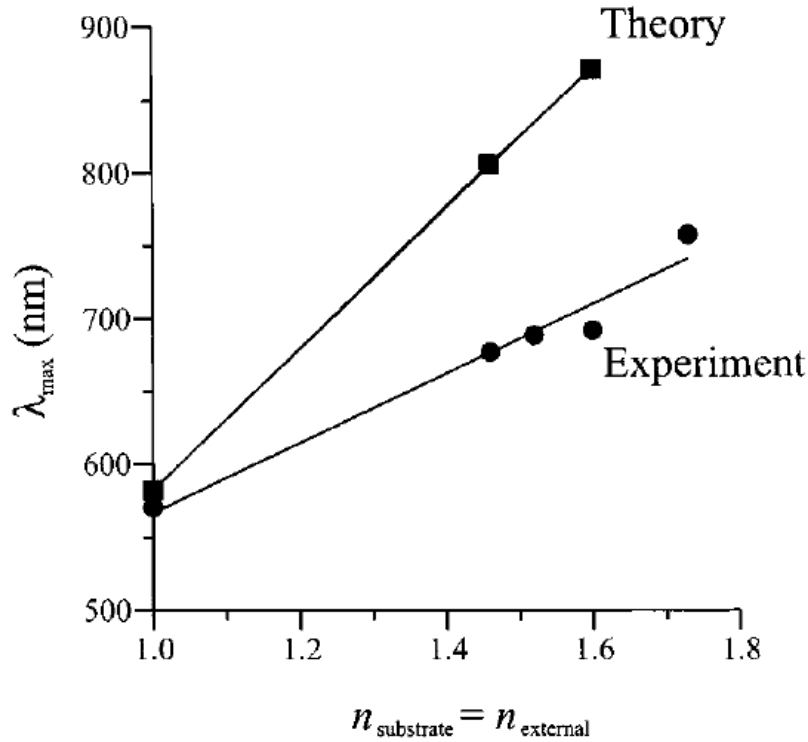


Figure 1.8. Maximum wavelength of the LSPR of Ag nanoparticles versus the refractive index of the medium.<sup>51</sup>

## 1.5 Applications of LSPR

The metallic nanoparticles are employed in a serial of applications in nanophotonics, such as <sup>54</sup> biosensors, <sup>55-57</sup> photovoltaic devices, <sup>58, 59</sup> biomolecular sensing, <sup>60</sup> chemical sensors, <sup>61, 62</sup> Surface-enhanced Raman spectroscopy<sup>63, 64</sup>. Among all of them, let us notice: Photovoltaic devices, biosensors and Surface-enhanced Raman spectroscopy, are widely used and close to our daily life.

### 1.5.1 Photovoltaic devices

No one doubts that after the solar cell, which is the device converting the sunlight into electricity, been produced by Bell Labs in the 19th century with 6% conversion efficiency that is not as high as present,<sup>65</sup> but it provides humans a good way to solve

the fossil fuel consumption to some degree. Due to its bright future, it never failed to draw human's attention. Therefore, with the advent of developed semiconductor technology and through many generations of researcher's effort, a big progress in this field has gained. Even so, the low-cost and high efficiency solar cells also are the goals of researchers pursuing for.

As is known to us, the active layer plays a vital role in solar cell structure. Indeed importantly, the light is absorbed and electron-hole pairs are created in this region. To make sure the light can be completely absorbed, in convention, the absorber layer must be thicker. Also increase active layer thickness can bring more light absorption and electron-hole pairs, but it also results in the device resistance and the cost increase. So localized surface plasmon resonance property of metal nanoparticles can enhance the electron-hole pairs creation without increasing active layer thickness. Meanwhile, thin film solar cells, with high efficiency and low cost, are competitive with conventional silicon-wafer-based solar cells.<sup>66</sup> But to thin film solar cells surfaces, they can't have the same surface light trapping forms, just like pyramid surface texture which can increase effective light path length. So for this case, the striking properties of metal nanoparticles offer a strategy to serve as light trapping form.<sup>67-69</sup> Meanwhile, metal nanoparticles can decrease light reflection and have the same traditional textured surface effects (Figure 1.9 a).<sup>58</sup> Also it is proved that the application of metal nanoparticles in photovoltaic cells did enhanced optical absorption and conversion efficiency.<sup>70-73</sup>

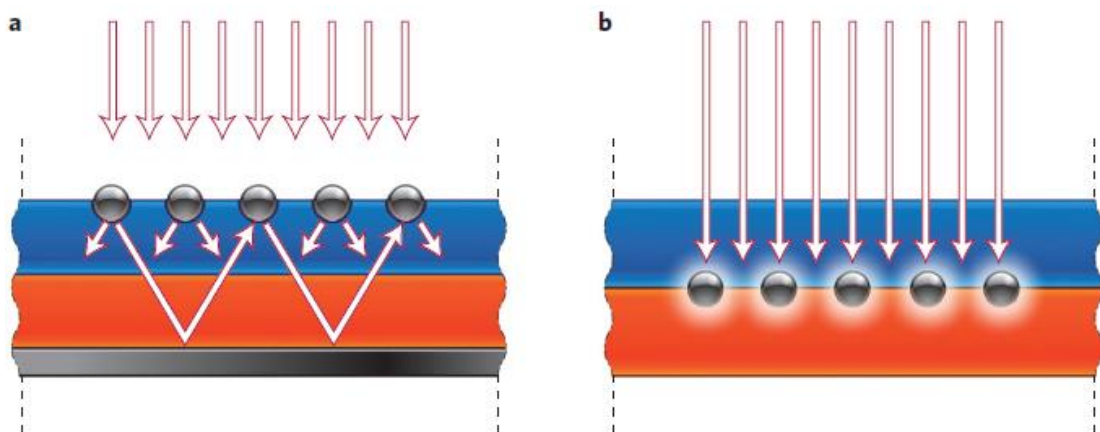


Figure 1.9. Metallic nanospheres serve as light trapping. a, metallic nanospheres scatter the incident light into solar

cell by multiple and high angle scattering, causing an enhancement of effective optical path length. b, metallic nanospheres are set in the semiconductor for light trapping.<sup>58</sup>

Here, we are explaining how metal nanoparticles work in solar cells structures. Metal nanoparticles enable light trapping in solar cells structures as two main types. In the first configuration, see Figure 1.9 a, metal nanoparticles are placed at the top surface, and the incident light will be scattered by them. But at the interface, the light scattering is not symmetric. It tends to scatter more into the dielectrics with the larger dielectric permittivity.<sup>74</sup> The deviated scattered light at some given angles will also increase the optical path length in the dielectric. Besides, if the angle of scattered light is larger than the total internal reflection critical angle, the light will still transmit in dielectric. Additionally, if the device has a reflecting metal back contact, the light is reflected to the surface, and be scattered again by the same mechanism. This repeated light transmission in dielectric increases the effective light path length. In a second configuration, see Figure 1.9 b, metal nanoparticles are embedded at the second interface. When the LSPR occurs, due to the enhanced near-field radiation effect, new electron-hole pairs will be created in active layer, so results in solar cells photocurrent generation enhancement. Of course, in order to trap the incident light as much as possible and gain the optimized priorities of device, nanoparticle's material, size, geometry and local dielectric environment can be selected.<sup>75</sup>

## 1.5.2 Biosensor

As is acknowledged that biosensor can function in numerous situations, just like food quality and safety, environment monitoring and other aspects.<sup>75</sup> Hence, the attention in its corresponding research keeps increasing, and various biosensor based on optical principles have been designed.<sup>76-78</sup> Biosensors based on surface plasmon resonance have a number of advantages, such as high sensitivity, real-time detection, large detective area and so on, biosensors based on localized surface plasmon resonance are cheaper and easily design and fabricated, as the fact that localized surface plasmon

resonance can be excited directly by light. Besides, it is demonstrated that some biosensors based on localized surface plasmon resonance can own the comparable sensitivity with of that based on surface plasmon resonance.<sup>79</sup>

As described in preceding text, localized surface plasmon resonance phenomenon is relative to nanoparticles shape, size, surrounding environment and serial elements. This phenomenon appears with selective photon absorption and scattering, so exhibits different colours. Based on this feature, biosensor can use colorimetric method to analyze test sample concentration. Also, for nanoparticle type, suspending nanoparticle in solution<sup>80</sup> or fixed single nanoparticle on substrate<sup>81</sup> can be fabricated.

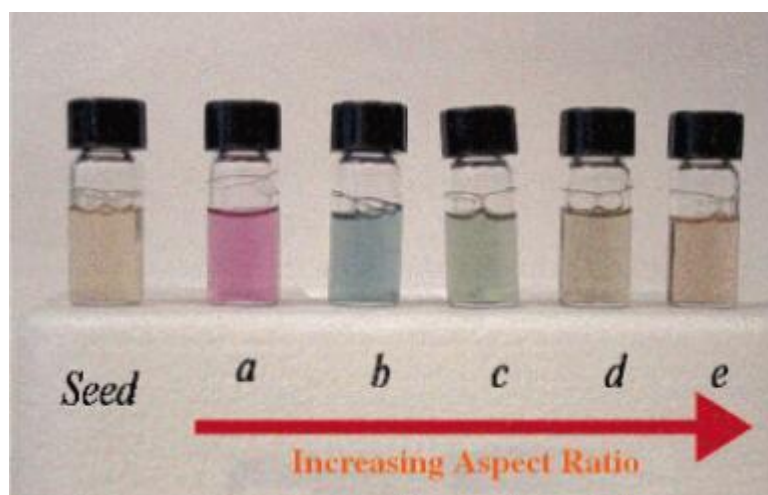


Figure 1.10. Photographs of gold nanorods with various aspect ratios in aqueous solutions.<sup>82</sup>

### 1.5.3 Surface-enhanced Raman spectroscopy

One of the branches of LSPR application is surface-enhanced Raman spectroscopy (SERS), benefiting from its advantages in chemical and biological molecules analysis in fundamental research and applications in pharmacology, food safety, etc.<sup>83-86</sup> Raman scattering is distinct from conventional Rayleigh scattering. Rayleigh scattering: When the incident light into the material, the photons are scattered with the same frequency as before. Nevertheless, a fraction of photons, after they are scattered, their frequencies are changed, some of them have higher frequencies or some of them has lower frequencies, that is resulted from the interaction of the molecular vibrations or rotations with the incident light. This is firstly observed by the scientists C.

V. Raman and K. S. Krishnan in liquids in 1928.<sup>87</sup> But compared with Rayleigh scattering, its signal is pretty weak, as normal it is nearly 10 million times weaker than Rayleigh scattering. In order to enhance and detect Raman signal, after SERS is first observed by Fleischmann in 1974 at a silver electrode and three years later researchers start to reveal the origin of the surface enhancement effect,<sup>88, 89</sup> enormous efforts and study have been done in this field over the past decades. At last, it is universal acknowledged that SERS is one of the most effective methods to enhance Raman signal and one of the widely used Raman-detection techniques in labs and industries.

Up to today, though through few decades research, to the Raman signal enhancement mechanism, there is no systematic theory. But based on the experiment experience, electromagnetic enhancement<sup>90</sup> and chemical enhancement<sup>91</sup> are accepted to explain the results. Electromagnetic enhancement takes the big part in enhancing Raman signals by the SERS techniques. This is because electromagnetic enhancement arises from the enhancement of local electromagnetic field during light-matter interaction. And the signal of SERS approximately scale with  $|E(\omega)|^4$ ,  $E(\omega)$  is the electromagnetic field of incident light, so the enhancement factor  $EF_{EM}$  can be written as

$$EF_{EM} = |E(\omega)|^4 \quad 1-11$$

From the equation, it is easy to get that a little increase in incident field can bring a significant amplification. Hence, the signal can be detected. Compared with electromagnetic enhancement, chemical enhancement possesses a small proportion of effect in SERS, but it is detected in experiment. The specific details can be found in according references.<sup>92</sup>

## 1.6 Origin and motivation of "W" structure

As referred in previous text, propagating surface plasmon can be generated at the flat

long interface, in this case, we propose to use instead of a flat interface, a "W" structure presented in the following Figure 1.11. The details of the Coupled Bi-Directional Sampling Spectrometer (CoBiSS) principle can be found in Y. Hadjar's article<sup>93</sup>. In this work, a refractive index gas sensing device is proposed based on the combination of the CoBiSS spectrometer and a surface plasmon resonance (SPR) chip. From this configuration, a potentially more sensitive and/or selective device could be proposed replacing the SPR (flat gold slab) chip by a LSPR chip such as the "W" periodic gold structure.

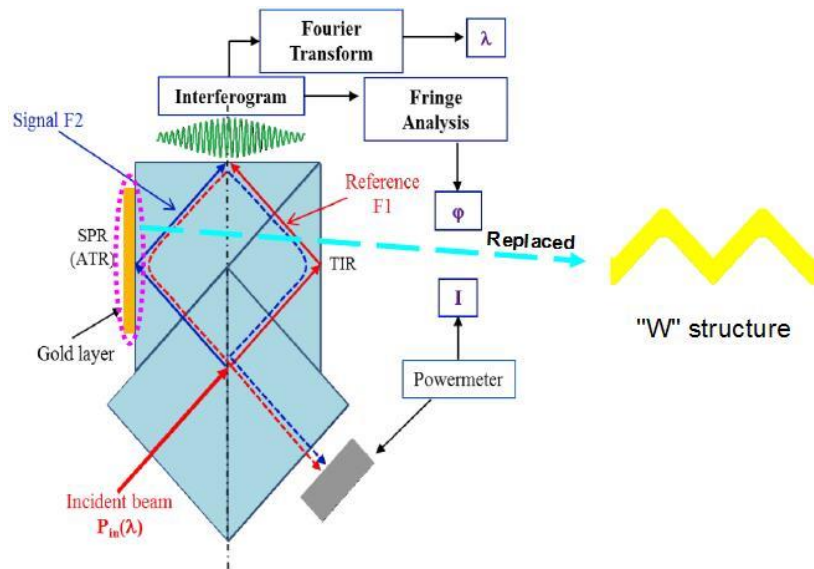


Figure 1. 11. Origin of "W" structure arises from Schematic of CoBiSS.

In the past decades, a lot of research focused on nanoparticles shapes has been proposed and studied. Such as triangular nanoprisms,<sup>94</sup> nanocube,<sup>53</sup> octahedron,<sup>95</sup> rectangular bar,<sup>9</sup> pyramid<sup>96</sup> and V-groove.<sup>97</sup> Among of them, especially for the last two geometries, have interesting optical properties. For instance, pyramids metallic structures can enhance fluorescence thanks to important near-field amplification<sup>98</sup> and diminish the Si surface reflection in solar cells.<sup>99</sup> However, V-groove owns a robust localized plasmon-polariton mode.<sup>100</sup> To some degree, V-groove have singularities similar than pyramids. The periodic repetition of the V-groove geometry leads to the

“W” geometry. As pyramid and V-groove structures have interesting optical properties, similar geometries should present interesting properties too. Based on this original idea, in order to confirm the structure efficiency, before to do the fabrication, measurement and application, a series of simulations were carried out by R. PRASAD<sup>101</sup>.

## 1.7 Primary "W" structure research simulation

Simulation details are described in R. PRASAD thesis<sup>101</sup>. At the beginning, for primary research, a set of parameters of "W" structure are set as follows: The folding angle  $\alpha$  is set to  $32^\circ$  and the incident light is set with a fixed angle  $45^\circ$ . At the outset, for the sake of testing, the large segment is not set as constant, so its values vary from 400nm to 1000nm by 200nm step. Of course, in fact, the peaks and trenches are not as sharp as ideal, but to simplify modelisation, the radius of curvatures is taken as follow  $r = 5$  nm. At the same time, because the gold structure is deposited on glass and polymer materials, both defined with similar refractive, an average refractive index value 1.52 is used for simulation. Different gold layer thicknesses are explored, 10, 20, 30, 40, 50, 60 nm. Meanwhile, the light wavelength is analyzed from 400-900 nm.

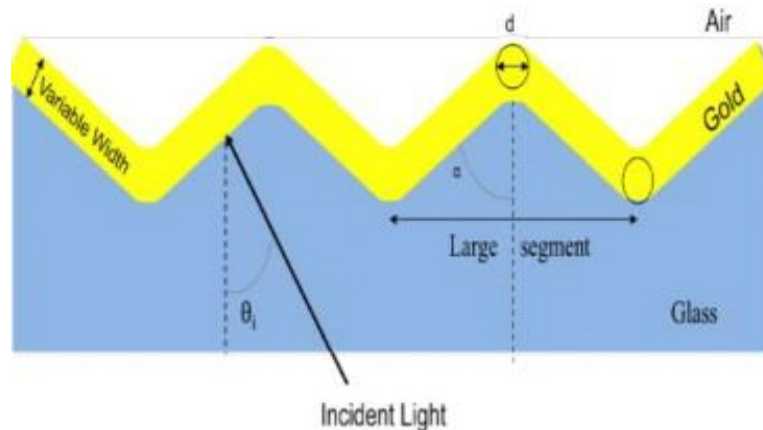


Figure 1. 12. CoBiSS modified for the Detection of SPR with modified "W" structure with  $2 \times \text{Radius} = \text{Diameter} = 10$  nm

Through some comparison results, the structure with 600 nm large segment (pitch),

gold with 25 nm thickness tends to possess better sensitivity than the other three.

The refractive index of the upper material varies from 1 to 1.05 by 0.01 spacing, in order to estimate the sensitivity. The simulated reflectance curves corresponding to different refractive index are marked with different colours are shown in Figure 1.13.

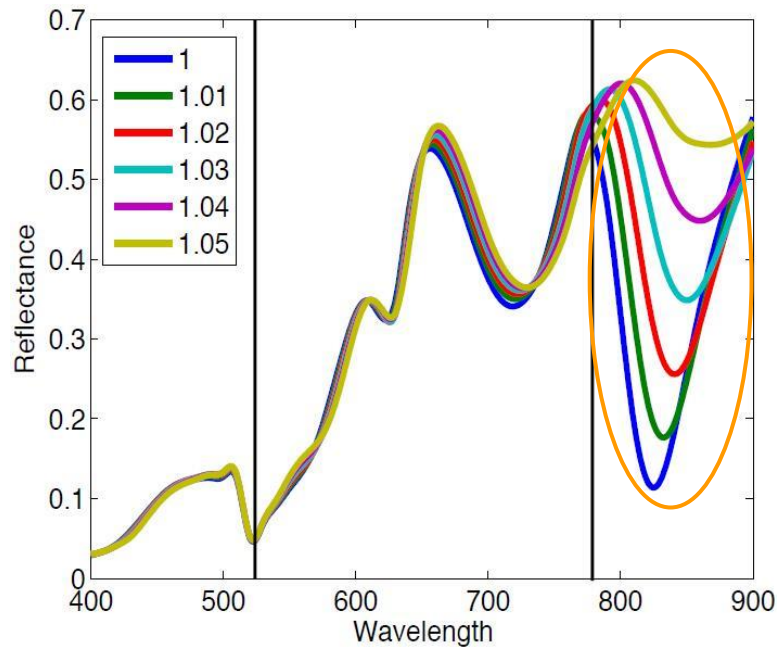


Figure 1. 13. Effect of reflectance with the variation of wavelength for multiple refractive index of layer above gold "W" structure that varies from 1 to 1.05 respectively.

From these curves we observe, that the curves are similar over a large range of wavelength, no obvious difference exists, but when the wavelength is over 760 nm (the second black line), the reflectance curves start to deviate, the deviation is marked by an orange circle. There is no doubt that this part with remarkable distinguish is very important for device sensitivity, and this performance applied in practical applications can make analyze easily to be done.

To summarize, this "W" structure possesses a good sensitivity in a given spectral window and can be an interesting candidate for LSPR applications. That is our original motivation to do the following work about it.

## 1.8 Summary

In this chapter, we have introduced some general basic elements of Local Surface

Plasmons (LSP), and the original plasmonic W- structure.

For the LSP, we introduce the basic principles, and describe the different and the same aspects between SPPs and LSP. We just pay attention to the latter type of surface plasmon in the following text. Two kinds of typical analyze model are cited, especially to Mie theory, it always owns an irreplaceable place in this field. Then a serial of elements impact on LSP are analyzed, based on the relationships, LSP applications are demonstrated as well.

For “W” structure, at first we present its origin. Then the corresponding primary simulations are presented from the Rohit PRASAD Thesis, showing good optical sensitivity properties.

## **1.9 Introduction of the chapters**

The thesis contains two main parts. In the first part, the first three chapters are dealing with metallic nanostructure W-shaped for Nano-optic, in the second part, the fourth chapter is specializing in Numerical simulation of tandem solar cells on silicon.

In the second chapter, the fabrication processes of W-structure are presented. We take an advantage of anisotropic wet etching of monocrystalline Si for template (mold) fabrication. Weak adhesion between silicon and gold facilitates W-shaped structure transfers from mold to a transparent substrate.

In the third chapter, experiment and simulation results of the W-structure are presented, as well as the properties of the near and far field also obtained by Differential method and Chandezon method.

In chapter 4, Silvaco simulation tool is used to study the III-V tandem solar cell based on GaAsPN as active layer and Si substrate. The work contains top cell (thickness, band offset in conduction band) and tunnel junction research. Finally, the total tandem solar cell simulation and top cell fitting between experiment and simulation are investigated as well.

## Chapter 2 Experiment

In order to obtain a "W" periodic gold structure, the fabrication contains mainly two parts: "W" structure mold fabrication and metallic "W" structure fabrication processes. In "W" structure mold fabrication processes, owing to Si is anisotropic, it is possible to get "W" structure mold. At the same time the alignment of crystal orientation between opening window and substrate is critical. In metallic "W" structure fabrication processes, it's not hard to do Au lift-off as the bad adhesion between substrate and metallic layer. Of course, each of them comprises many components. The first and most important step is to gain "W" mold, only if base on it, the further work can carry on. For "W" mold fabrication, silicon (Si) is used to as basic wafer, due to its anisotropic performance in etching liquid. That offers us the feasibility to reach "W" structure.

Next step is to metallic "W" structure fabrication. We take template stripping technique as method, on account of the bad adhesion of Au to Si. Also through the entire processes, some techniques are also applied to help to arrive to the aim. Photolithography for writing structure; Reactive-ion etching (RIE) for etching the layers on wafer; UV light for curing the polymer; Scanning electron microscopy (SEM) for checking structure's etching results, etc.

In this chapter, all the details of experiment principles and procedures are going to be referred. First and foremost, it begins with the important part that "W" structure mold fabrication: the basic theory, experiment details and corresponding problems and solutions. Then the following part is metal stripping: different materials and stripping methods for metal lift-off are introduced based on preceding mold.

## 2.1 W-structure mold fabrication

### 2.1.1 Principle of W-structure forming process

There is no doubt that W-structure mold plays the most critical and fundamental role in experiment. It goes through from the beginning to the end of the fabrication section. At first, principle of the fabrication is shown in Figure 2.1. The wafer (Figure 2.1 (a)) comprises two materials, one is Si serving as substrate; the other is silicon nitride ( $\text{Si}_3\text{N}_4$ ) serving as mask layer, in order to protect the unexposed Si from damage in the subsequent wet etching process. By following, Figure 2.1 (b), some portion of  $\text{Si}_3\text{N}_4$  is removed in the form of rectangles with spacing to each other, so the underneath Si becomes exposed to etchant. After that, we use wet etching method to form W-structure; As shown in Figure 2.1 (c), because of Si anisotropic property, the etching rate is not the same along different crystallographic orientations. The rate in (100) plane (red mark) is higher than that of (111) planes (blue mark).

Due to the presence of  $\text{Si}_3\text{N}_4$  mask layer, at the beginning of etching trapezoidal grooves appear; And as the etching time goes on, the trapezoidal grooves change into triangle V-grooves, but there is still a distance between edges of grooves, as illustrated in Figure 2.1 (d); As etching time increases, the shape of triangle grooves is not modified anymore, the only change of triangle grooves is their size. The longer is the etching process, the larger are the V-grooves and it results in the much smaller distance between them. When the etching time is appropriate, the adjacent summits of triangle grooves meet each other, and the W-structure is done (Figure 2.1 (e)).

The next step is the mask layer removal (Figure 2.1 (f)). At last, the W-shaped mold is gained. Of course, this is just in theoretical analyze, as for experiment, in the coming text, many problems occur and should be solved.

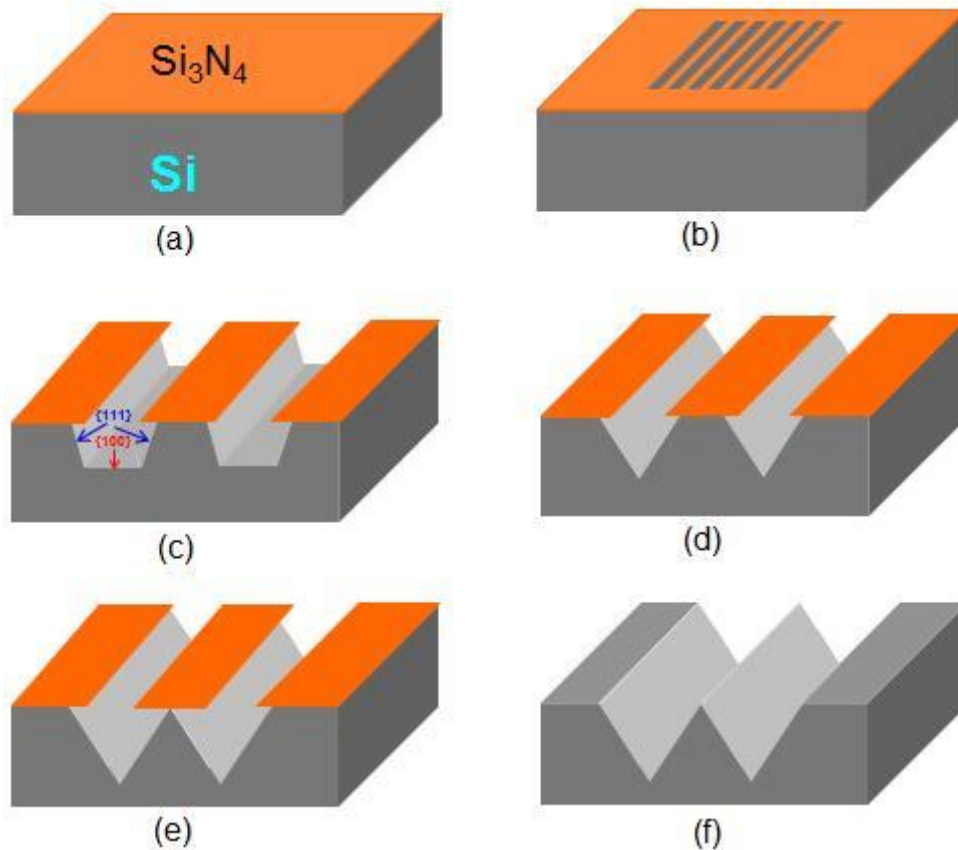


Figure 2.1. Principle of W-structure forming process based on Si substrate covered by  $\text{Si}_3\text{N}_4$  mask layer. (a) Si substrate covered with  $\text{Si}_3\text{N}_4$ ; (b) Openings in  $\text{Si}_3\text{N}_4$  mask to expose Si to etchant; (c) At etching start, trapezoidal grooves appear; (d) Triangle V-grooves formation; (e) W-structure formation; (f) Mask layer removal, bare W-structure mold is gained.

## 2.1.2 Fabrication of W-structure

It seems, according to theoretical knowledge of fabrication methods, that the W-structure it is easily feasible. Nevertheless, the fabrication cannot be done in a straight way: it is necessary to combine some microelectronic technologies. The following fabrication sequence was proposed: EBL using Poly-(methyl methacrylate) (PMMA) as a positive resist; dry etching (RIE) to remove mask in order to expose Si surface to the etchant, anisotropic wet etching.

Hereafter, the fabrication processes are described in details.

The Si substrate employed in experiment is covered by 100nm Silicon nitride ( $\text{Si}_3\text{N}_4$ ) layer. As mentioned in the previous part, it serves as mask layer in order to protect the part of unexposed Si wafer from etching during the wet etching process (Figure 2.2).

As a first step, PMMA is spin coated on the wafer surface (Figure 2.2 (a)). The PMMA is dissolved in methyl isobutyl ketone (MIBK) and its concentration is 30 g/L. We choose 3000 rpm/sec as acceleration, 3000 rpm in speed and 30 sec in time as Spin-coating parameters. With these parameters, finally the thickness of PMMA is around 180 nm. In order to get a flatted PMMA surface, the sample is kept in oven for 4 hours at 160° C. During the baking procedure, solvent evaporates out, just leaving PMMA on surface.

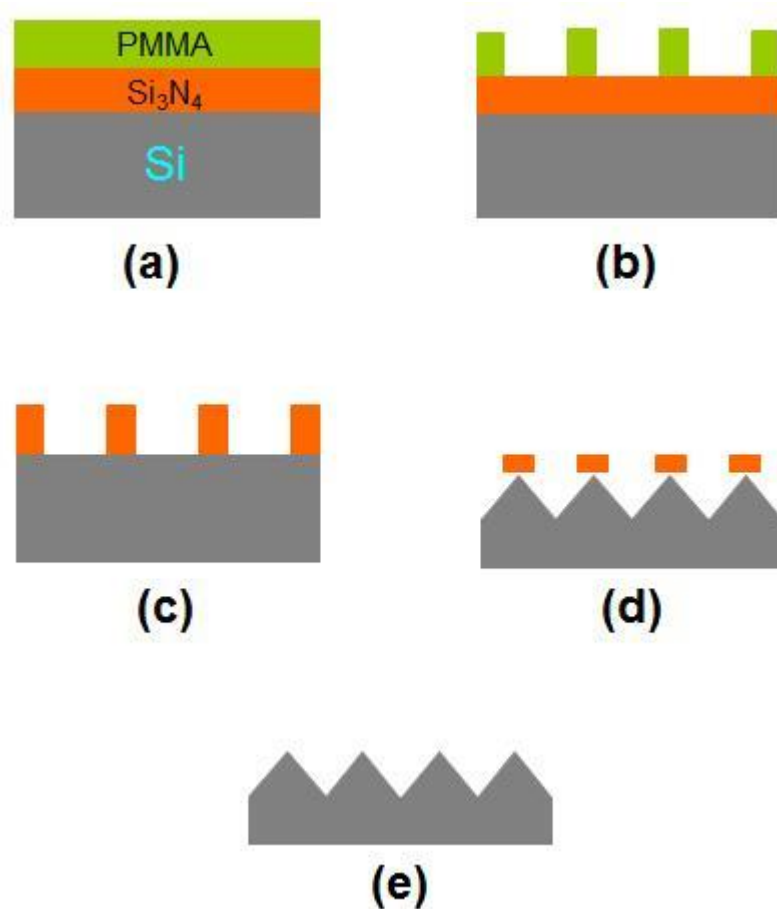


Figure 2.2. Fabrication process of W-structure based on Si substrate covered by Si<sub>3</sub>N<sub>4</sub> layer. (a) Photoresist coating; (b) Photolithography and development processes to write the designed patterns; (c) RIE etching process removes patterned Si<sub>3</sub>N<sub>4</sub> mask layer and PMMA; (d) Wet etching process to form W-structure; (e) Mask layer removal to gain bare W-structure.

After finish resist spin-coating, the subsequent process is to use EBL to write the designed pattern on PMMA with following resist development. For writing designed

pattern, HITACHI S-3500 SEM is employed and Nanometer Pattern Generation System (NPGS) is used to design the pattern and control the EBL process. As referred before, the Si is anisotropic. For gaining the ideal result, the pattern must be aligned strictly along the crystallographic axes orientations. But the identification of the crystal orientation is not so evident (more about this will be explained and refined in another coming part). For elementary trial, the designed arrays are slightly rotated (with  $0.2^\circ$  step) to match the crystallographic axes orientation, the theoretical patterns are presented in Figure 2.3. Taking the writing time into account, the angle range should be reasonably restricted. At the beginning of test, we adopt the range from  $-0.8^\circ$  to  $0.8^\circ$ . Correct rotation angle is chosen through analysis of the shape of the etched pattern. At the same time, the circles with different diameters are regarded as reference of crystal orientation. That is because during wet etching process, the orientations of (111) and (100) can form square shape, and the sides of square are parallel to the corresponding crystal orientations.

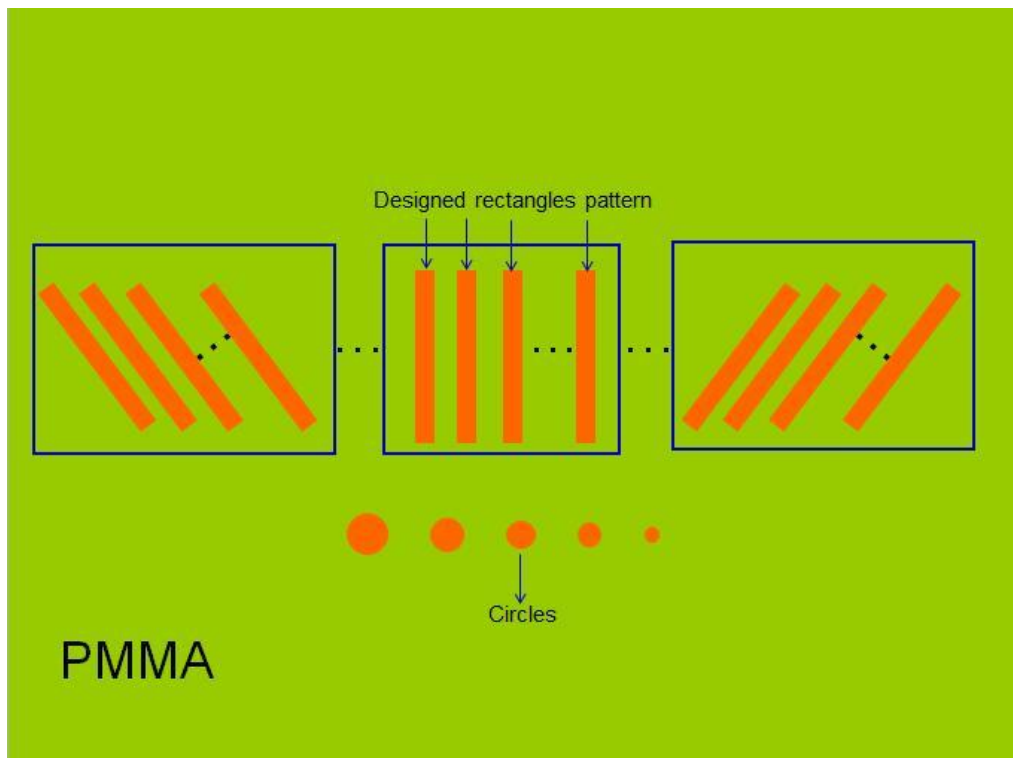


Figure 2.3. Patterns designed by Nanometer Pattern Generation System (NPGS). Every team, marked by blue frame, has the same number of rectangles. In the same team, rectangles are parallel to each other and have constant

spacing. Different diameters circle opening are used as measurement reference.

As PMMA is positive photoresist, so during the EBL writing patterns process, its molecular chains undergo the scission by the energetic electrons of the electron beam. After then, we put the sample into the developer mixture of Methyl Isobutyl Ketone (MIBK) and Isopropanol (IPA) with volume proportion 1:3) for 1 min to remove the broken PMMA chains. To clean up the remaining developer, it is recommended to immerse the sample in IPA for 15 s, and dry it with air blow. To now, the openings in resist are formed as Figure 2.2 (b) presents.

The dry etching process is done using capacitively coupled radio-frequency plasma system RIE PLASSYS MU400. Gases  $\text{CHF}_3$  and  $\text{O}_2$  are chosen to etch  $\text{Si}_3\text{N}_4$  and PMMA respectively. Now, the windows in  $\text{Si}_3\text{N}_4$  are open, nevertheless Si is covered by thin  $\text{SiO}_2$  layer formed during PMMA ashing in oxygen plasma. Therefore, we need to repeat  $\text{CHF}_3$  etching process (Figure 2.2 (c)). If the sample is put into solvent directly after RIE etching, the etching result is very bad (Figure 2.4). There are probably two phenomenon causing such an effect: a) teflon-like passivating layer is formed during RIE etching process, but the compound of elements and proportions are indeterminate; b) thin  $\text{SiO}_2$  layer is formed at air during transfer from RIE vacuum chamber to etching bath. Here after, two of them are named "Passivating Layer" (P-layer) shown in blue in Figure 2.4. For avoiding the P-layer influence, buffered hydrofluoric acid (BHF) is introduced prior to wet etching to treat the sample for 10 min, afterwards cleaned with deionized water, dried and immersed in etching bath as soon as possible. Tetramethyl Ammonium Hydroxide (TMAH) solution with 25% weight concentration is used as anisotropic etchant for our experiment. The resulting structure obtained with appropriate time and temperature is represented in Figure 2.2 (d).

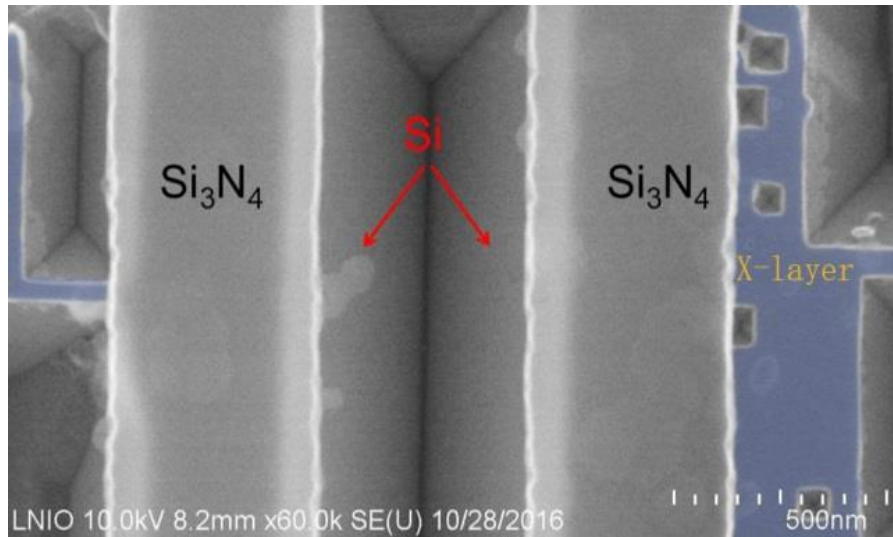


Figure 2.4. SEM image of sample result after TMAH etching. The sample is directly putted into TMAH for etching after RIE etching process.

The bared W-structure can be gained after mask layer is moved off by BHF by following. As shown in Figure 2.2 (e) (experimental result will be shown in following text).

## 2.2 Influence of BHF etching time

As it is seen from the description of last experiment processes, BHF is used twice. The first time is for removing the P-layer before wet etching; the second time, it serves for  $\text{Si}_3\text{N}_4$  removal. BHF reaction with Si surface is not strong, even so, if the sample immerses into it for a long time, just for test, for example, we keep our wafer sample into BHF for 20 hours, as shown in Figure 2.5 (a), the Si surface possesses a very awful quality. Even if the etching time diminishes to only 5 hours, it is still enough to rough exposed silicon surface, as shown in Figure 2.5 (b).

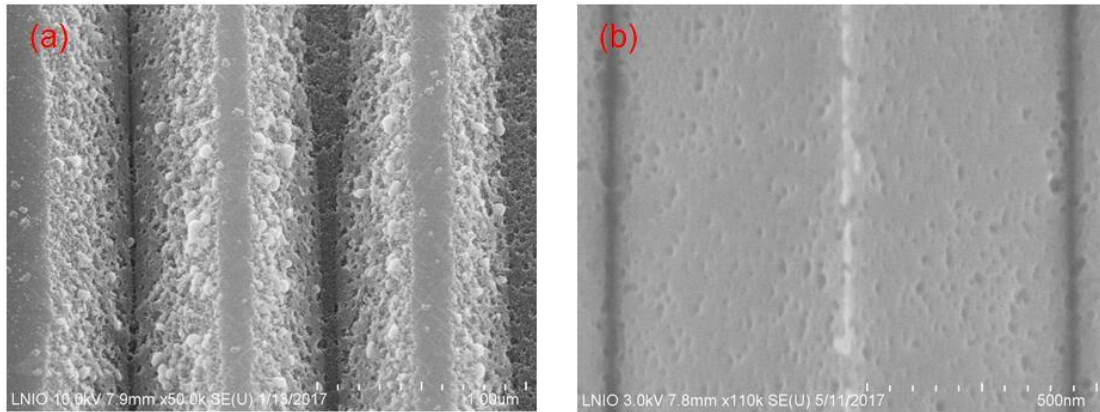


Figure 2.5. SEM images of Si surface with different BHF etching time. (a) Sample is etched for 20 hours with BHF. Si surface performance is awful. (b) The etching time decreases to 5 hours, the Si surface performance is better than (a), but there are also spots on Si surface.

To avoid this bad Si surface quality induced by BHF, and to gain as smooth as possible Si surface, we reduce initial thickness of the  $\text{Si}_3\text{N}_4$  layer down to 30nm with 3.5 hours in BHF solution. Thus, time of final  $\text{Si}_3\text{N}_4$  removal is reduced down to 1.5 hours. And so, the time of dry etching is proportionally reduced. From the final experiment result, it shows excellent Si surface nature, as smooth as shown in Figure 2.6. That is why we adopt that value.



Figure 2.6. SEM images of Si surface after mask layer removing. The mask layer thickness is around 30nm, and the etching time is 1.5 hours to remove it after W-structure formation.

## 2.3 Influence factors of etching results

Obviously, as described in Figure 2.2, the most important part in all of them is the wet etching section. Let us mention main technological parameters.

**Etching solvent concentration:** Although the etching rate decreases with increasing TMAH concentration, the quality of etched surface also strongly depends on concentration. The lower concentration leads to higher Si roughness due to micro-masking by hydrogen bubbles formation, and the best results we can obtain with TMAH concentration of 25%.<sup>102</sup> So, in all our experiments, the TMAH weight concentration in water is 25%, such that we can assure the best etching conditions.

**Etching temperature:** At high temperature condition, the molecule's speed of solvent is higher, thus resulting in acceleration of reaction with Si surface, following the Arrhenius rule. In order to assure constant temperature during etching, the sample is placed in water-bath heater (Figure 2.7) controlled with the precision of 0.1°C.



Figure 2.7. Water bath is to support a constant temperature environment.

**Open window size:** If the open window is too small, that means the consumed TMAH can't be efficiently refreshed, as a consequence, etching rates are not stable. By contrast, if the open window is very large undercut Si walls contact less TMAH, and etching depth is shortened. So, the appropriate open window size is also an important factor.

**Pattern writing process:** Open window size determines the size of exposed Si, during writing patterns process. After the patterns are designed, it is supposed that after the writing patterns process, every sample has the same size rectangles. In practical,

when sample is changes, it is imperative to refocus the electron beam. So the spots have different diameters, finally, the rectangles have different size. The exposed Si areas and etching results are not the same.

**Etching time:** This is obvious that long etching time brings the deep etching degree. In our case this time will mostly depend on mask undercut etching rate, which, in turn, depends on (111) face etching rate. In order to get the approximate etching time, for the beginning trials, we try long and short etching time (40 minutes and 10 minutes). Finally, based on the undercut etching rate estimation and on a number of satisfying results, we have found the best conditions.

**Alignment to crystallographic axes:** As it is mentioned previously, due to Si anisotropic properties, the open window sides must have good alignment with defined crystal orientation. But in experimental operation, the following elements have effect on the alignment.

**Substrate edges:** Thanks to its monocrystallinity, Si wafer can be relatively easy cleaved in small size samples. We use diamond pen to initiate the cleavage, and if the fissure runs along the crystal orientation, sample with good regular edges can be got. Indeed, it is difficult to get the ideal cleavage. Most of the time, the sample's edges look like in Figure 2.8. The edges are not straight, to some degree, that means the sample rotates some degree, and the rotation angle depends on flatness of the side that goes into contacts with the sample holder in the EBL process.

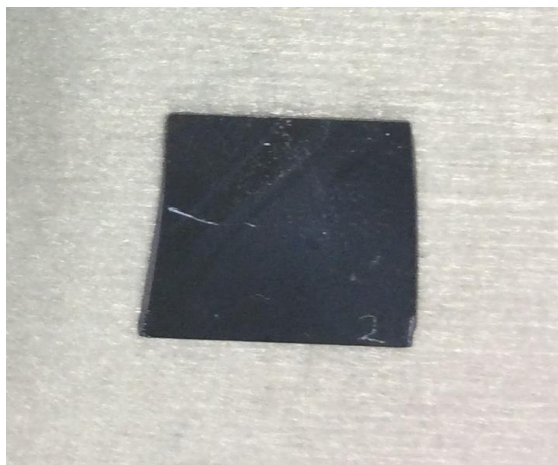


Figure 2.8. Sample substrate cut from wafer.

Sample holder alignment: As illustrated in Figure 2.9, before the writing patterns process, sample is fixed on sample holder. The flatness of contact edges of the sample holder also influences the final alignment result. The rotation of sample holder relative to stage translation axes and to electron beam scanning axes has to be taken into account.

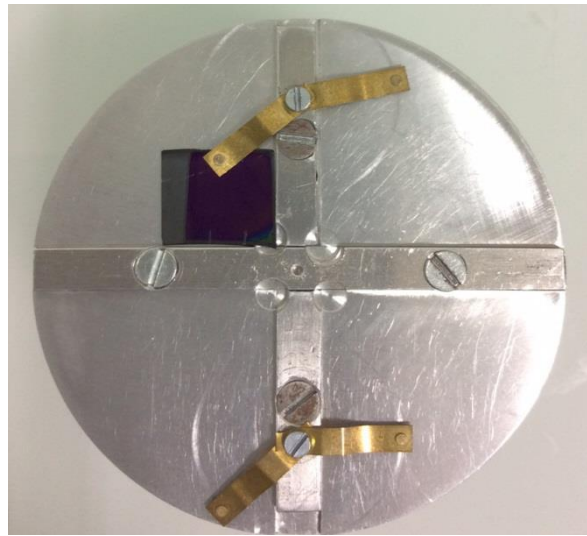


Figure 2.9. Sample is fixed on sample holder.

Although the manual alignment of the sample holder to the translation stage can be done visually (Figure 2.10), the precision of this correction is not enough for the consequent W-structure fabrication.

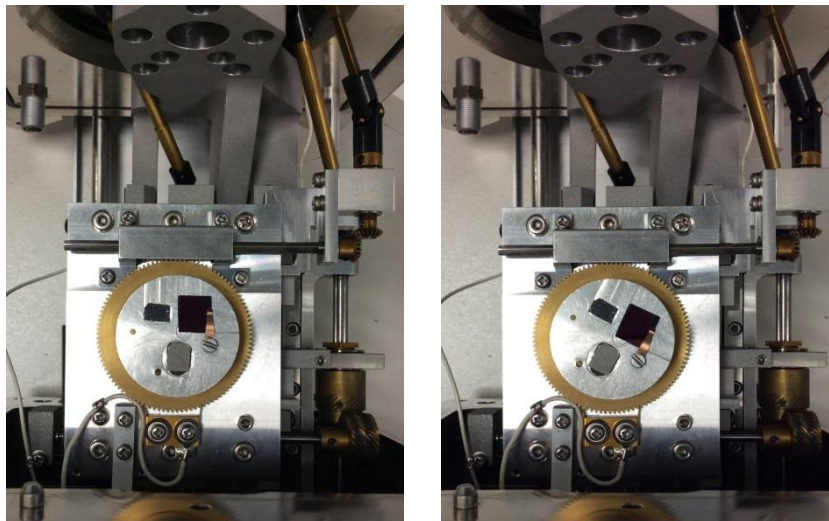


Figure 2.10. Sample holder fixed with sample on translation stage for EBL. It should be placed as straight as possible (left image), visible rotation has to be corrected

## 2.4 Sample alignment methods

As pointed out earlier, many elements have correlation with crystallographic axes orientation alignment. Even the patterns are designed with various angles, and some of them can be close to the ideal structure. But from the observation of experimental result, it shows that the deviation is inevitable. For solving this problem, “Circle Reference” method (hereafter, call it as CRM) and “Edge Reference” method (ERM) are introduced.

### 2.4.1 CRM

The original motivation owns to Si anisotropic property as well. As described in previous text, in anisotropic wet etching process the (111) plane has the slowest etching rate. Taking this advantage, for the first step, we create the opening in the mask having circular symmetry (in our case it is the circle), and do the preliminary wet etching. Thus we can get the structure in shape of truncated pyramid, having two base squares with every side corresponding to the intersection line of (111) and (100) planes, as shown in Figure 2.11, left image. If the etching time is getting longer, the four (111) planes meet each other, completing the reverse pyramid, as demonstrated in Figure 2.11, right image. Consequently, the square sides can play the role of crystallographic axes orientation references.

Once the sample is installed in EBL system, the angle correction alignment has to be performed in order to overlay the EBL write field axes and one of orthogonal sides of CR figure and as soon as this step is accomplished, the pattern exposure can be started.

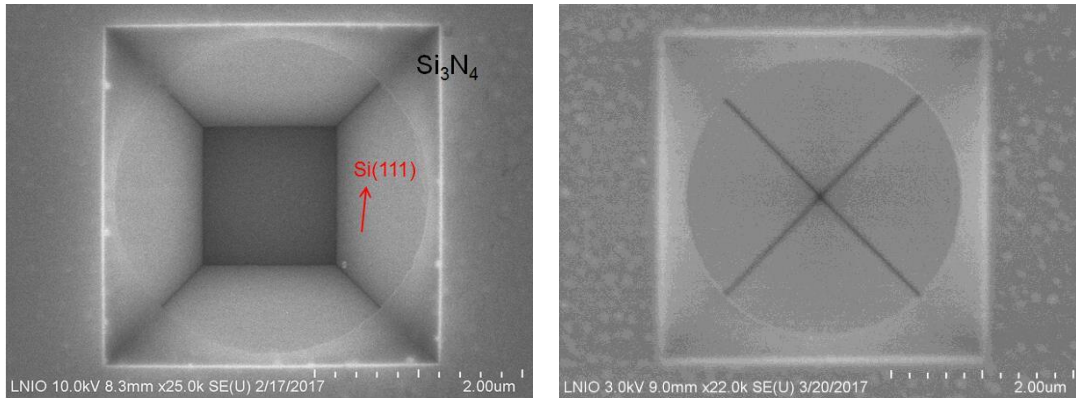


Figure 2.11. SEM images of substrate etching results. Left, square shape is formed at the bottom. Right, reverse pyramid is formed.

The functionality of CRM is proved experimentally. In this work, as presented in Figure 2.12, two sets of patterns are exposed on the same substrate. The difference between of them is following: alignment for the first set is done by CRM and the writing of the second one is proceeded without additional alignment step. After EBL patterns writing process, the subsequent development, RIE, BHF, wet etching, BHF removing mask layer processes are carried on, followed by SEM observation.

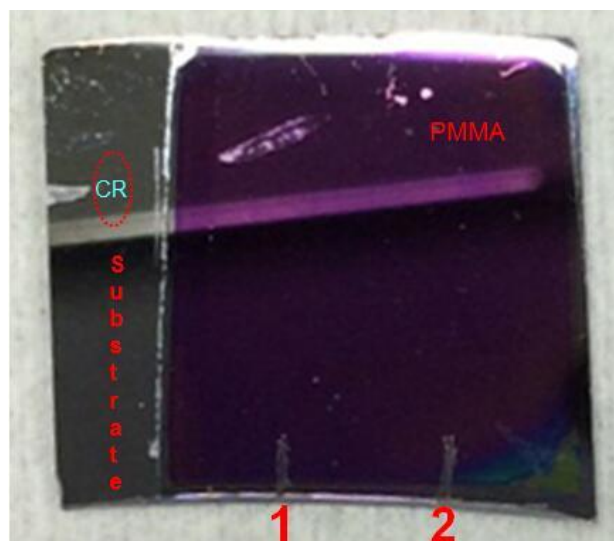


Figure 2.12. Compared experiment sample. CR is got in advance. Compared scratches 1, 2 are done with and without CR method respectively.

Images in Figure 2.13 show etching results without and with CRM respectively. As it can be easily seen in Figure 2.13a, the alignment between opened rectangles and (100) plane is bad. On the contrary, the structure done with CRM shows a perfect result as expected.

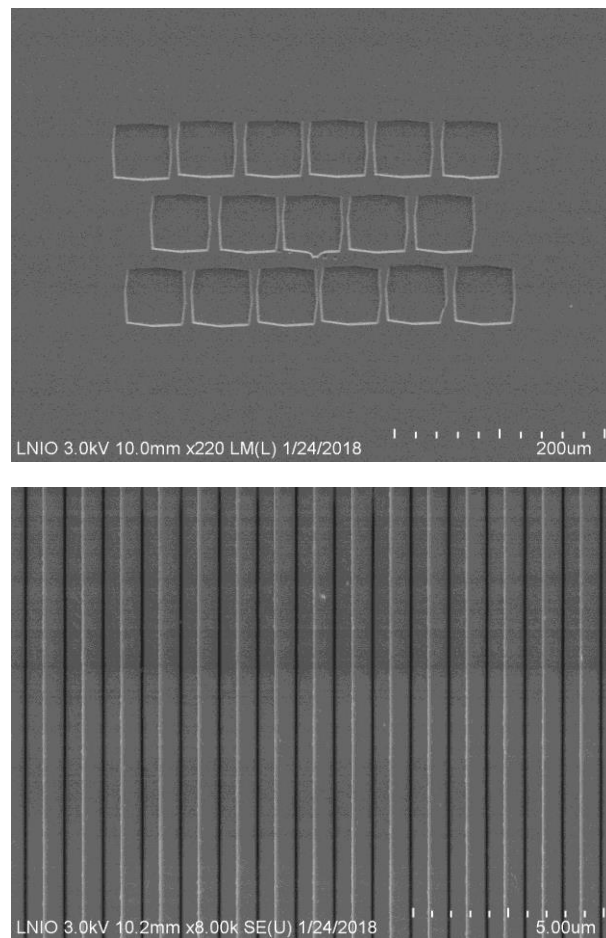


Figure 2.13. SEM images of CR compared experiment etching results. a: scratch 2 without CR method. The W-structure is completely etched away. b: scratch 1 with CR method, the good result is obtained..

CRM seems to be the universal way to make alignment even if it is more time and money consuming, since it doubles the processes of PMMA spin-coating, EBL, development, RIE and wet etching. But this method can be employed for this kind of samples whose edges are not straight. Take for example, the left image in Figure 2.14. We choose a sample with curve edge and put this edge on the sample holder at random on purpose. After the fabrication, the SEM image of experiment shows, the right image

in Figure 2.14, the W-structure with sharp, regular tips and smooth slopes is gained thanks to CRM.

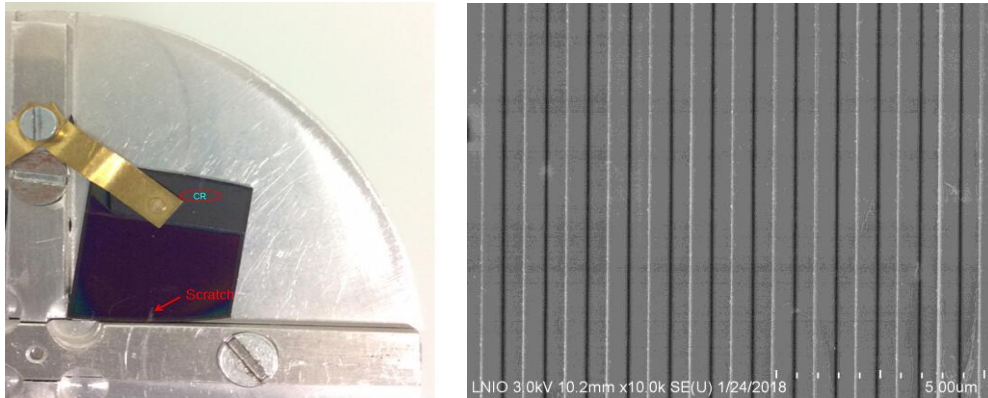


Figure 2.14. The images of curved edges sample fixed on sample holder and corresponding etching result using CRM alignment.

## 2.4.2 ERM

ERM is another way to reach crystallographic axes orientation alignment. This method is based on Si anisotropic properties as well. As the Si substrate is cut, it always cracks along the crystal orientation. For ideal case, the edges of well cleaved substrate are parallel to the corresponding crystallographic orientation.

Finally, after all the fabrication step (Figure 2.15) are accomplished, the SEM image shows the tips of “W” are as sharp as that obtained by CRM. Besides, compared with CRM, ERM possesses more advantages: time saving, low cost and the less processes.

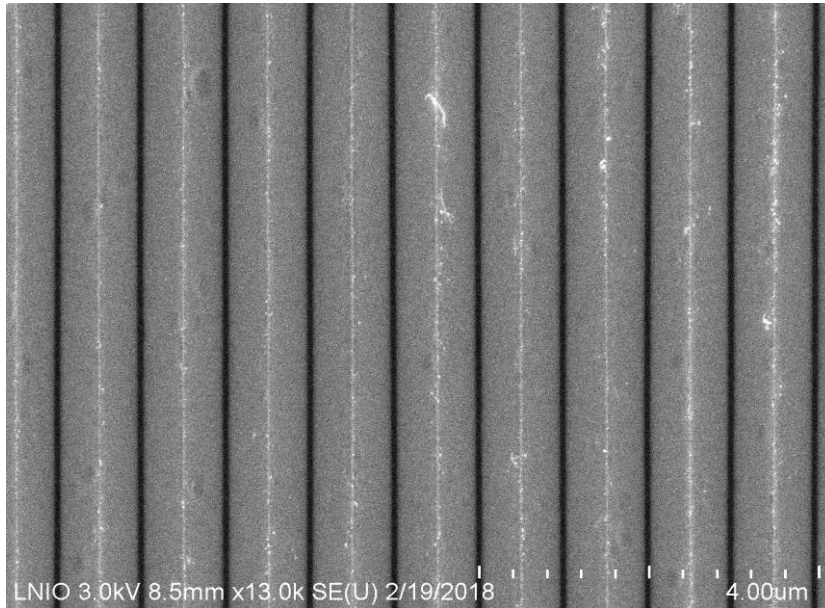


Figure 2.15. SEM image of etching result done with ERM.

## 2.5 Final W-structure mold

Figure 2.16 shows the scanning electron micrograph (SEM) images of Si W-structure corresponding to the stage of after TMAH etching and  $\text{Si}_3\text{N}_4$  removal processes. From the overview image Figure 2.16 (a), it is easy to understand that formed W- structure has a sharp tip. Figure 2.16 (b), represents zoomed image of tip. Through the analysis of these two pictures, it is obvious that the Si W-structure has well defined geometry, smooth sides and sharp tips. Meanwhile, in order to make sure the bottom of the groove is as sharp as a tip, we cut the sample and take the cross-section view as shown in Figure 2.16 (c), the inset picture shows more details. From the cross-section image we can see that the bottom of V-groove is also sharp. So, we can conclude that we succeed in fabrication of the W-structure.

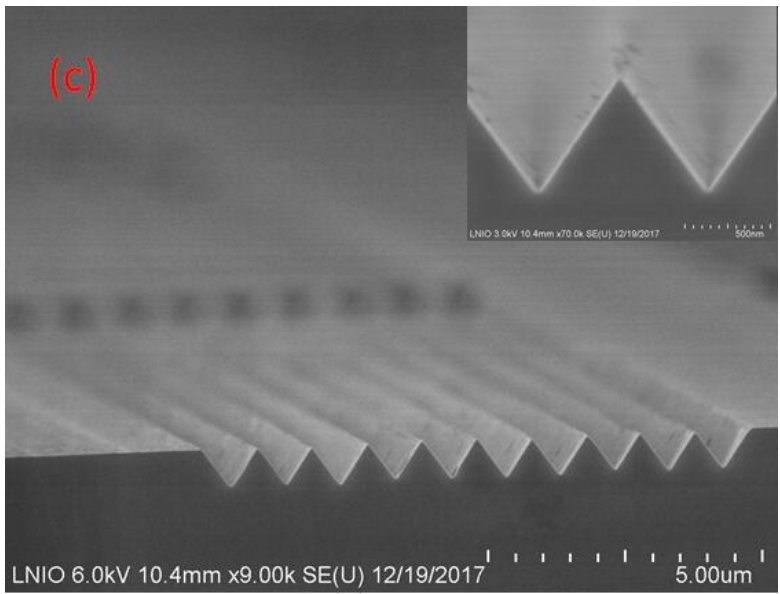
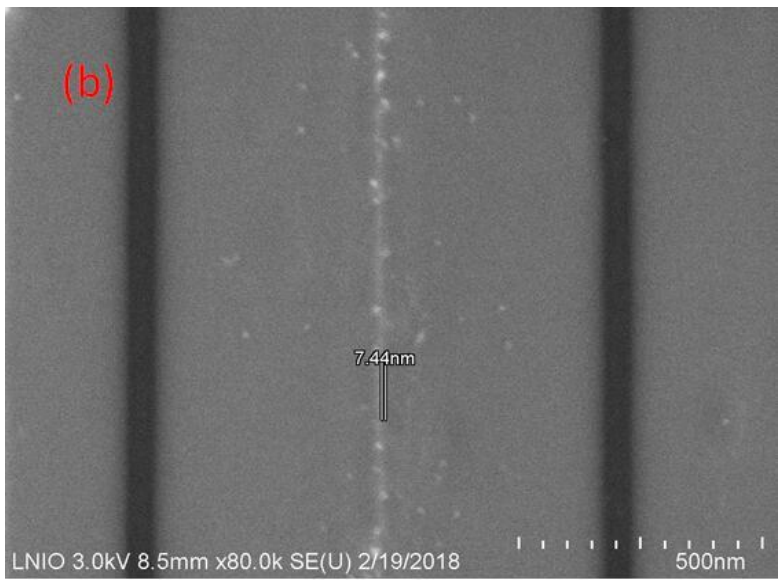
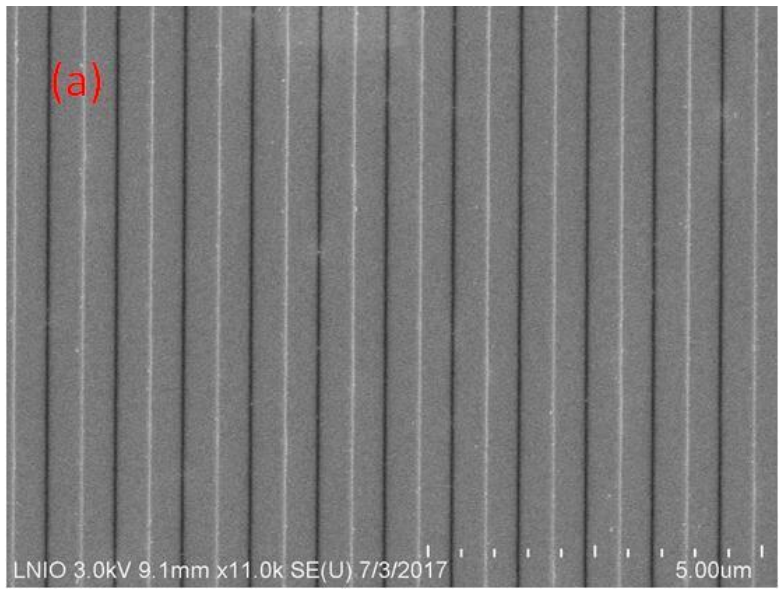


Figure 2.16. SEM images of Si W-structure. (a) Overview image; (b) Zooming image of tip; (c) Cross-section image.

## 2.6 Metallic W-structure fabrication

This fabrication step requires successful accomplishing of all previously described workflow. Once the W-structure mold fabrication is finished, metal is deposited on its top. Template-stripping technique based on poor adhesion between deposited gold film and a mold is used to peel-off metal layer from Si surface. Schematic diagram of the experiment is presented in Figure 2.17. The details of each step will be explained in following text.

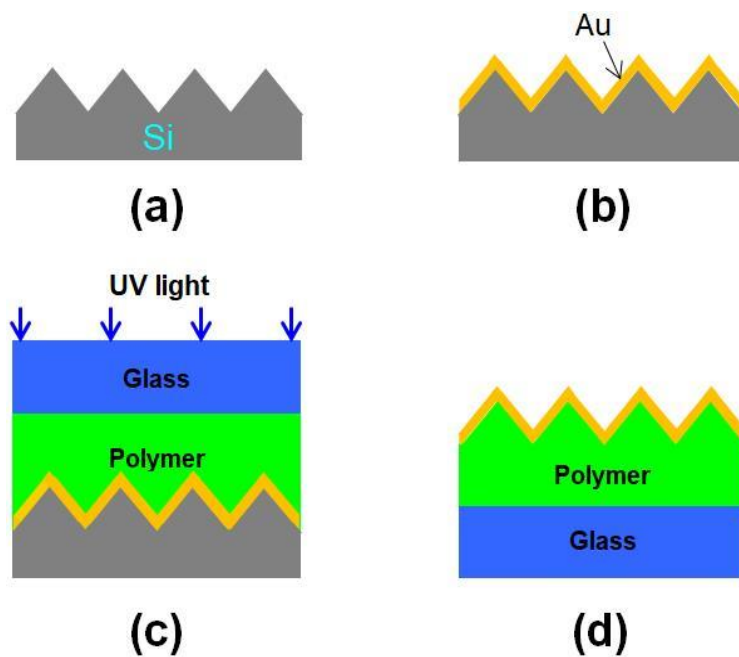


Figure 2.17. Metallic W-structure stripping schematic diagram. (a). Bared Si W-structure; (b). Au deposition; (c) Polymer deposition, glass superposition and UV light exposure; (d) After metal stripping process, the reversed metallic W-structure is got.

First of all, W-structured mold (Figure 2.7 (a)) must be well cleaned in order to remove any residual traces of chemical reaction products and other eventual contaminations. The sample is cleaned by Neutracon solution in deionized water in ultrasonic bath during 15 minutes. It is recommended to put the sample on hot plate at

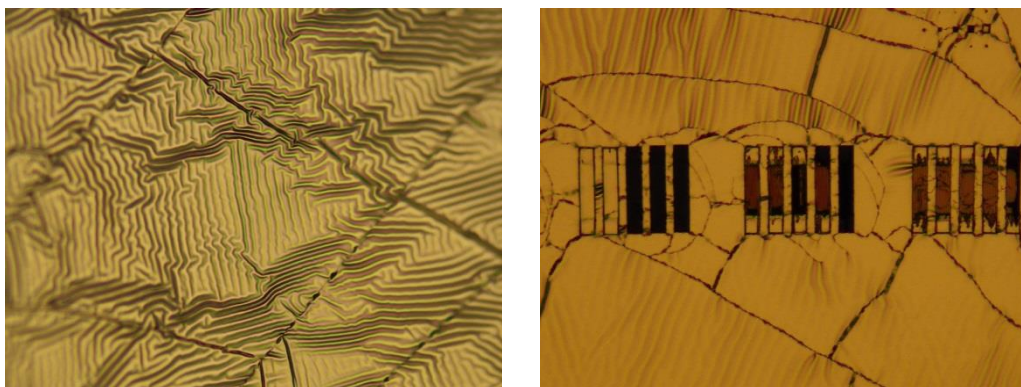
300°C for 5 minutes after gas dry operation, in order to make sure that no water is left on the surface of sample.

When the W-mold cleaning is over, the following process, as is shown in Figure 2.17 (b), is metal deposition. This process is conducted through physical vapor deposition technique using PLASSYS MEB400 evaporator. At first, gold (Au) layer is deposited using following parameters: thickness 50nm, rate 0.25nm/s, pressure  $1 \times 10^{-6}$  Torr. Secondly, in order to enhance the adhesion of metal to polymer, a thin titanium (Ti) layer is evaporated on top (parameters: thickness 3nm, rate 0.25nm/s, pressure  $1 \times 10^{-6}$  Torr.). Titanium film could be replaced by (3-Mercaptopropyl) Trimethoxysilane (MPTMS). In this case sample into the toluene solvent containing 1% MPTMS volume at least for 2 hours.

To transfer the Au layer, the polymer polydimethylsiloxane (PDMS) have been used.<sup>103-107</sup> . It was chosen due to its flexibility, transparency and low cost.

Prior to PDMS pouring Ti layer needs to be treated by oxygen plasma for few minutes. The liquid PDMS is poured on sample and they are curing for 2 hours at 75°C in oven.

From the tripping results, presented in Figure 2.18, it is evident that after the stripping process, the Au layer surface is heaped with irregular ripples and cracks caused by PDMS thermal curing. All in all, even if PDMS stripping possesses a plenty of advantages, the shrinkage is fatal to our structure. So another material for Au layer transfer should be employed.



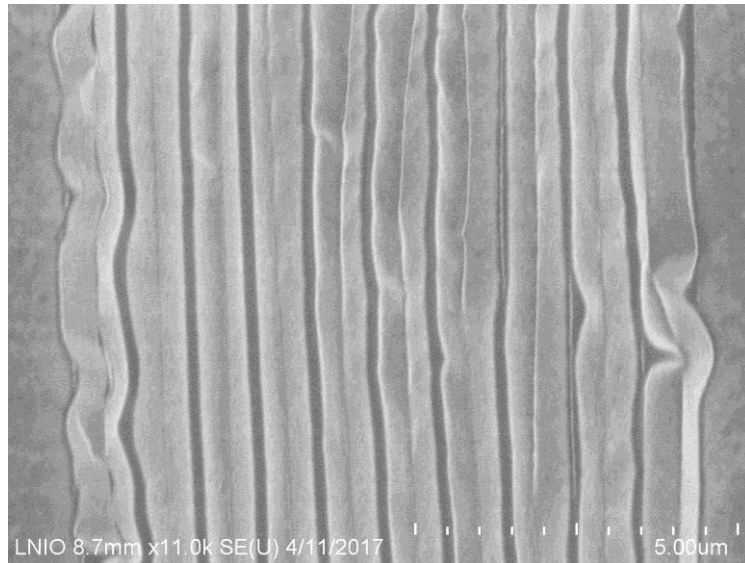


Figure 2.18. PDMS stripping results.

The polymer OrmoClearFX was chosen, as it has low shrinkage after UV curing. The value is always below 5%. Following process guidelines for OrmoClearFX, the surface of the metal layer is also treated by oxygen plasma for few minutes, and spin-coated by adhesion promoter OrmoPrime 08 (4000 rpm, time is 60 seconds, and acceleration is 1000 rpm/s). After spin-coating, in order to cure the OrmoPrime 08 and remove the residual solvent, we use hotplate to bake the sample for 5 minutes at 150°C.

OrmoClearFX is drop-casted on the structure surface. This polymer is solvent-free and thus has a high viscosity; we need to assure full coverage of W-shaped structure (penetration into the grooves). The drop is deposited on the sample and then left in yellow room for few hours.

The glass slide is used as stripping support. Prior to use, the glass is cleaned for 15 minutes in Decon90 deionized water solution in ultrasonic bath, rinsed in deionized water for 15 minutes and dried by air blow. At last, the glass is treated with oxygen plasma for few minutes and superposed with the metal-coated W-structure.

For curing, the sample is exposed under UV light, as shown in Figure 2.17 (c). Exposure dose is 1000 mJ/cm<sup>2</sup>, exposure time is 135 s. After UV light curing, it is baked for 10 minutes at 130°C on a hot plate. When the sample's temperature downs to room temperature by nature, process proceeds to the last step of stripping. Once it is cooled down, the last peeling step could be proceeded.

But when come to do stripping, we find the template contact way with substrate determines the stripping result. As displayed in Figure 2.19, if the contact as Figure 2.19 (a), the substrate is covered by the template completely, also the polymer diffuses further, and more contact area is filled with the liquid. After UV curing process, the separation is not feasible. So for reaching our aim, we modify the contact way. To diminish the contact area, at the same time, make sure the structure is under template cover, as shown in Figure 2.19 (b) and Figure 2.19 (c). By the latter way, the stripping is easy to be done, and the metal layers are lifted off completely. The stripping result shows it works (Figure 2.19 (d)).

In order to succeed the template-stripping we have to control the spread of the OrmoClearFX: keep the contact area as small as necessary and avoid the spill-off of the polymer outside of Gold-coated area, otherwise after UV curing the separation is no more possible (Figure 2.19 (a)). To reduce the contact surface, control the polymer spread and have a sufficient area for applying the pilling force, we overlap the glass and the Si substrate only partially. This way, the stripping is easy to be done, and the metal layer is piled off completely. The result of stripping is shown in Figure 2.19 (d).

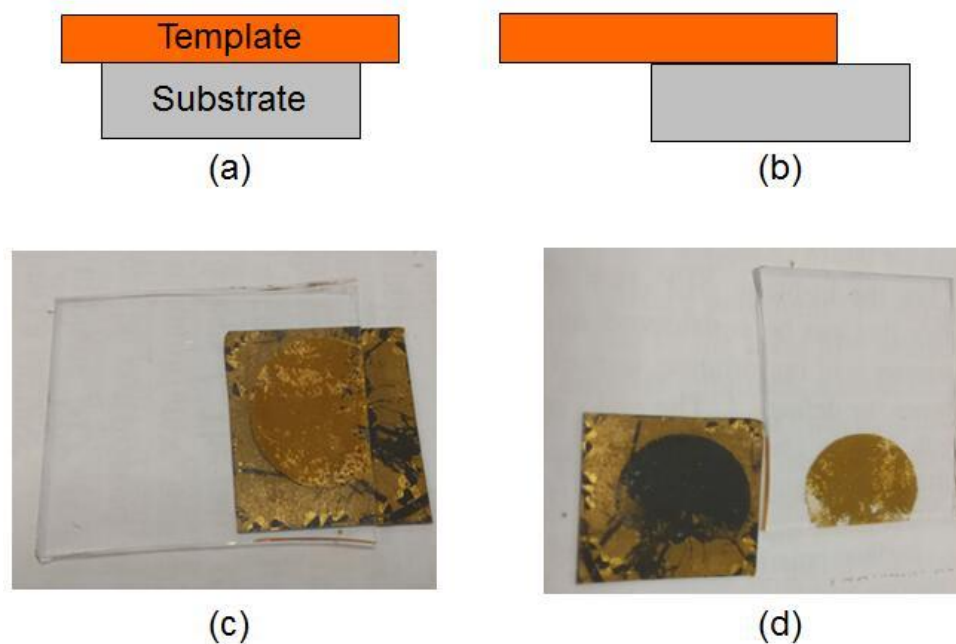


Figure 2.19. Glass contact with substrate and stripping result. (a). Sketch of sample covered by template

completely. The stripping is difficult; (b). Sketch of sample partially covered by glass. (c). Experimental picture of sample partially covered by glass. (d). Stripping result.

After refining the stripping method, the final theoretical W-structure is illustrated in Figure 2.17 (d). At the same time, after the metal stripping, for the sake of checking stripping result, the SEM image of the metal surface is took, as shown in Figure 20 (a). From the image showing result, it seems there is a beautiful metal stripping result. As well, in order to make sure the metal is stripped completely, it is necessary that return to measure the Si surface to check whether there still has metal clinging to the Si substrate. Figure 20 (b) shows the result of the Si substrate surface after metal stripping process. Obviously, the substrate displays us a very clean, smooth and regular consequence. That proves the metal stripping is succeeded and completed.

The overview of successfully stripped surface of Gold W-structure is shown in Figure 20 (a). In order to verify if the metal has been peeled-off completely, we checked the Si template for the residual metal (Figure 20 (b)). The surface is metal-free, clean and the template can be used again. The cross-sectional view of the final metallic W-structure is presented on Figure 20 (c).

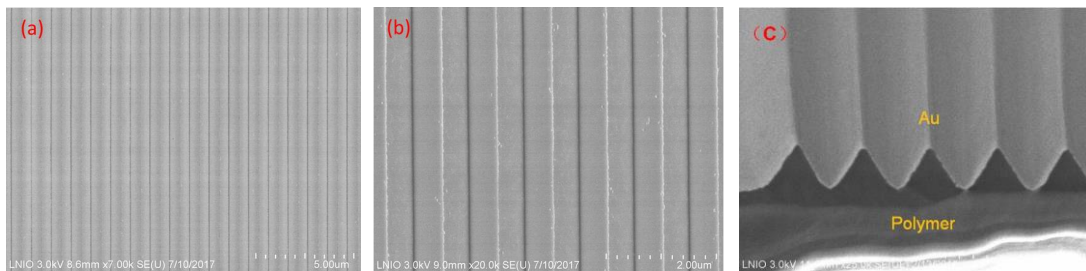


Figure 20. SEM images of metal stripping result: (a) the metal W-structure-top view; (b) Si surface after stripping; (c) the cross-section of metal W-structure.

## 2.8 Summary

To sum up, in this chapter, the theoretical principle and experimental details of W-structure fabrication are described.

The theoretical principle offers the way to fabricate W-structure mold. In fabrication,

HF is introduced to get rid of the “P-layer” which passivates the Si surface wet etching. Meanwhile, the factors impacting etching result are analyzed as well. Alignment deviation between open windows to crystallographic axes orientation can be diminished using CRM and ERM, and that results in repeatable regular and sharp W-structure. Regarding the metal stripping procedure, Ormoproducs are recommended to serve as stripping polymer due to small shrinkage. With refined way of contact of supporting glass slide with Si substrate, the stripping result is as good as expected.

# Chapter 3 Optical properties of the 2D-folded metallic nanolayers

In this chapter, our work majors in analysis measurement and simulation results of “W” structure.

## 3.1 Introduction

One interesting domain of application of our W-shaped nanostructure is the optical/photronics domain. Indeed our ability to fabricate thin W-shaped structures in a precisely controlled manner is of interest for the fine tuning of local field enhancements, the engineering of LDOS (local density of state) or more simply the control of absorbance, reflectance and transmittance. Our structures may also be considered as a particular 2D optical metamaterial.

For these reasons we've conducted a series of experimental and theoretical studies.

Experimentally the structures studied in this chapter consist of W-shaped gold structures deposited onto a glass surface via a polymer of refractive index  $n=1.55$ . We've focused on two samples with a period of 400nm and 600nm. The thickness of gold deposition is 50nm in both cases. The half angle of the wedges of the structure is  $35.3^\circ$ , as described previously.

For all the simulations we will consider that the metallic W-structure is deposited onto a semi-infinite dielectric media of index 1.55.

Our measurement bench allows us to measure the transmission coefficient in the 300-950nm range and for angles of incidence ( $\theta_i$ ) from  $0^\circ$  to  $50^\circ$ .

We've used the power of simulations to explore a larger spectrum of properties than we were able to access experimentally. And the experimental measurements - even though more limited in scope - completely confirmed us that we had a good control on our samples and a good adequation of our simulation methods. Indeed a very good agreement between experimental and simulated data was observed.

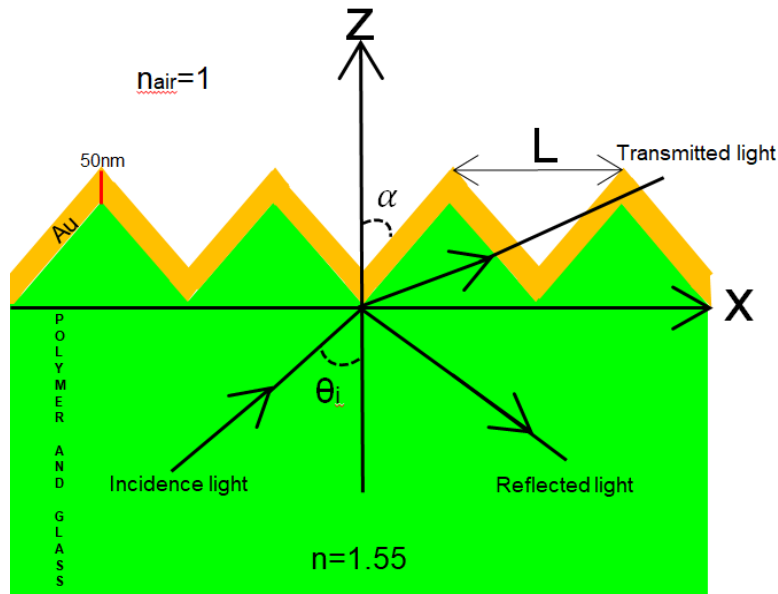


Figure 3.1 Schematic of W structure measurement. The incidence light comes from the side of glass and polymer with relative permittivity 1.55. Gold layer thickness is 50nm as shown in the figure. The periods of structure L are 400nm, 600nm. The half wedge angle  $\alpha = 35.3^\circ$ .

## 3.2 Description of the electromagnetic modeling methods

Due to the practical importance of gratings in optics in particular for their applications to laser and spectroscopy, many theories are available for the study of periodic structures.<sup>108, 109</sup> In most cases a rigorous treatment of vectorial Maxwell equations is required and there exists no simple solution for the general problem of diffraction by periodic structures. Instead there are a number of different theories which all have their qualities and drawbacks. We've chosen to work with the differential method for its versatility and with the Chandezon method for its fast and accurate results in case of structures without high aspect ratios (height divided by period).

### 3.2.1 Properties of the electromagnetic field in periodic media

We limit ourselves to the case of linear homogeneous and isotropic material and we

consider a periodic structure of period  $L$  along the  $x$  axis. The structure is lightened by a monochromatic plane wave coming from the half plan ( $z > 0$ ) with an incidence angle  $\theta_i$  and a wavelength  $\lambda$ . For simplicity of the equations we also limit ourselves to the classical configuration where the plane of incidence is perpendicular to the grooves. This correspond to the most usual and practical configuration. And although the general case, where the azimuth angle  $\Phi_i$  between the normal to the grooves and the plane of incidence is not nul, may present some interest, we didn't have time to perform such an extensive study yet. Both methods we've used are based on Maxwell equations:

$$\left\{ \begin{array}{l} \text{div } D = \rho \\ \text{rot } E = -\frac{\partial B}{\partial t} \\ \text{div } B = 0 \\ \text{rot } H = j + \frac{\partial D}{\partial t} \end{array} \right. \quad 3-1$$

Which simplifies, when we assume an harmonic dependence of the fields in  $e^{-i\omega t}$ , into

$$\left\{ \begin{array}{l} \text{div } D = \rho \\ \text{rot } E = i\omega B \\ \text{div } H = 0 \\ \text{rot } H = j - i\omega D \end{array} \right. \quad 3-2$$

which is a 1st-order differential system which now depends only on space variables.

It can be shown that in a periodic media of period  $L$  along  $(Ox)$ , all the field components present a pseudo periodicity,<sup>110, 111</sup> which is a periodicity with an additional phase shift corresponding to the incident field in case of abnormal incidence. Mathematically the pseudo-periodicity of the fields is expressed by

$$u(x, z) = \sum_{n=-\infty}^{+\infty} u_n(z) e^{i(nK + k_0 \sin \theta_i)x} \quad 3-3$$

where  $u$  designs any field  $E$ ,  $B$ ,  $D$  or  $H$ .

In the homogeneous zones surrounding the periodically modulated region, below (the substrate) and above (the superstrate), it can be shown that the field can be written as a sum of plan waves <sup>110, 111</sup>,

$$E(x, z) = \sum_{n=-\infty}^{+\infty} [A_n^- e^{i(\sigma_n x - \beta_n z)} + A_n^+ e^{i(\sigma_n x + \beta_n z)}] \quad 3-4$$

with the  $A^+$  coefficients corresponding to waves propagating in the direction of  $(Oz)$  and  $A^-$  the waves propagating in the direction opposite to  $(Oz)$ .

### 3.2.2 Differential method

The differential method considers directly the set of Maxwell equations, combined with a decomposition of the fields into Fourier series. This leads to an infinite set of differential equations, with values of  $n$  from  $-\infty$  to  $+\infty$ . Since we're dealing with Fourier series, the high value of  $n$  corresponds to the description of high spatial frequencies of the field and the structure.

This infinite system can also be truncated between the values of  $n$  between  $-N$  and  $+N$ . Where,  $N$  is the truncation parameter which has to be chosen in order that the truncated Fourier series still represent correctly the field and the structure. The choice of this parameter is important since the calculation time will be proportion to  $N^3$ .

Once the system is truncated, the system appears as a system of 1<sup>st</sup> order coupled differential equations of one variable  $z$ , which correspond to the optical axis.

Many algorithms are available to solve this type of system, for instance the Runge-Kutta method. But the initial conditions has to be known at one initial position  $z_0$  which is not so obvious since even if we take the side of the incident field, the total field is the sum of the incident field (which is known) and the diffracted field which is unknown. Here some tricks have to be applied that we won't go into details, the reader can refer to <sup>112, 113</sup> for more information on this point.

The differential method has known several improvements since its first formulation,

such as the efficient S-matrix algorithm <sup>114</sup> for dealing with thick samples and the use of appropriate factorization rules of the Fourier series <sup>115,116</sup> for faster convergence. All these improvement is included in the computer code we are using. We again refer the reader to <sup>112,113</sup> for more details on these aspects.

One advantage of the differential method is that it is not restricted to a particular situation and can deal with metals, dielectric, anisotropic, structures with many materials or continuously varying media. It belongs to the class of rigorous electromagnetic methods. One of the weak points of the method is that it is quite numerically intensive which makes it less suited to big diffracting structure. It can also present some numerical instability in the case of highly conductive materials, such as many metals in the infrared region.

### **3.2.3 Chandezon method**

The Chandezon method (also called C method) was first introduced in 1980 by Chandezon <sup>117,118</sup> and later received numerous improvement by various authors. <sup>119-124</sup>

The method is based on the introduction of a new coordinate system that maps the grating surface to a planar surface, making the matching of boundary conditions easy, and transforms Maxwell's equations in Fourier space into a matrix eigenvalue problem. Consequently, numerical solution of the grating problem is straightforward. The C method is applicable to a large class of grating surface profiles, and it is perfectly adapted for modeling multilayer coated gratings. Its convergence is fast and low strong dependence on the incident polarization or permittivity of the medium.

We've used the C method via a commercial software called MC grating <sup>125</sup> and mostly used it for the determination of the local fields.

In our case, both the differential method and the C method are able to solve the problem and give similar results.

### 3.3 Measurements of light transmission through the W-structure in the visible range

Light transmission through the fabricated gold W-structures was measured in the visible and near infrared range (400-950nm) using a polarimetric bench for several angle of incidence. We present here the measurement method and the experimental results for the W samples with a period of a 400nm and 600nm.

The transmission coefficient is defined by  $T = I_T/I_o$ , where  $I_T$  is the transmitted intensity,  $I_o$  is the incident one and its value is expected between 0 and 1.

#### 3.3.1 Description of the measurement setup

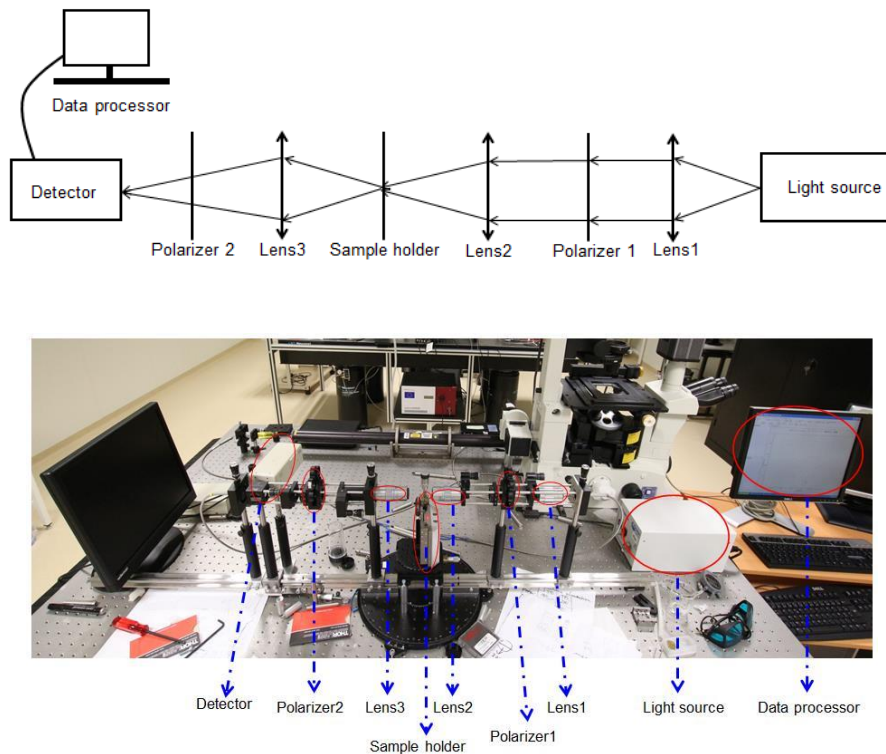


Figure 3.2 Schematic (up) and practical (below) diagrams of measurement machine. Broadband white light source with wavelength from 300-950 nm is used. TE and TM lights can be set by polarizer 1 and polarizer 2. Incidence angle is determined by rotating sample holder from  $0^\circ$  to  $50^\circ$ . Ocean Optics SpectraSuite software is used for analysis.

The extinction spectroscopy bench used for the transmission measurement is shown in fig 3.2. Focus and straight optical line can be got by changing the three lenses and sample holder. Two polarizers are used to select the TM (p-polarisation) and TE (s-polarisation) polarisations. Ocean Optics SpectraSuite software installed in computer plays the role of analysing the optical signal captured by detector. Of course, the corresponding data can be exported from the software.

### **3.3.2 Description of the experimental results**

Transmission through the gold W-structures of 50 nm thickness on a polymer + glass substrate and periods of 400 nm and 600 nm W-structures were measured in the 400-950 nm range for incident angle from  $0^\circ$  to  $50^\circ$  and for both linear polarizations TM (p) and TE(s).

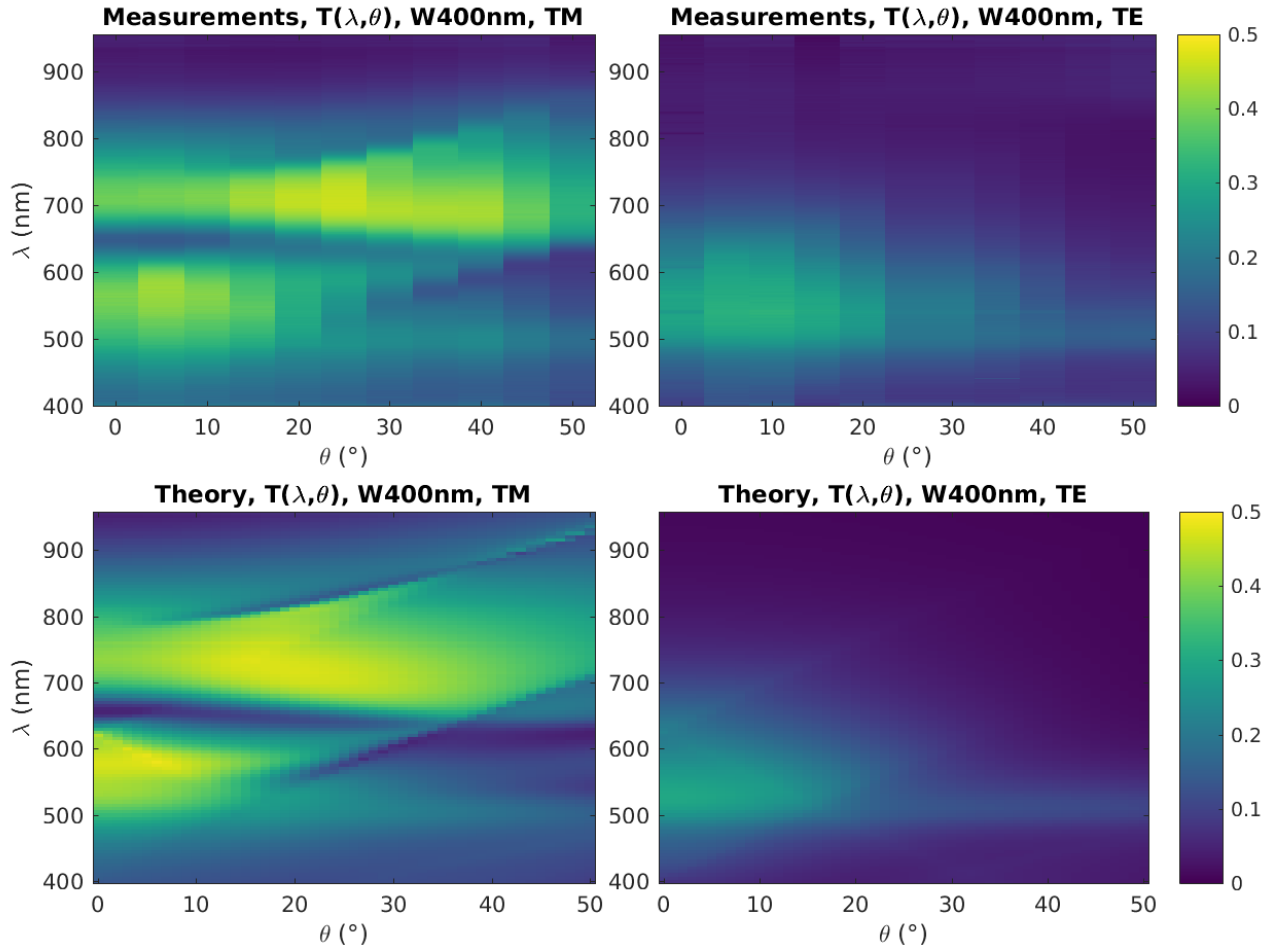


Figure 3.3 Transmission coefficient of a gold W structure with a 400nm period and a 50nm thickness in the visible and near IR(Infrared radiation) range (400-950nm, vertical axis) and for various incidence angle from  $0^\circ$  to  $50^\circ$  (horizontal axis). Measurements (top) and calculations using the differential method (bottom) for both linear polarizations TM (p) on the left and TE (s) on the right. The colour scale is the same for left and right figures.

Figure 3.3 shows a map of the transmission coefficient as a function of the incidence angle and wavelength.  $T(\theta, \lambda)$ , for the W-structure with a period of 400 nm. For these calculations 40 harmonics with a spatial discretization of 1 nm are used.

Experimental results are presented on the first row and theoretical ones calculated with the differential method on the second row. TM results are presented on the first column and TE on the second one.

A good agreement is observed between experiments and theories both for the shape

of the variations as a function of  $\theta$  and  $\lambda$  and for the absolute values of the T coefficients (the color-scale is the same for theory and measurement and for TE and TM).

The transmission coefficient is globally higher in magnitude for the TM polarization than for the TE. It is also much higher than the transmission coefficient of an equivalent flat gold layer of 50nm thickness (Figure 3.5) both for TM and TE.

A complex shape of the variation as a function of  $\theta$  and  $\lambda$  is observed, especially for TM polarisation. Also some clear lines appear in the map and seem to delimitate regions. All these features will be commented further in the next section on the theoretical properties of the far field.

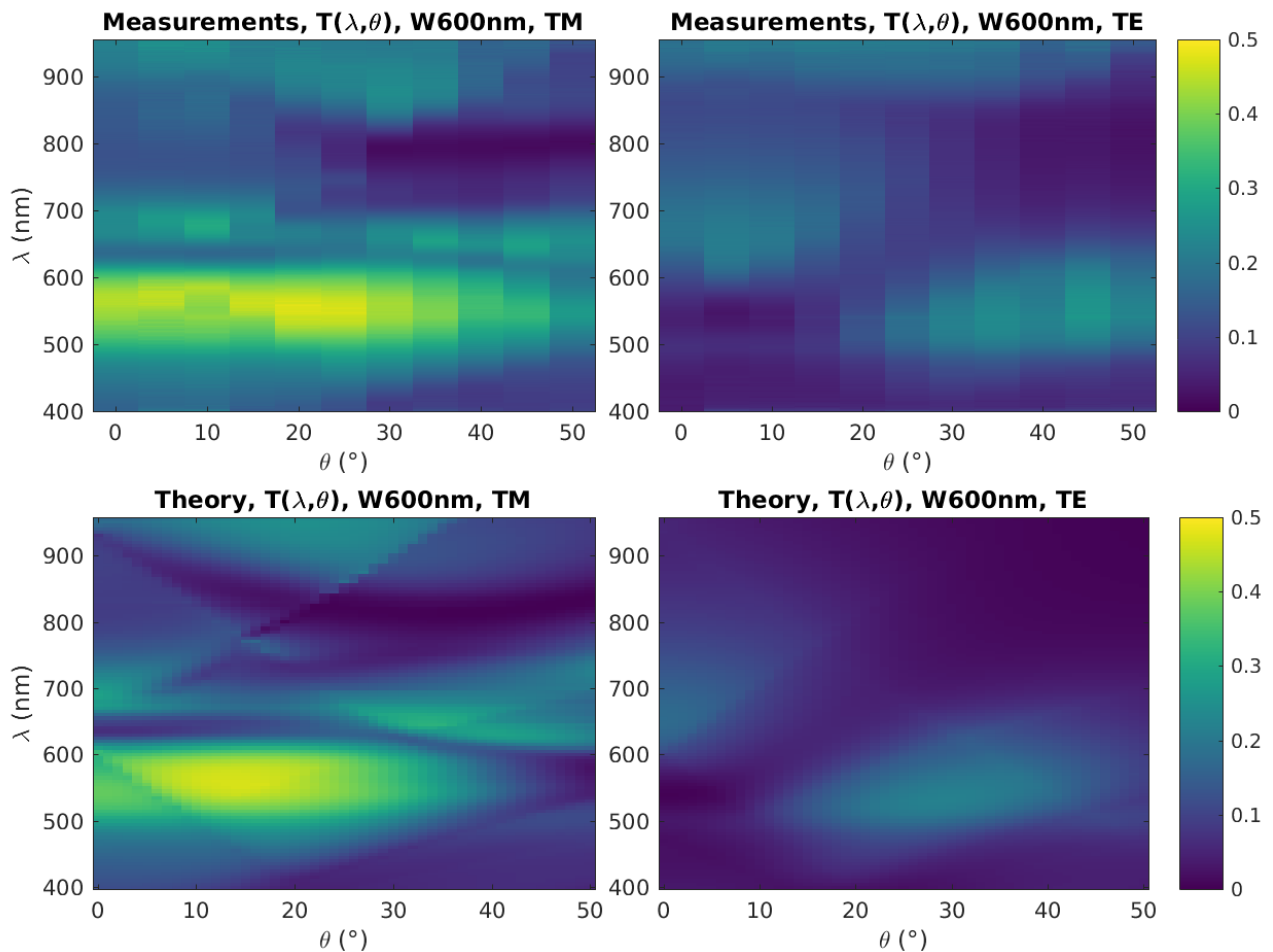


Figure 3.4 Same as Figure 3.3, but for a W structure with a 600nm period.

Figure 3.4 shows the transmission through the W-structure with a period of 600 nm.

Similar comments apply than for the 400nm one. A good agreement is also observed between measurements and theory. An even more complex shape is observed than for the W-400nm. This is due to a larger number of diffracting numbers.

We can also notice a slight horizontal shift of 5-10°, between the theoretical and experimental figures. This is observed both for W-400nm and W-600nm and is likely due to an error of alignment of the sample in the measurement bench.

Figure 3.5 shows the measurement and calculation of the transmission through a single flat gold layer of 50nm thickness. In comparison, the shape of the variation of the transmission coefficient for a W-structure of same thickness is more complex and more intense. Notice that for these flat layer results, we observe the same shapes of the variations between experiments and theory, but a discrepancy for the absolute intensity of the signal. We expect that this discrepancy comes from a calibration error in our measurements but we didn't have time to check again the experiment and we present the results as it is. In this case, the theoretical calculations were validated after been checked by two different methods: the Fresnel coefficients method (not shown, but same results) and the differential method.

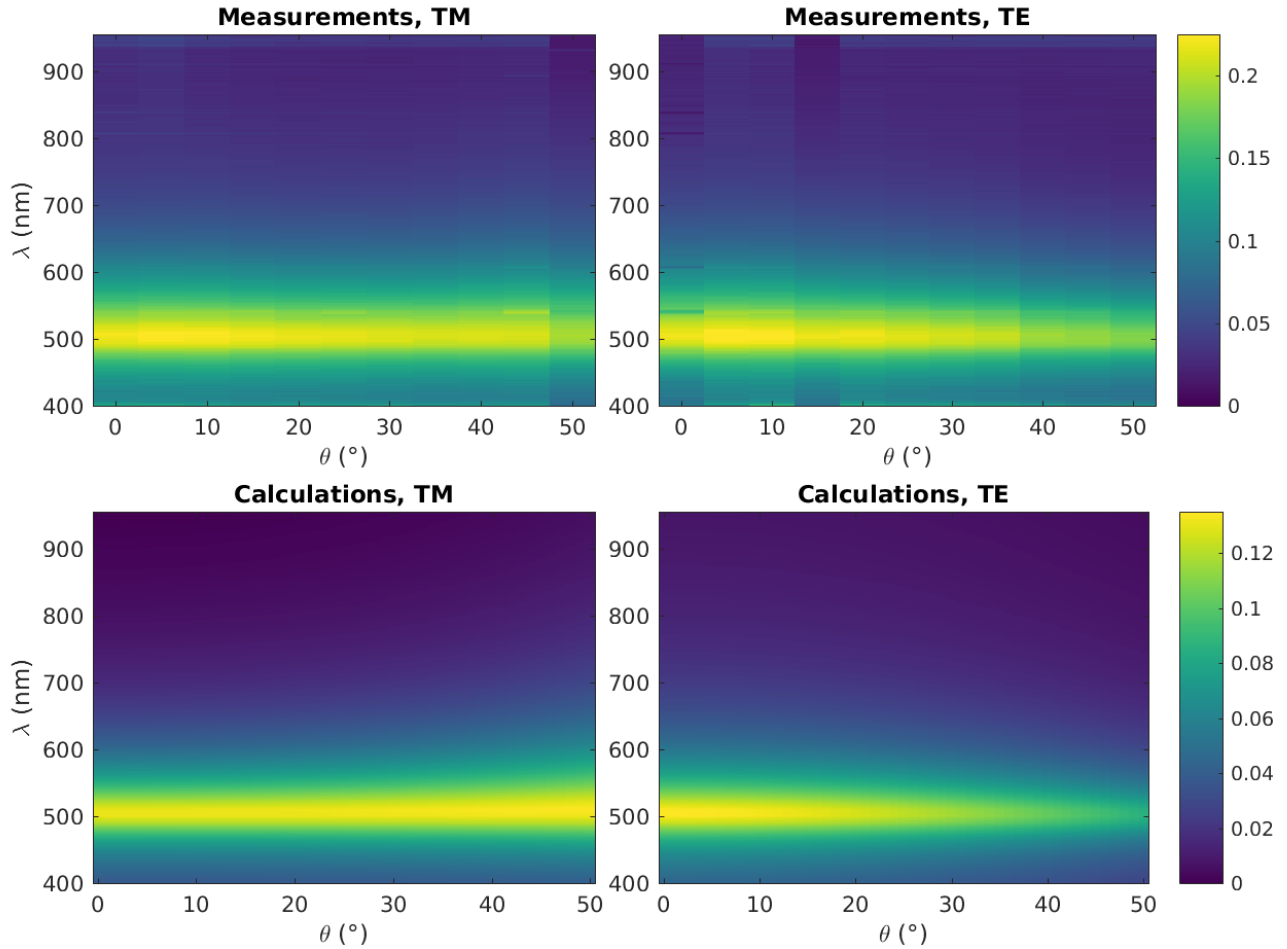


Figure 3.5 Transmission coefficient measured and calculated for a 50nm thick gold layer on a glass substrate for both polarizations (the same color scale is used for left and right columns).

### 3.4 Far field properties of the gold W-structures obtained by electromagnetic modeling

In this section we rely on the electromagnetic simulation to study the far field properties, beyond what we were able to measure in the previous section. In particular we can calculate the reflection coefficient and the absorption and we are able to reach incidence angles that were beyond our reach experimentally.

For all results presented in this section, we consider the light to be incoming from the dielectric substrate with a refractive index  $n=1.55$ , while the upper medium is constituted by air. Instead of light from the air, we use this configuration for the

simulations since it allows us to reach larger longitudinal projections of the wave vector when the incidence angle is high and thus to access a more complete information.

### **3.4.1 Effect of the existence of diffraction orders on the variation of the absorption, reflection and transmission coefficients**

A crucial property of a periodic structure or grating is the possibility of existence of diffraction orders in some particular discrete directions, depending on the incidence angle, the wavelength and period. These orders are a direct consequence of the pseudo-periodicity of the field (cf. the theoretical properties of the field in a periodic structure presented earlier). In a simpler approach, the diffraction orders are also viewed as the directions of constructive interferences resulting from the diffraction by the grating.

The relation between the direction of the order  $\theta_m$ , the angle of incidence  $\theta_i$ , and the period of the grating  $L$  is

$$k_m = k_0 \pm mK \quad m \in (0,1,2,3 \dots) \quad 3-5$$

$$n \sin \theta_m = n_0 \sin \theta_0 \pm m \lambda/L \quad 3-6$$

For a given incidence angle  $\theta_i$ , there is a certain wavelength above which the diffraction order  $m$  will cease to exist. Such value of wavelength corresponds to when  $\theta_m$  goes below  $-90^\circ$  for a negative order or beyond  $+90^\circ$  for a positive order and its value is

$$\lambda = \frac{L}{m} (n \sin \theta_m - n_1 \sin \theta_i), \quad \theta_m = \pm 90^\circ \quad 3-7$$

(where  $m$  is the index of the order,  $n_1$  is the refractive index of the incoming wave medium and  $n$  is the refractive index of the medium of the diffraction order)

When we superimpose these curves corresponding to the limits of existence of the diffraction orders, we observe that they correspond well to some discontinuities or rapid variations that are observed in the maps  $f(\theta, \lambda)$ .

Physically this can be interpreted as the fact that when an order is no longer propagative, there is a redistribution of its energy into some propagative orders. Although there is no simple rule and only a complete electromagnetic calculation can give an accurate picture of what is exactly happening.

Figure 3.6 shows the absorption calculated by the differential method for the W-400nm gold structure. We can see that the limit of existence effectively delimitate various zones in the figure, but it is not enough to describe it and obviously some more complex phenomena are also happening and are traduced by complex variations in the absorption as a function of  $\theta$  and  $\lambda$ . Again, as was observed experimentally with the transmission, the variation is more intricate in TM than in TE. This is expected since in this polarization we have some confinement and resonance effects due to the interaction between the shape of the structure and the electric field, while in TE the electric field is parallel to the grooves.

Figure 3.7 shows the absorption for the W-600nm grating and again we observe an even more intricate pattern, which is expected due to a larger number of diffraction orders with a larger period.

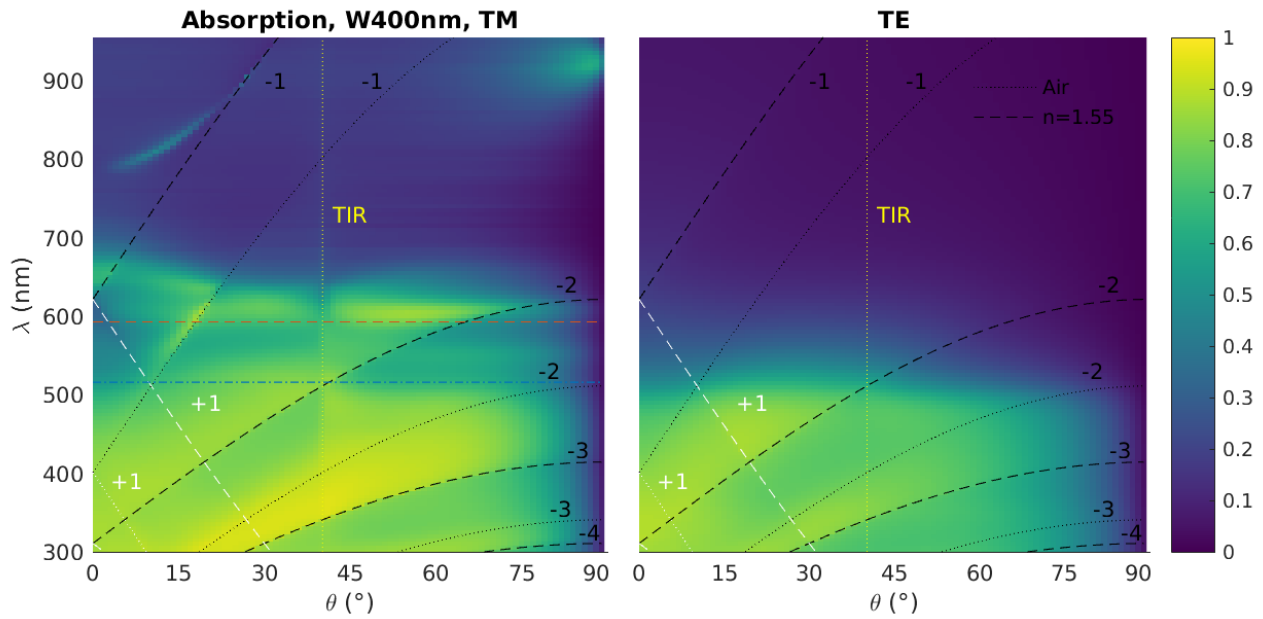


Figure 3.6 Absorption calculated for the gold W-structure with a period of 400nm for TM and TE polarizations.

Black and white, dashed and dotted lines corresponding to the limit of existence of diffraction orders are superimposed to the map and correspond to some variation which is discussed in part 3.4.1 The blue and red horizontal lines at wavelength of 516nm and 593nm correspond to approximate theoretical resonances of gold corner in air and glass respectively, which will be discussed in part 3.5.2. The vertical yellow dot line at 40.2° corresponds to the Total Internal Reflection (TIR) angle from glass ( $n=1.55$ ) to air.

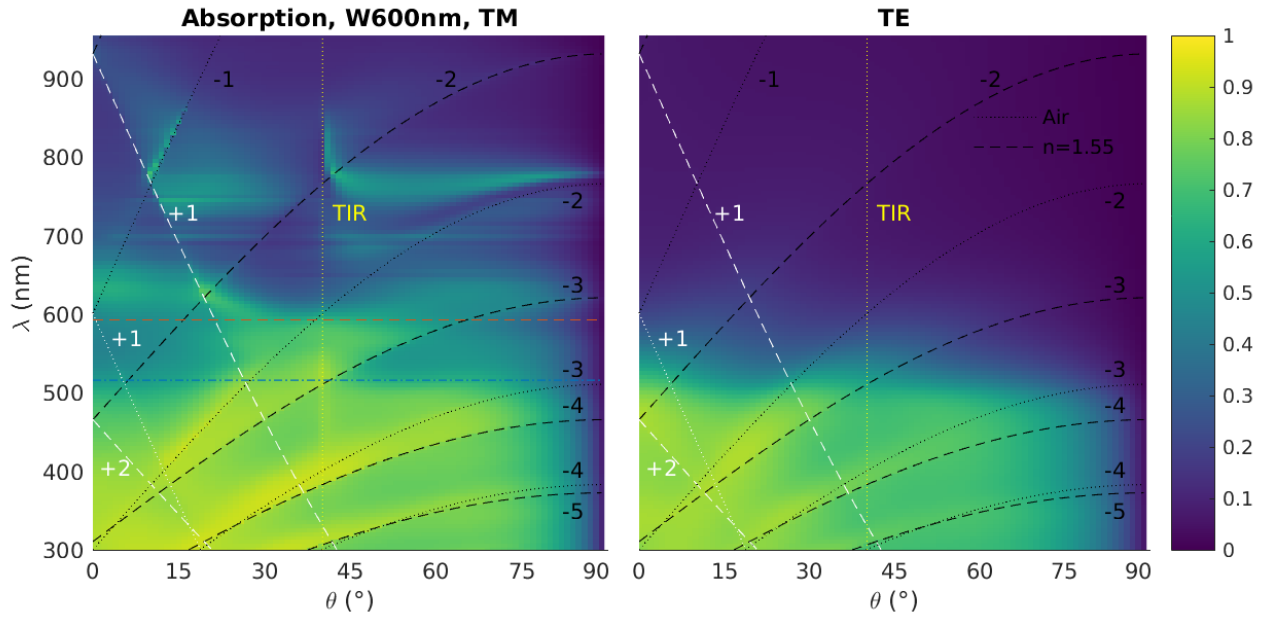


Figure 3.7 Same as Figure 3.6. For a gold W-structure with a period of 600nm.

### 3.4.2 Repartition of the energy between the diffraction orders

Figure 3.8 illustrates an interesting phenomena happening for the reflected diffraction orders in TE polarization for the W-400nm structure: we observe a transfer of energy towards higher diffraction orders when they exist. Roughly speaking, the (0) order (ie the specular reflection) presents two zones of high values: the one where there the grating is subwavelength (above the (-1) order limit) and the one at high incidence angle. If we expect this zone of high incidence angle, near  $\theta_i=90^\circ$ , we observe a clear complementarity of energy between the orders and a tendency of the light to go into the higher order possible. We do not have a simple explanation for that.

In this regarding the TM polarization is not as clear, especially for the (-1) order which presents a very intricate pattern. Contrary to the TE case, a significant part of the energy remains in the (0) order.

In Figure 3.8 and 3.9, the red dashed lines correspond to the condition of back propagation in the direction of incidence for the considered order. This criteria is part

of the Littrow condition used for maximizing the diffraction efficiency of blazed gratings for a particular order. For a given incidence angle and order  $m$ , this condition is obtained for a wavelength

$$\lambda_{\text{Littrow}} = \frac{L}{|m|} \cdot 2n_1 \sin \theta_i \quad 3-8$$

Here we observe that the local maximum efficiency of a diffraction order often correspond to this particular condition (cf. Figure 3.8 and 3.9).

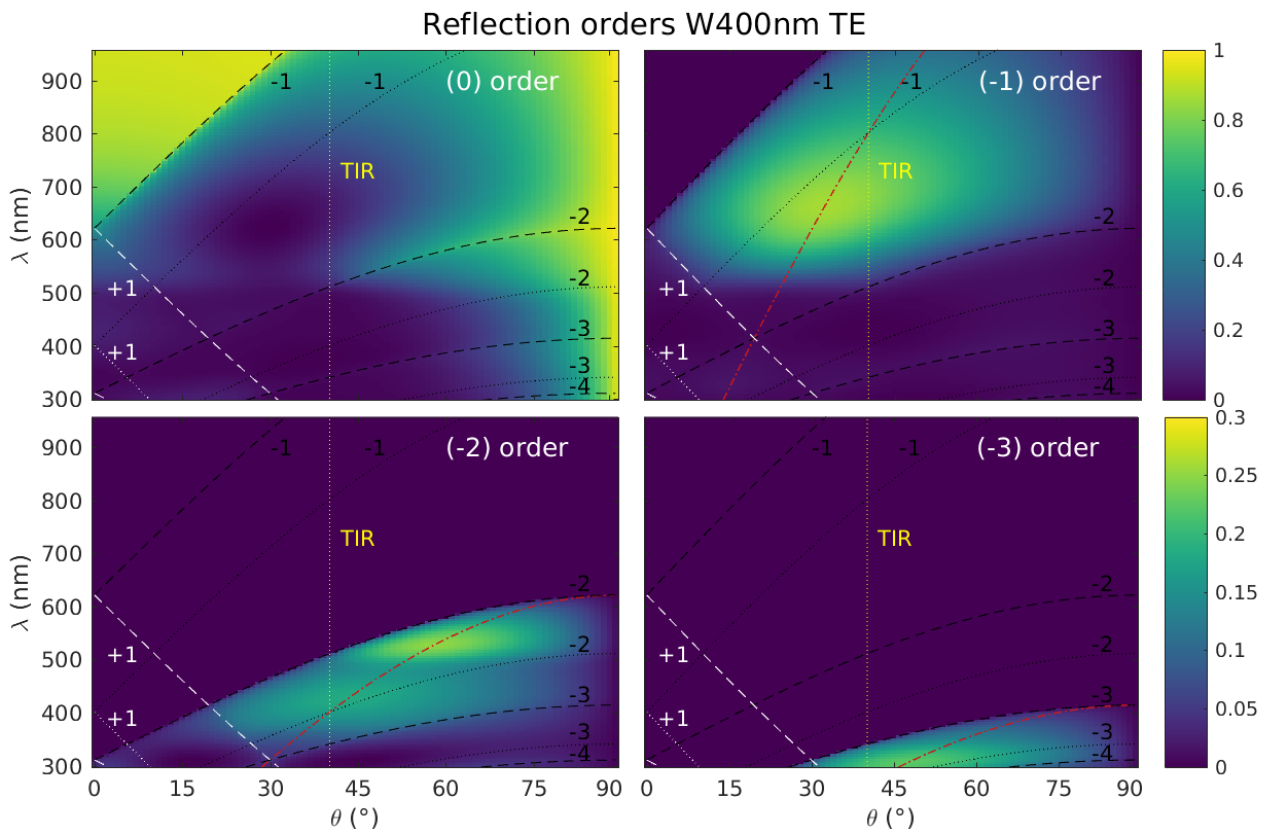


Figure 3.8 Diffraction order in reflection for the gold W-structure of 400nm period in TE polarization for each order between (0) and (-3). The red dashed curve corresponds to the condition of back-propagation in the direction of incidence for a given order.

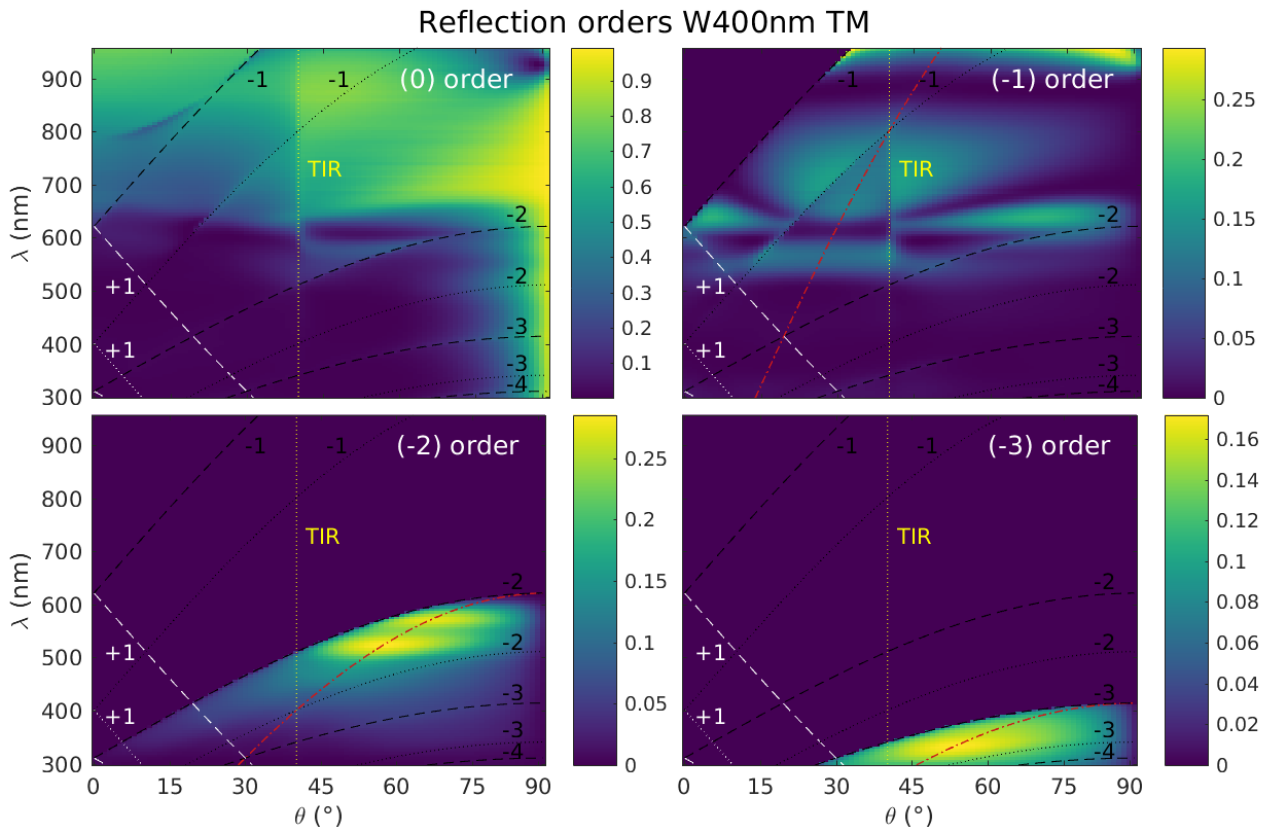


Figure 3.9 Same as Figure 3.8 for TM polarization.

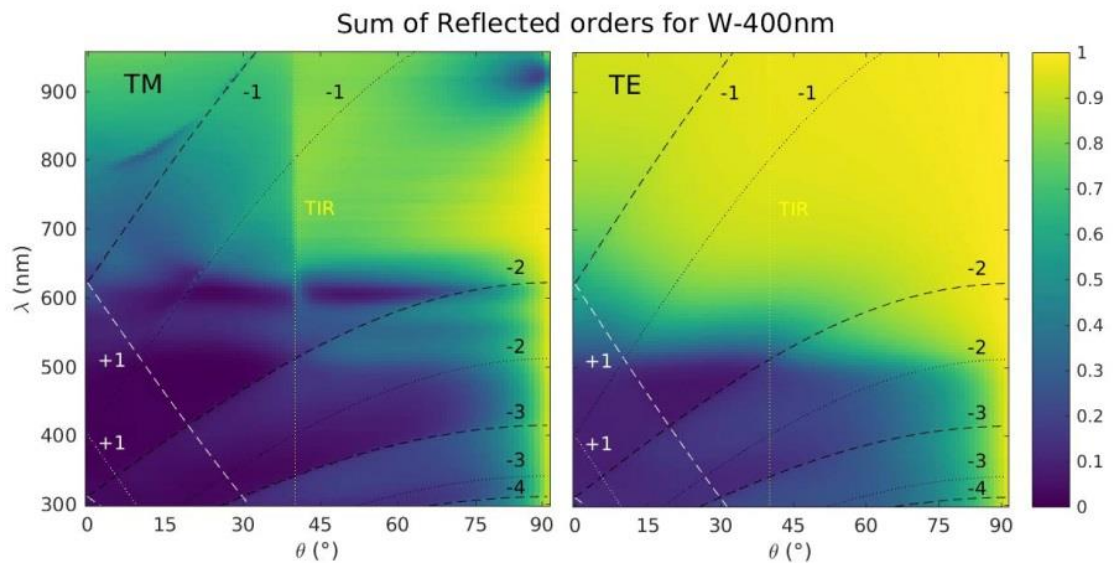


Figure 3.10 Sum of all reflected orders efficiencies presented in figures 3.8 and 3.9 for TM and TE, ie total reflected energy.

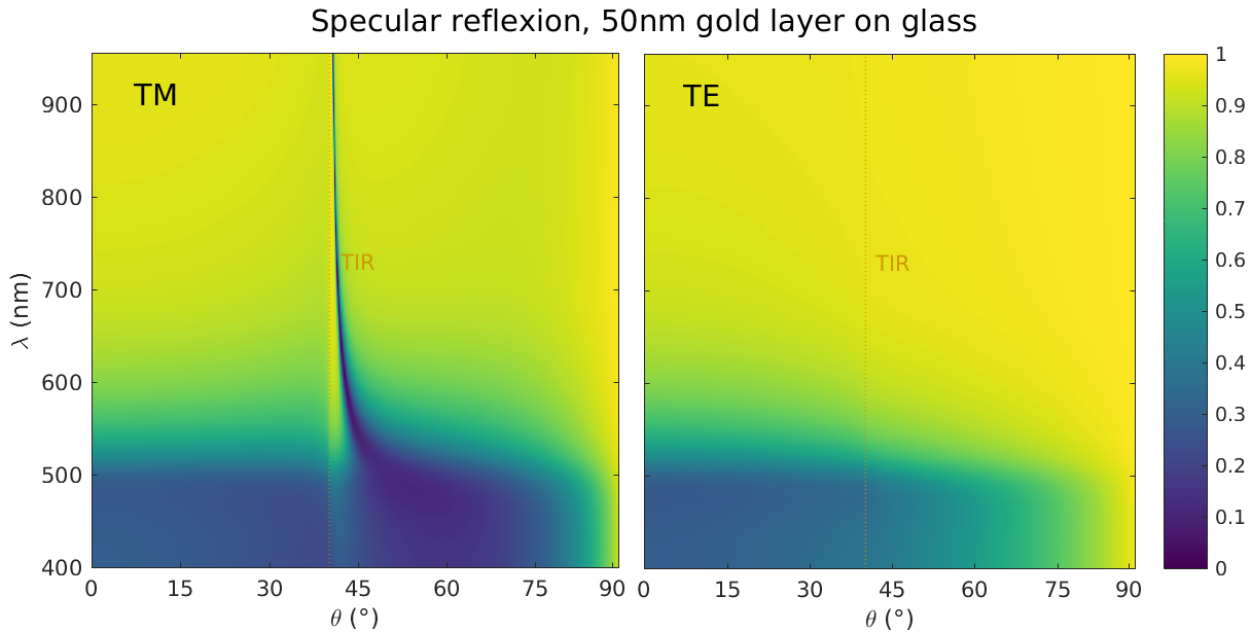


Figure 3.11 Reflected intensity of a thin film of gold on a glass ( $n=1.55$ ) substrate. Same conditions are for the W-structures for comparison purpose. The light is coming from the glass medium. In TM image, for incidence angle above the Total Internal Reflection (TIR), the peak corresponds to the Gold-Air interface SPR dispersion curve.

### 3.5 Local field properties of the gold W-structures obtained by electromagnetic modeling

So far we've seen that the origami gold W-structures present complicated variations in their far-fields properties, especially in TM where the electric field may resonant with the structure. Surely many of the effects observed in the far field are linked to specificities of the local field such as surface plasmons polaritons resonance at the edges and angles of the structure. These effects are interesting to study, not only because they complete the comprehension we have about these structure, but also because their properties may allow for interesting applications such as biosensor through chemical functionalization of the metallic surface.<sup>126</sup>

Also not only the W-structure presents many edges and corners but its periodic

nature makes natural the coupling from a far field free propagating incident light into higher order spacial frequencies, without the use of a prism such as in a Kretschmann or Otto configurations.<sup>127</sup> Existence of guided modes or coupled-chain mode<sup>128</sup> is possible inside such a structure and is worth to be studied.

### 3.5.1 Identification of the wavelngths and angles of incidence of interest

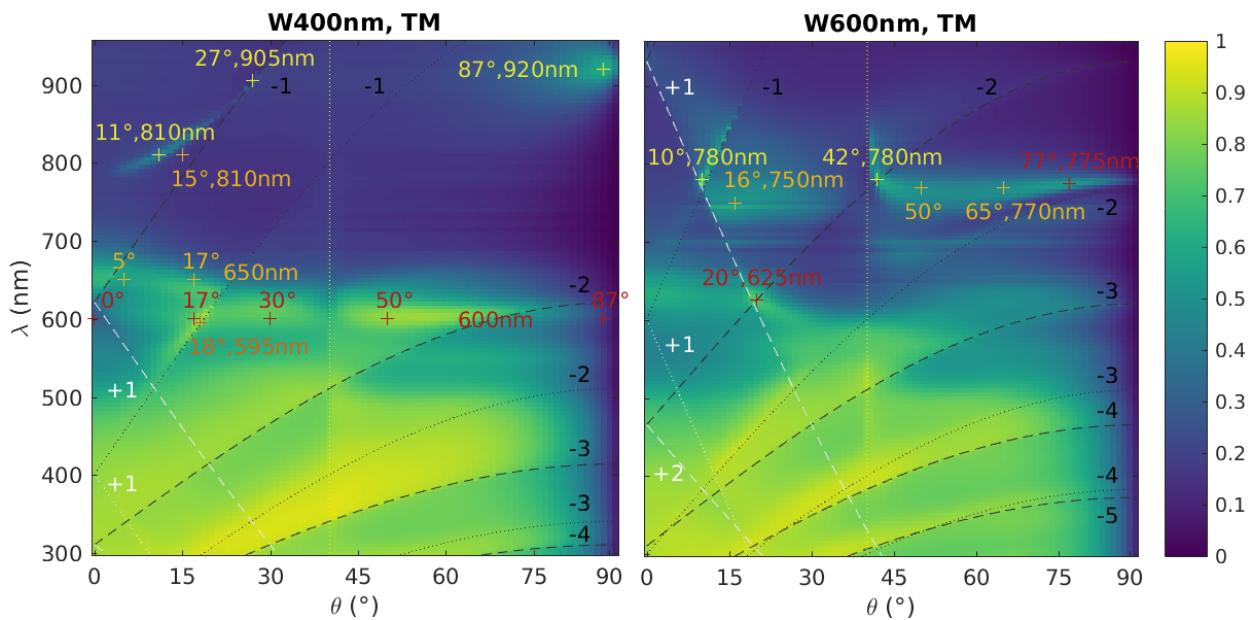


Figure 3.12 Absorption maps for W-400nm and W-600nm in TM with indication of points of interest where we've chosen to calculate the local field inside and around the structure. Corresponding local field maps are presented in this chapter or in Annex.

In order to select the points of interest for the study of the local field, we've chosen to rely on the absorption map. Indeed some particular zones with increased absorption may signal local resonances in enhanced local fields. Figure 3.12 shows the points we've selected for the local fields representations.

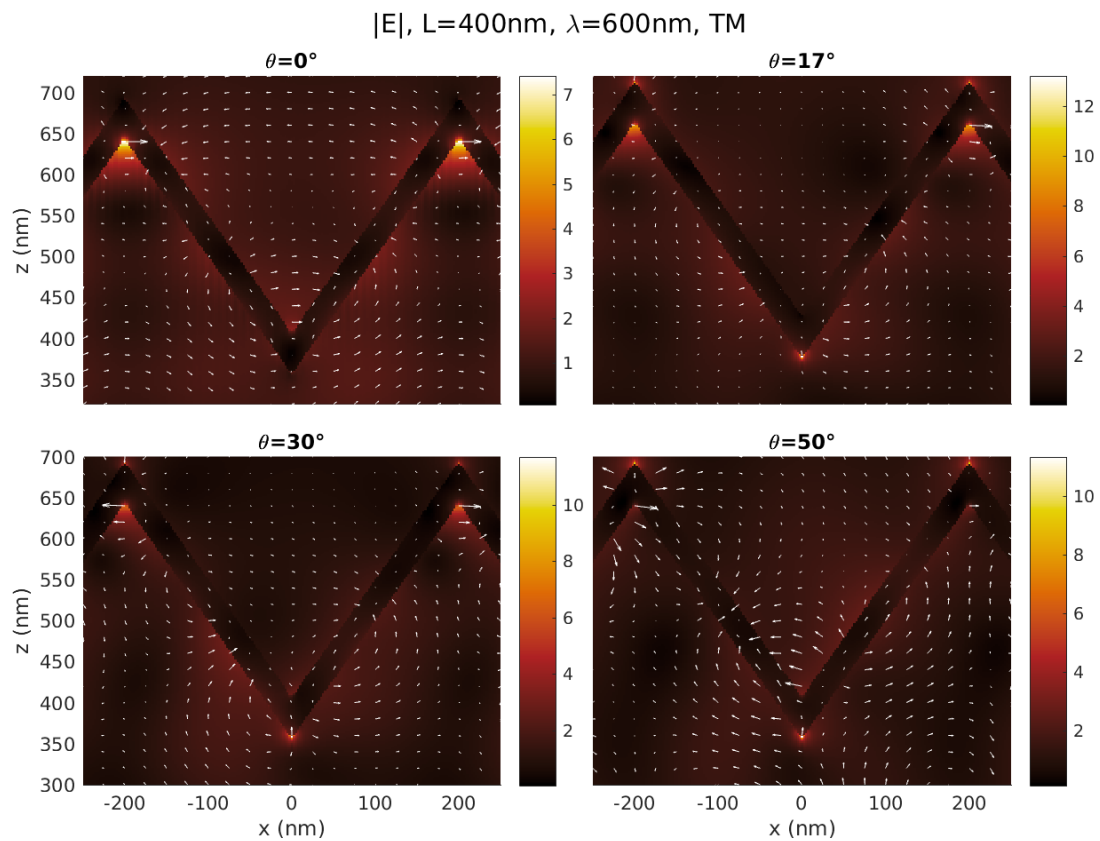


Figure 3.13 Amplitude of the local electric field for a wavelength of 600nm and various angles in TM polarization.

The vector field represents the direction of the electric field at a particular and arbitrary moment in the periodic cycle . The incident electric field amplitude is equal to 1.

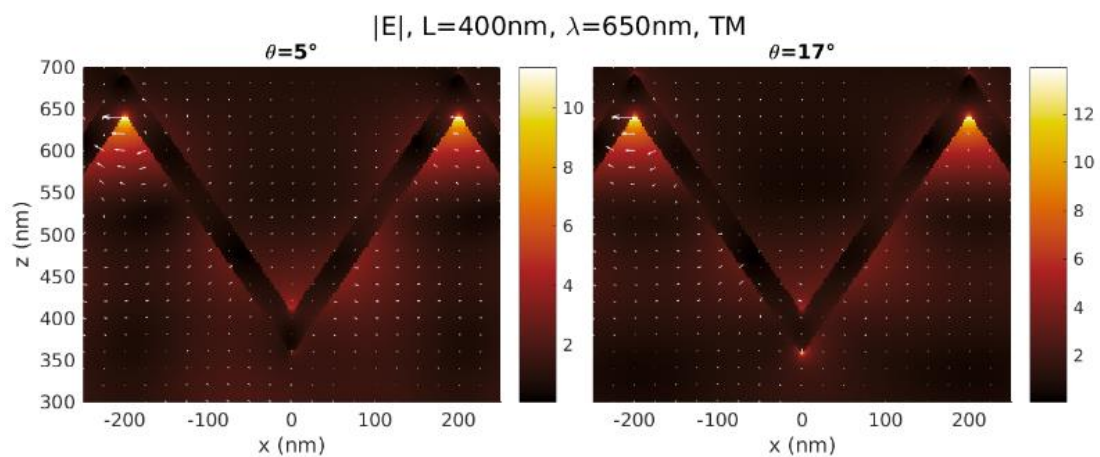


Figure 3.14 Amplitude and instantaneous direction of the local electric field for a wavelength of 650nm and angles of incidence of 5° and 17° in TM polarization. Notice the field enhancement at the bottom tip and the directions of the electric fields in the upper corner.

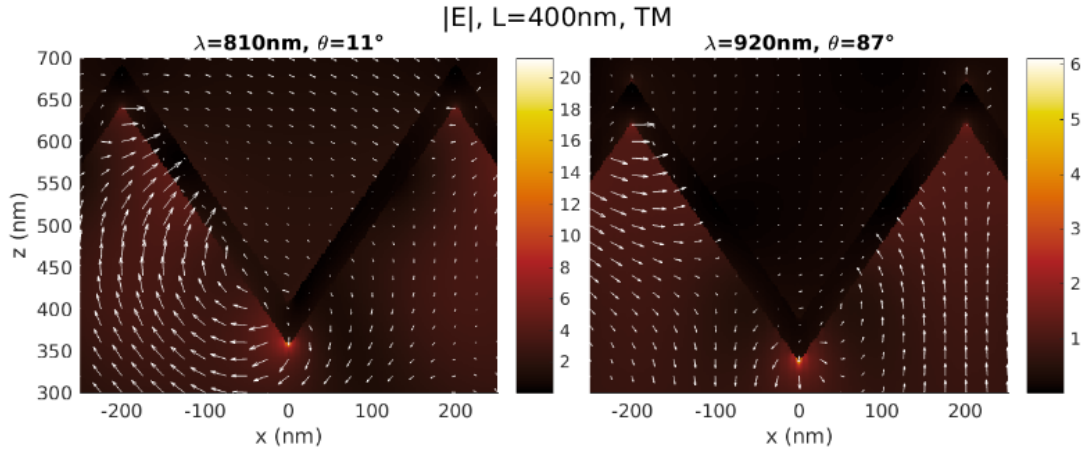


Figure 3.15 Amplitude and instantaneous direction of the local electric field for a wavelength of 810nm and an incidence of 11° and a wavelength of 920nm and an incidence of 97° in TM polarization.

### 3.5.2 Theory of wedge resonances

Although no analytical theory is available for the description of the resonances in the structures we are studying, it is possible to derive an analytical formulae in the simpler case of a corner forming an interface between two semi-infinite media. Geometrically, this corner can be described as resulting from the folding along a 1D line of a plan delimitating two semi-infinite media.

Given that one of the media is a metal of permittivity  $\epsilon_m$  and the other media is made of a material with a permittivity  $\epsilon_1$ , the resonance is achieved with the condition<sup>129, 130</sup>

$$\text{Re}\left(\frac{\epsilon_m}{\epsilon_1}\right) = 1 - \frac{\pi}{\alpha} \quad 3-9$$

where  $\alpha$  (rad) is the  $\frac{1}{2}$  angle of the corner.

In our case the half angle of the wedge is  $35.3^\circ = 0.616$  rad, which - using the values of the gold permittivity indicated in annex - gives a resonance wavelength of 516.4 nm for the wedge at the contact gold/air and 592.9 nm for the wedge at the contact gold/glass ( $n=1.55$ ).

Moreover, the complementary of this corner at  $\pi - \alpha = 2.525$ rad can also be calculated using this formula. For the interface gold/glass ( $n=1.55$ ) the equation

admits two very close solutions at 337.3nm and 338.2nm and for the interface gold/air, the equation has no solution in the 300-1000nm range for the values of permittivity of gold presented in annex.

This analytical theory does not correspond closely to our intricate W-structure but let's notice that we still observe a horizontal zone of increased absorption around 600nm for the W-400nm gold structure. This is close to the theoretical value of 592.9nm. We also observe a strongly enhanced and very localized local field at the tips of gold in the substrate at this wavelength (Fig 3.13 bottom of the structures). We're not sure yet if we could conclude that this effect is linked to the present theory. Especially we notice that the W-600nm - which presents the same tip's angles - do not clearly reproduce this phenomena. It is also possible that the assumptions of this theory are too far away from the geometry of our W-structure and that the enhanced absorption around 600nm observed for the W-400nm have another explanation.

### **3.5.3 Local fields in the W-400nm and W-600nm gold nanostructures**

Let's remind that for all the simulations presented in this chapter, the light is incoming from the substrate which is a dielectric with  $n=1.55$ , situated below the W-structure on all the local field maps.

Interestingly, for several wavelengths and angles of incidence, the W-400nm gold structure presents strongly enhanced and localized electric fields near the tips or corners. Up to a factor  $\times 20$  is observed for a wavelength of 810nm and incidence angle of  $11^\circ$  (Figure 3.15).

The W-400nm absorption map presents two peculiar zones: one around ( $11^\circ, 810\text{ nm} - 27^\circ, 905\text{nm}$ ) and another one around ( $87^\circ, 920\text{nm}$ ), see Fig 3.12 and Fig 3.15. We do not have yet a complete explanation on the physical phenomena that produces these effects but we observe in both cases an increase in the absorption and a locally strongly enhanced electric field at the tip/wedges between gold and glass. So we may

be in presence of local resonance effect.

As a tendency, the W-600nm structure doesn't show such local enhancement of the field that are observed from the W-400nm. We see that the maximum enhancement factor lies around x5 for the W-600nm, instead of x20 with the W-400nm. The reason for this is not clear to us. One possible explanation would be that due to a smaller size, the modes could couple between themselves easily in the W-400nm, and thus lead to enhance combined resonances. This hypothesis needs more work to be confirmed.

### **3.6 Conclusion**

We've successfully characterized experimentally and by simulations the W-shaped gold nanostructures of 400nm and 600nm period and 50nm thickness. The optical properties present a complicated dependence upon  $\lambda$  and  $\theta$  and a great sensitivity to a variation of geometrical parameters. Numerous effects can be explained by the periodic properties of the structures and by the presence of local plasmon polariton resonances which traduces themselves as very strong localized field enhancement, up to a factor x20, near the wedges or the corners of the structures. Such properties may be of interest in particular in the domain of biosensors, after the bio-functionalization of the gold interface.

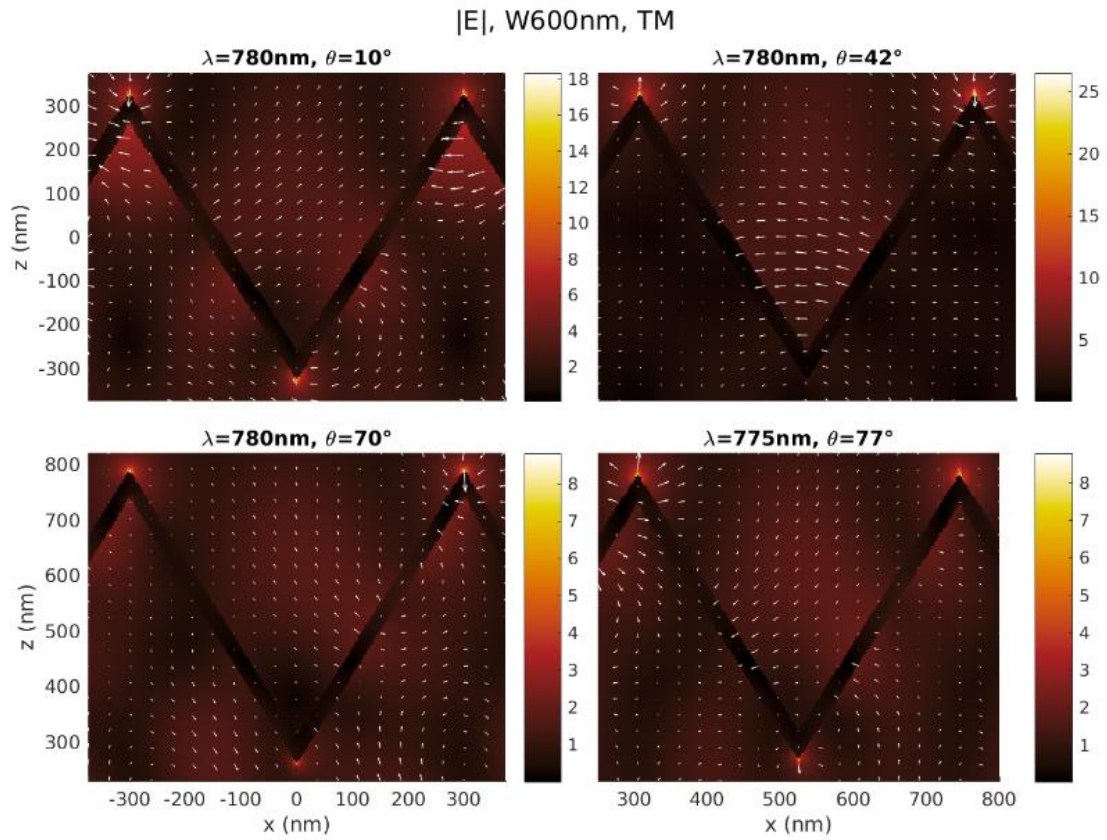


Figure 3.16 Amplitude and instantaneous direction of the local electric field for a wavelength of 780nm and an incidence of  $10^\circ$ ,  $42^\circ$ ,  $70^\circ$  and  $77^\circ$ .

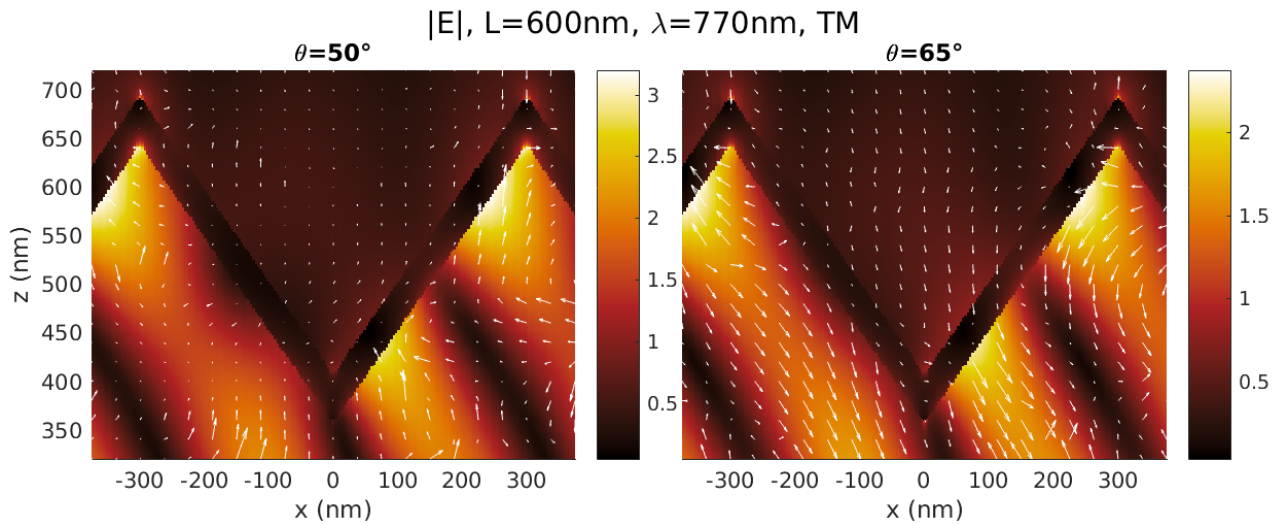


Figure 3.17 Amplitude and instantaneous direction of the local electric field for a wavelength of 770nm and an incidence of  $50^\circ$  and  $65^\circ$ .

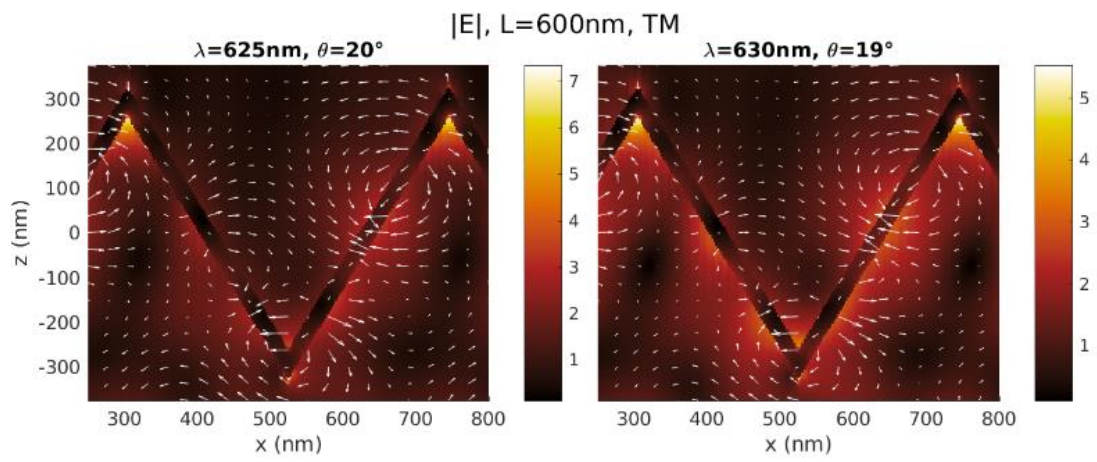


Figure 3.18 Amplitude and instantaneous direction of the local electric field for W-600nm in TM for wavelength of 625nm, 630nm, and angles of incidence of  $20^\circ$ ,  $19^\circ$  respectively.

# Annex

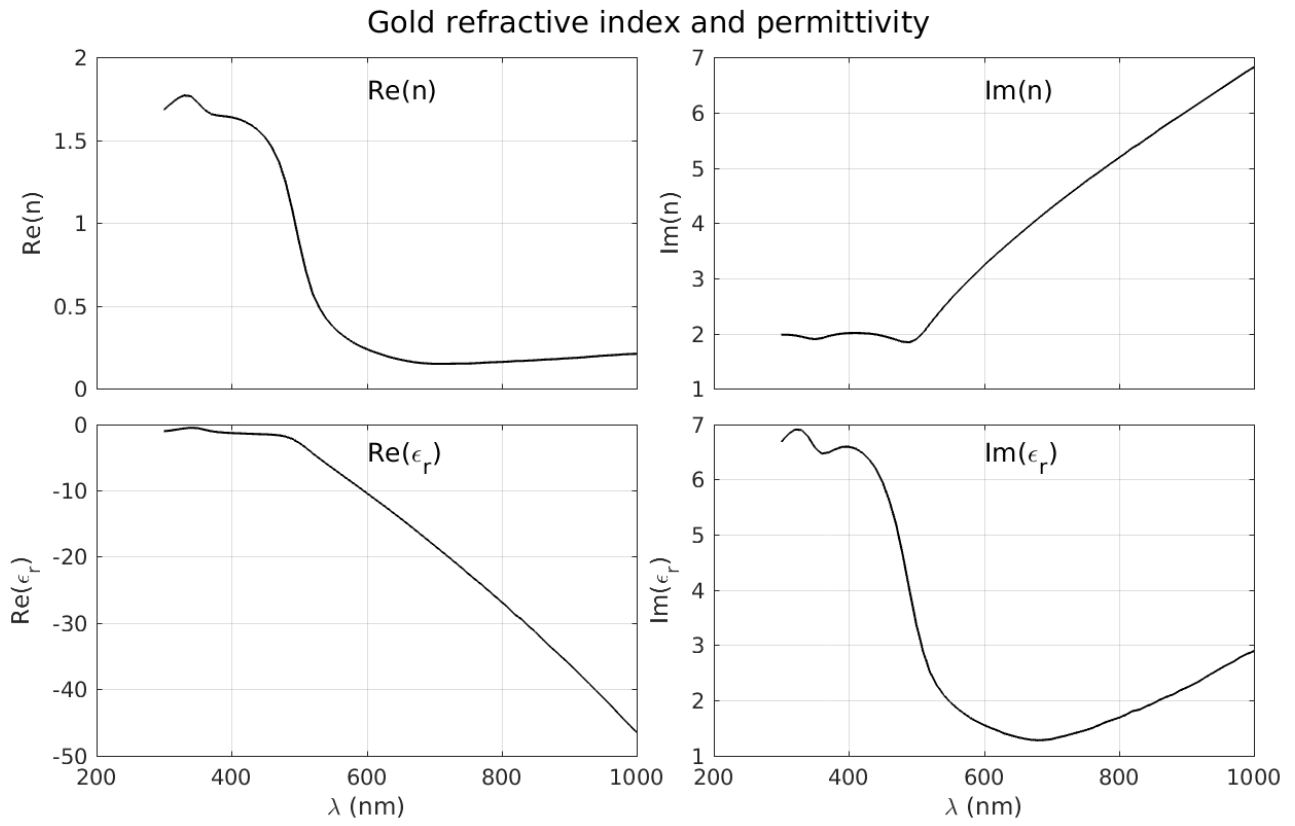


Figure 3.19 Values of gold refractive index and permittivity used for calculations. We used the values provided by <https://refractiveindex.info> from a paper of Yakubosky et al. (2017)<sup>131</sup> obtained for a 53nm thick gold layer.

# Chapter 4 Numerical simulation of tandem solar cells on silicon

In this chapter, first we introduce solar cell background and theory, and advantages of our tandem solar cell structure. Then we describe the method and the software used for the numerical simulation. Based on that, the research about our tandem solar cell is done. Through simulations, we get the relative better device parameters. Finally, we use the parameters to fit the experimental results.

## 4.1 Background

Solar cells used for converting the sunlight into electricity have a promising market and are potential to replace the increasing fossil fuel consumption which gives rise to energy crisis, global warming and other attendant problems.

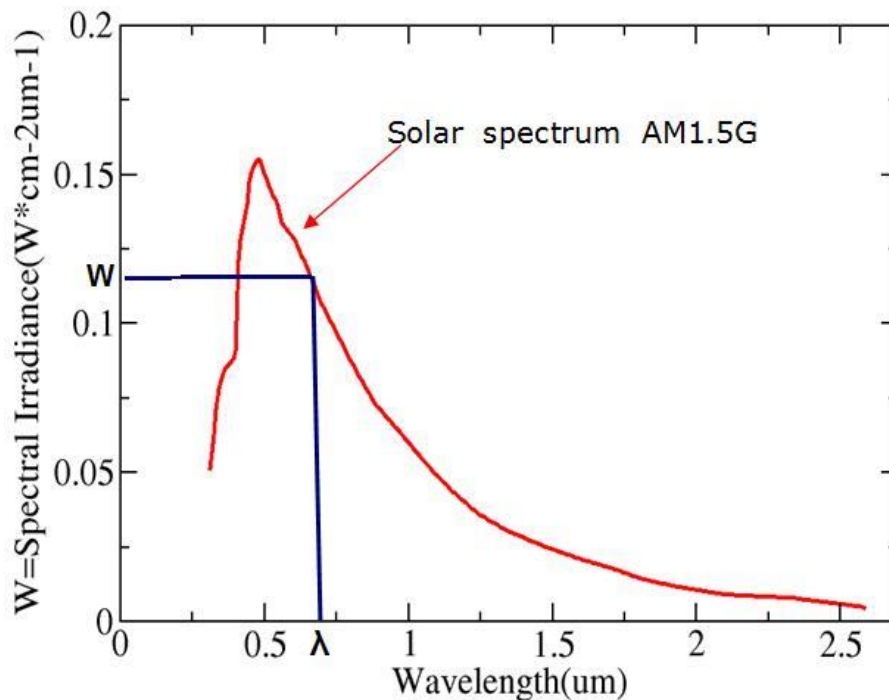


Figure 4.1. Solar spectral spectrum(Where AM is Air Mass) . The figure obviously shows different wavelengths light corresponding to variable intensity due to the different degree of absorption and scattering in the atmosphere.

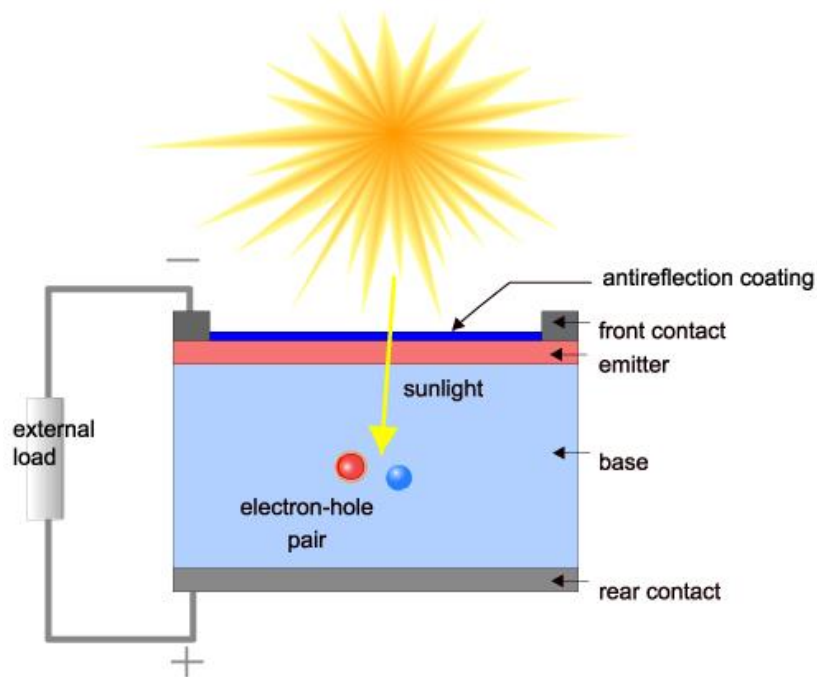


Figure 4.2. Simple solar cell structure.<sup>132</sup> Sunlight is absorbed and electron-hole pairs are created meanwhile. The electrons work on external load, after their energy is dissipated, they return into solar cell.

At the same time, the fossil sources are not renewable, and we can imagine that finally they will be used out in one day. However, the sunlight is regarded as renewable energy source. Additionally, solar energy is inexhaustible energy resource. That is why the study and application of solar cells attract more and more researchers to study in this field.

Attention on search for high efficiency and low cost solar cells has never decreased since the first solar cell development in 1950s.<sup>65, 133, 134</sup> Through researchers effort, to now, as certificated by National Renewable Energy Laboratory (NREL) in Figure 4.3, four-junction GaAs research-cells based concentrators possesses the best efficiency up to 46%.<sup>135</sup> Even this kind of solar cell has high efficiency, it is not suitable to mass commercial production due to its expensive cost compared with traditional crystalline silicon(c-Si) based solar cells whose efficiency can reach 27.6%.<sup>135</sup> Especially, the existence and development of III-V multi-junction solar cells, perovskite solar cells and copper indium gallium selenide (CIGS) solar cells, application of this high efficiency is pendulous. Advanced processes in III-V alloys monolithic epitaxial growth on silicon substrate<sup>136,137</sup> make these alloys promising materials for low cost multi-junction solar

cells.<sup>138-140</sup> The first tandem solar cell for this kind of structure was reported by J. F. Geisz et al with 5.2% efficiency under AM1.5G.<sup>141</sup> This kind of solar cell will be explained more in section 4.3. Perovskite solar cells efficiencies have increased from 3.8%<sup>142</sup> to 23.7%<sup>135</sup> in past years, at the same time, 28% efficiency has been reached in silicon-based tandem cells.<sup>143</sup> Probably, new record shall appear as it goes on rocket-like rise. Moreover, in the case of metal halide perovskites solar cell, the materials and the fabrication methods (such as various printing techniques) are low cost.<sup>144</sup> Research on CIGS thin film solar cell also achieved new results. Its efficiency has reached as high as 22.9%<sup>145</sup> from 4.5%<sup>146</sup>. The prominent performance of CIGS is that it owns high absorption coefficient and bandgap range by controlling the Ga/In ratio.<sup>147</sup> Besides, CIGS solar cell has an exception of low cost compared with conventional c-Si solar cell technology.<sup>148</sup>

# Best Research-Cell Efficiencies

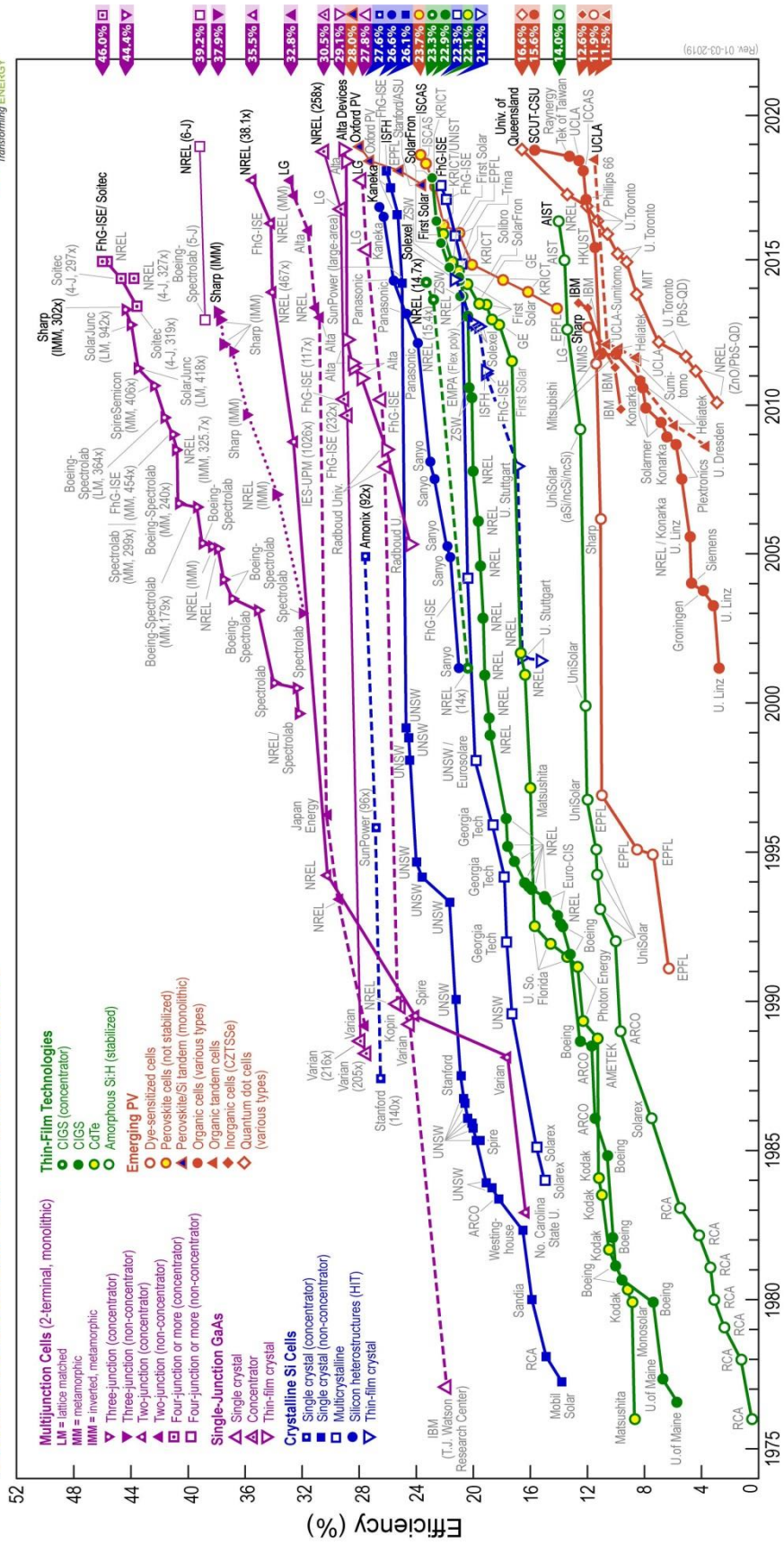


Figure 4.3. Best Research-cell efficiencies certified by NREL(01-03-2019)

## 4.2 Solar cell principle

Basically a solar cell is a p-n junction under illumination (Figure 4.4). It is formed by different types of doped materials. In p type material, IV semiconductor material is doped with III material, holes have dominant proportion, but electrons own few proportion. On the contrary, in n type material, IV semiconductor material is doped with V material, electrons take a big account, and holes possess a small account. Once these two varied semiconductor materials contact each other, near the interface, due to their different carriers' densities, electrons diffuse from n material into p material, leaving holes. In the similar way, holes diffuse from p material into n material, leaving electrons. This diffusion also induces the build-in electric field appearance which makes the holes drift along electric field direction and electrons drift in the opposite direction. At last, the number of diffusion carriers equilibrates with of which drove by electric field effect. This case is named the thermal equilibrium state of p-n junction.

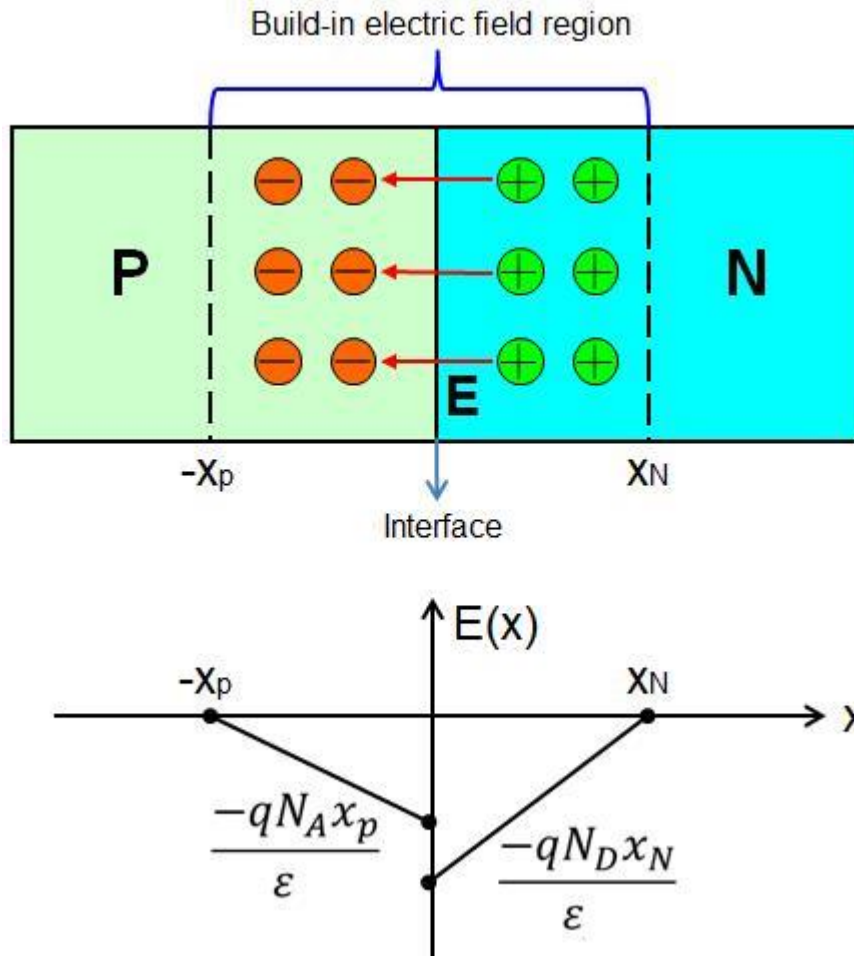


Figure 4.4. p-n junction at thermal equilibrium state and corresponding electric field. The left and right are p and n type materials. The built-in electric field is formed by immovable electrons (Orange circles) and holes (Green circles). Where  $q$  is the magnitude of unit charge,  $N_A$  ,  $N_D$  are the net acceptor concentration in the p side and the net donor concentration on the N side,  $\epsilon$  is the permittivity.

As we all know, the sunlight contains a host of different lights, each of them has corresponding wavelength and photons energy see Figure 4.1. For conventional semiconductor materials, when the energy of photons is less than semiconductors energy bandgap ( $E_g$ ), the energy is lost by transparency. On the contrary, the energy of photons above the bandgap energy is absorbed and that leads to generation of electron-hole pairs, but due to the carriers thermalization (depending to the photon energy), those carriers with high energy prone to back the lower energy state in conduction band ( $E_c$ ). In this process, the energy is lost by cristal heating. That induces increase of device temperature. Under incident light absorption, electron-hole pairs are created, so p-n junction thermal equilibrium state is broken. Due to the existence of

build-in electric field, electron-hole pairs are separated by it and collected by different electrodes. This process is the basic solar cell theory.

A solar cell device can be modeled as a circuit containing a diode and two resistances, simplified as Figure 4.5. The major device parameters are: the open Circuit Voltage ( $V_{oc}$ ), the short Circuit Current ( $I_{sc}$ ), the Series Resistance ( $R_s$ ) and Shunt resistance ( $R_{sh}$ ), the Fill factor (FF), and the conversion Efficiency ( $E_{ff}$ ). All of them are going to be explained by following text.

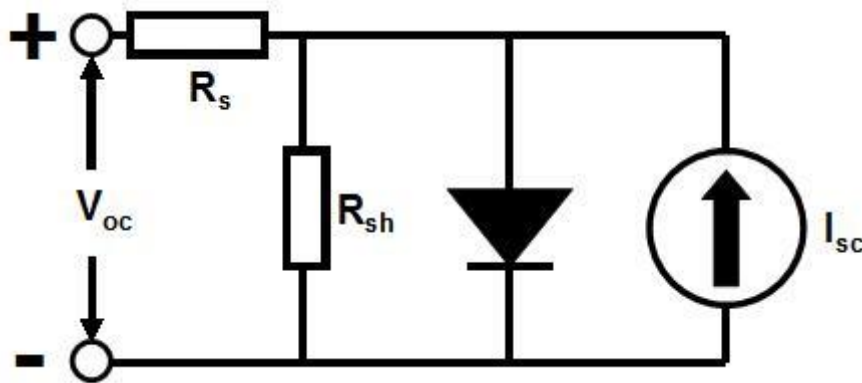


Figure 4.5. Solar cell equivalent circuit diagram.

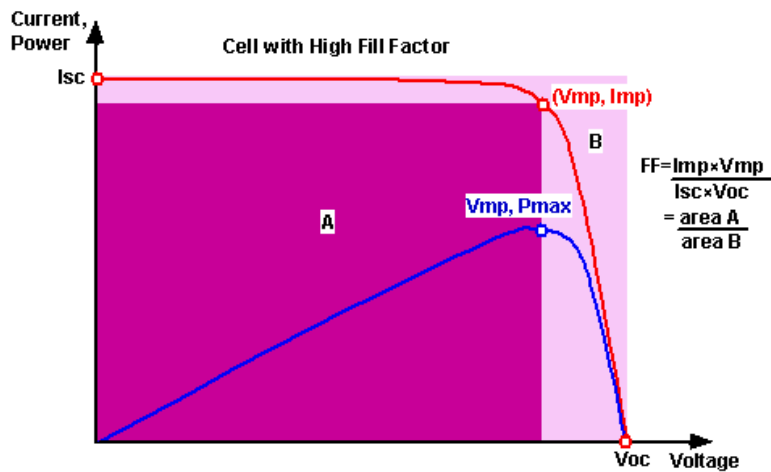


Figure 4.6. Solar cell I-V curve under illumination.<sup>132</sup> Output power (blue line) and current (red line) as a function of voltage.

Open Circuit Voltage: The device voltage, as the device current is zero. It can be calculated by this equation<sup>132</sup>

$$V_{oc} = \frac{nkT}{q} \ln\left(\frac{I_L}{I_0} + 1\right) \quad 4-1$$

Where  $q$  is elemental charge,  $n$  is the diode ideality factor,  $k$  is the Boltzmann constant, and  $T$  is the temperature,  $I_L$  is light-generated current,  $I_0$  is the dark saturation current.

Short Circuit Current: The device current, as the device voltage equals zero. It can be expressed as <sup>132</sup>

$$I_{SC} = qG(L_n + L_p) \quad 4-2$$

Where  $G$  is carriers generation rate,  $L_n$  is electron diffusion length and  $L_p$  is hole diffusion length. Diffusion length is defined as the carriers average traveling distance before they are recombined and it can be expressed by equation:

$$L = \sqrt{D\tau} \quad 4-3$$

Where  $D$  is the diffusion coefficient,  $\tau$  is the carriers lifetime

Series Resistance: It is composed by three parts: First, the movement of current through the device emitter and base. Second, the contact resistance which could be generated by metal and silicon contact, and the last is the electrode resistance. This type of resistance also decreases fill factor, meanwhile if its value is too high, it leads to a reduction of the short circuit current.

Fill factor: The device maximum output power  $I_{mp} \cdot V_{mp}$  divided by the produce of  $V_{oc}$  and  $I_{sc}$ . See Figure 4.6, it can be described as

$$FF = \frac{V_{MP} I_{MP}}{V_{OC} I_{SC}} \quad 4-4$$

Where  $V_{MP}$  is voltage at max power,  $I_{MP}$  is current at max power. Obviously, the higher is the FF, the better are the device performances.

Shunt resistance: It could be generated by manufacturing defects at the interfaces. For a low value, it causes the light generated current can't go through p-n junction totally, but offers an alternate current path. That makes power lost. Shunt resistance also can reduce fill factor.

Conversion Efficiency: The max output power divide by the incident light energy. Expressed as

$$\eta = \frac{P_{MP}}{P_{IN}} = \frac{V_{oc}I_{sc}FF}{P_{IN}} \quad 4-5$$

Where  $P_{MP}$  is max output power,  $P_{IN}$  is incident light power.

For the single junction based on c-Si solar cell, many different ways are applied to improve device performance. Of course, a bunch of results have been gained. Up to now, Si single junction solar cell efficiency is about 27.6%<sup>135</sup> (with light concentrators) in lab and 24.4%<sup>149</sup> for industrial production. But in recent latest years, the efficiency just makes a little progress and it closes to theoretical limit. As the well-known Shockley-Queisser limit proposed in 1961 describes.<sup>150</sup> This method assumes all the photons above material bandgap can be absorbed and the generated carriers can be collected completely. It is obvious that as displayed in Figure 4.7, the  $I_{sc}$  decreases with the increase of absorbing material bandgap, due to the light transparency. In other words, when the absorbing material bandgap becomes bigger, there are more photons whose energy is lower than bandgap going through material. Thus they don't make contribution to electron-hole pairs generation. But  $V_{oc}$  increases, owing to lower absorbed carriers thermalization causing by the higher split of the Fermi level, when the absorbing material bandgap increases.<sup>150</sup> So this trade-off makes there exists an optimum photovoltaic devices efficiency, as shown in Figure 4.8.

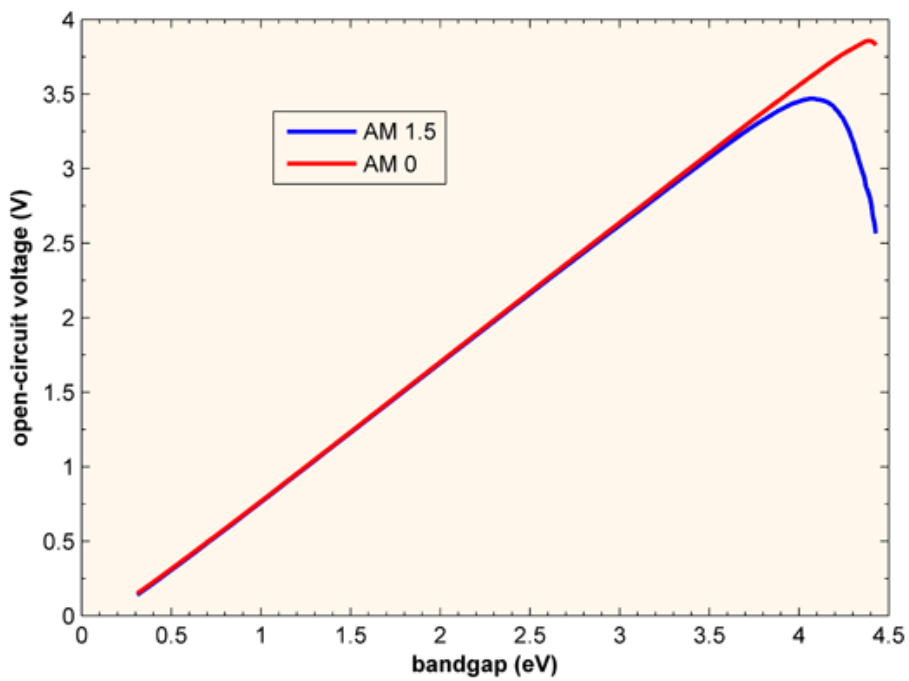
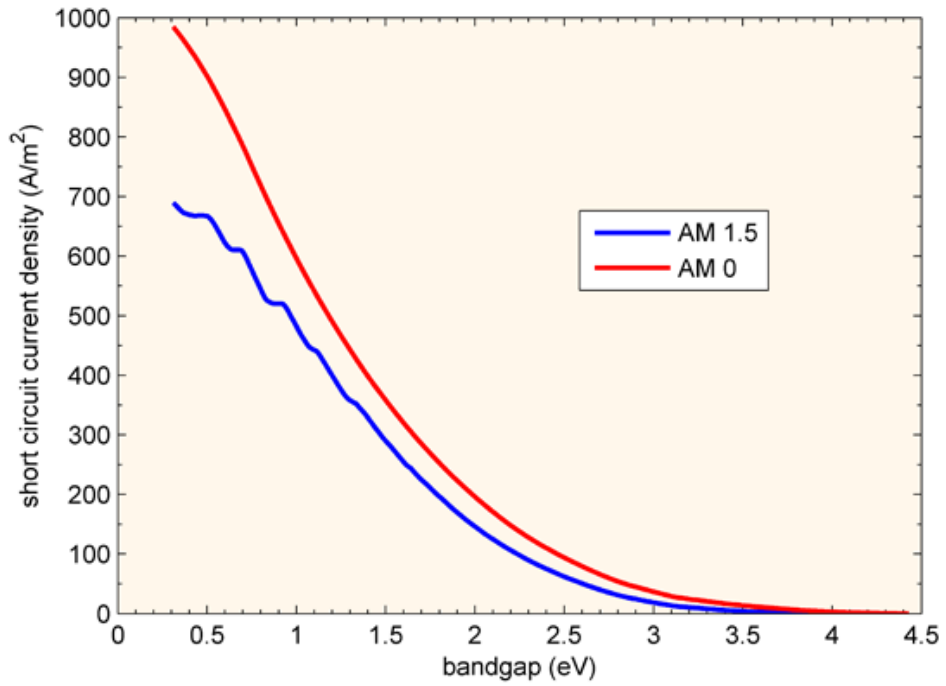


Figure 4.7. Ideal short circuit current density (above) and open circuit voltage (below) for different bandgap materials under different solar spectrum.<sup>132</sup>

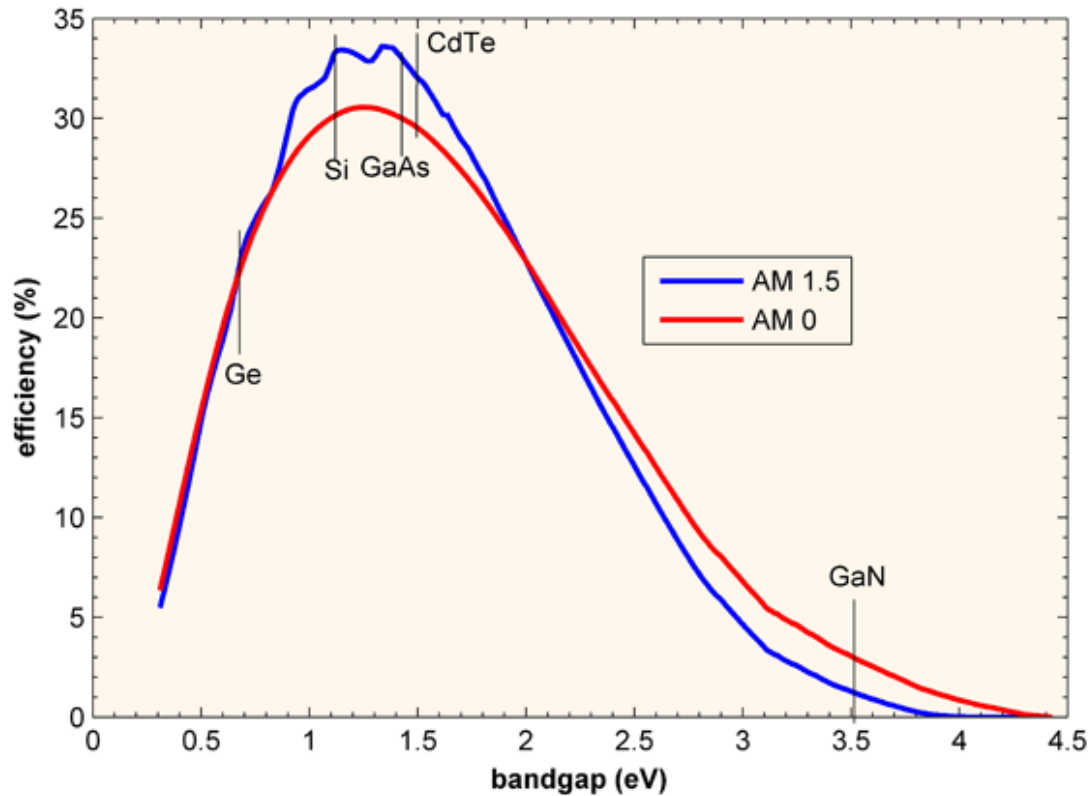


Figure 4.8. PV device efficiency limit as a function of material bandgap calculated by Shockley-Queisser method.<sup>132</sup>

In order to improve the efficiency, a lot of methods are proposed. Different solar cell structures: In order to eliminate the shadow losses and restrictions on metal-contact/busbar size which are induced by front contact grids, back-contact solar cell structure was proposed. In this structure, the positive and negative contacts are located on the device backside, so it can solve the problem well.<sup>151</sup> Heterojunction with intrinsic thin layer (HIT)<sup>152</sup> solar cell with 26.6% efficiency based on Si substrate has been reached as well.<sup>135</sup> This symmetrical structure solar cell has many advantages: High open circuit voltage, excellent passivation effect and low process temperatures.<sup>153</sup> And the new passivation material- $\text{Al}_2\text{O}_3$  is studied and some results have gained by B.Hoex and his colleagues.<sup>154, 155</sup> However, due to the Shockley-Queisser limit, it is hard to make single junction to reach a very high efficiency record, for further steps, in the light of the limitations and gaining much higher solar cell efficiency, new concepts should be proposed.

## 4.3 Tandem solar cell structure

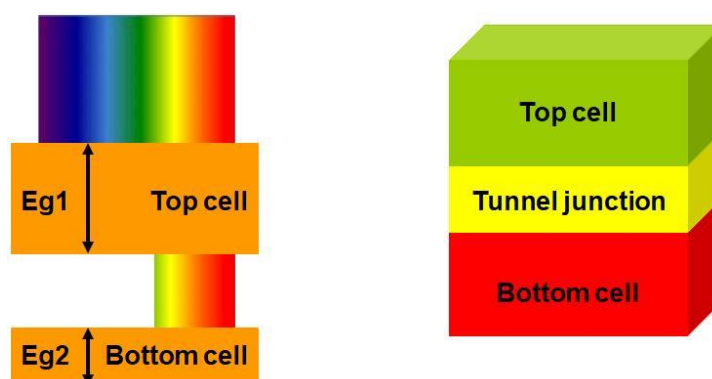


Figure 4.9 Schematic of tandem solar cell band diagram and structure

Based on previous theories, in order to decrease the thermodynamic loss and make full use of sunlight, a big number of concepts have been proposed. Among all of them, multijunction solar cells take a dominant advantage. An approach of stacking two junctions is called tandem system.<sup>156-158</sup> Tandem solar cell splits the spectrum into two parts. Each of parts has an according absorbing material for absorbing different energy range of the input light. Figure 4.9 presents the tandem solar cell schematic of band diagram and structure. From it, we can also see that tandem solar cell is composed by three parts: Top cell, bottom cell and tunnel junction. The top cell, with high bandgap absorber, is used for the absorption of the photons with high energy. The middle member, tunnel junction, is used to electrically connect the two sub-cells. The last part is the second sub-cell with low bandgap absorber, which is used for the absorption of the rest of light incoming from the former top sub-cell.

For our tandem solar cell structure,  $\text{GaAs}_{0.09}\text{P}_{0.87}\text{N}_{0.04}$  (GaAsPN) grown by Molecular Beam Epitaxy (MBE) based on GaP(001) in FOTON lab and Si are applied to top cell and bottom cell absorbing materials. It is based on the following reasons:

- ◆ First, the whole device current is determined by the smallest sub-cell current, so it is important to match the sub cells to each other. For the structure, GaAsPN (bandgap1.75eV) junction with Si (bandgap1.12eV) junction, the sub-cells

must have **perfect current matching** and **high theoretical efficiency**. Figure 4.10 shows the tandem solar cells efficiency of different materials bandgaps combination depending on the solar spectrum. And also Si as bottom cell, GaAsPN as top cell, this structure device not only has good current matching but also supposed to have efficiency as high as 37% theoretically.

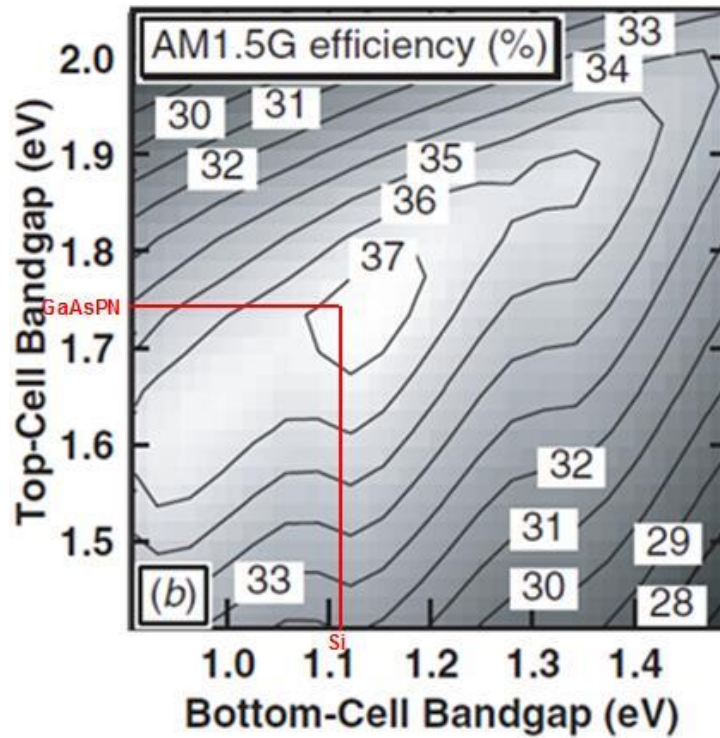


Figure 4.10. Tandem solar cell theoretical efficiency as a function of top-cell and bottom-cell bandgaps<sup>141</sup> using standard AM1.5 global spectrum. The red lines cross is the GaAsPN/Si tandem solar cell efficiency. From the figure, this tandem solar cell efficiency value drops into the highest circle-37%.

◆ Second, Figure 4.11 shows GaAsPN can have good lattice matching with Si depending on the material composition. That reduces the defects: Threading dislocation density, microtwins, stacking faults and anti-phase domains<sup>159-165</sup> which are induced by lattice mismatch and drastically decrease the solar cells performances. The study at NREL shows that the device current decreases definitely even the lattice mismatch as small as 0.01%.<sup>166</sup>



charge,  $\vec{J}_n$  ,  $\vec{J}_p$  are electron and hole current densities,  $G_n$  ,  $G_p$  are electron and hole generation rates,  $R_n$  ,  $R_p$  are electron and hole recombination rates,  $\Psi$  is electrostatic potential,  $\rho$  is local space charge density,  $\epsilon$  is local permittivity

Drift diffusion currents:

$$\vec{J}_n = -qn\mu_n\vec{\nabla}\phi_n \quad 4-9$$

$$\vec{J}_p = -qp\mu_p\vec{\nabla}\phi_p \quad 4-10$$

Where  $n$  ,  $p$  are electrons and holes concentration  $\mu_n$  ,  $\mu_p$  are electron and hole mobilities,  $\phi_n$  ,  $\phi_p$  are electron and hole quasi-Fermi levels.

Recombination: electrons stabilize from conduction band (CB) back to the valence band (VB), then recombine with holes, accompanying energy loss. In silicon-based solar cells, there are four main recombination types: Radiative, Surface, Shockley-Read-Hall, and Auger.

Radiative recombination (Figure 4.12): electrons jump from conduction band to valence band, recombining with holes. During this process, the energy is released as photons. This recombination mechanism is dominant in direct bandgap semiconductors, but in Si based solar cell, this recombination takes very low proportion, so it is always neglected. But GaAsPN is pseudo-direct bandgap, this type of recombination should be took into account.

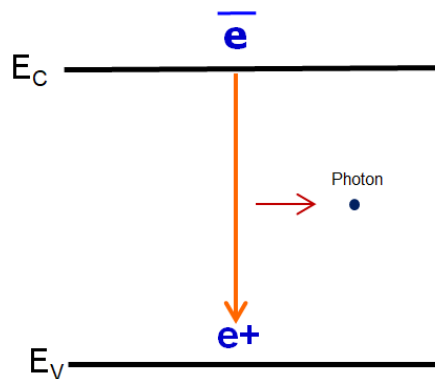


Figure 4.12. Schematic radiative recombination.

The net recombination rate can be expressed as

$$R = \alpha_{rad} \cdot (n \cdot p - n_i^2) \quad 4-11$$

Where  $\alpha_{rad}$  is radiative coefficient,  $n$  ,  $p$  are electron concentration and hole

concentration,  $n_i$  is intrinsic carrier concentration.

Surface recombination: The surface defects or dangling bonds-traps-are induced by substrate related processes. These bonds can break the symmetry of lattice, so there exists a large defects density at the substrate surface (and at the different interfaces), hence that makes very high recombination effect.

Shockley-Read-Hall(SRH) recombination (Figure 4.13): In this recombination, the deep trap states induced by impurities appear in bandgap. As the introduction of deep trap, compared with radiative recombination, first the electrons jump from conduction band to deep trap level, the energy is released as photons or multiple phonons, then to valence band, recombining with holes. The energy is released as other photons or multiple phonons.

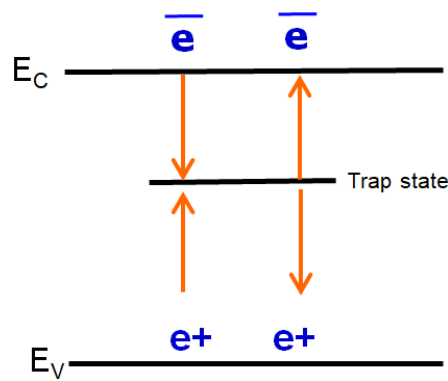


Figure 4.13. Schematic SRH recombination.

the SRH recombination rate is given by:

$$R_{SRH} = \frac{pn - n_{ie}^2}{\tau_{n0}(n + n_{ie}) + \tau_{p0}(p + n_{ie})} \quad 4-12$$

where  $\tau_{n0}$ ,  $\tau_{p0}$  are the electron and hole lifetimes,  $p$ ,  $n$  are the hole and electron concentrations,  $n_{ie}$  is the intrinsic electron concentration.

Auger recombination: In this recombination, after the electrons recombine with holes, the energy is transferred to another electron in conduction band. Then this electron gives off the energy by heat and back to low energy state in conduction band.

$$R_{Auger} = G(pn^2 + np^2) \quad 4-13$$

The software through numerically solving these set of equations, the device priorities can be got under steady state or transient conditions.

With this tool, 1D or 2D numerical simulations can be done.

The structure input parameters are :Layers thickness/Doping levels/Types, and material input parameters :Bandgap/Carriers mobilities/Affinities/Lifetimes/n.k (where n is refractive index, k is extinction coefficient). Then the software solves the three preceding set of equations, and many parameters can be outputted, such as I-V(dark and under illumination)/Quantum efficiency/Conduction band/Valence band/Carrier concentrations/Traps/. As an example Figure 4.14 shows one input material parameter sample based on experimental GaAsPN n-k data.

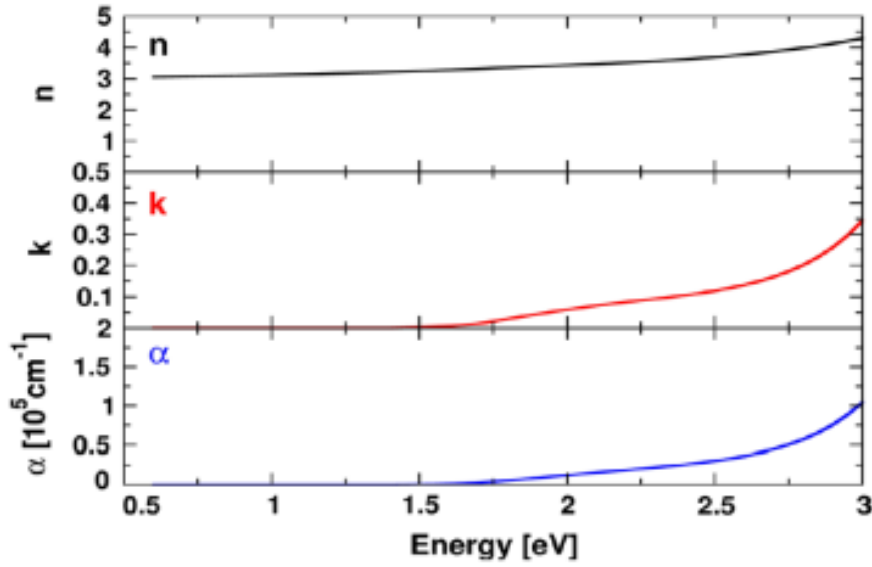


Figure 4.14. Experimental GaAsPN n,k data.  $\alpha$  is absorption coefficient.

SILVACO is probably the only tool able to simulate tandem solar cells based on tunnel junction. For simulating tunnel effect, "Non-local Band-to-Band Tunneling" modes are used.

$$J_t = \frac{qk_B T_L}{2\pi^2 \hbar^3} \sqrt{m_e m_h} \int T(E) \ln \left\{ \frac{1 + \exp[(E_{f,r} - E)/k_B T_L]}{1 + \exp[(E_{f,l} - E)/k_B T_L]} \right\} dE \quad 4-14$$

where  $T_L$  is the lattice temperature,  $k_B$  is the boltzmann constant,  $J_t$  is the tunneling current,  $\hbar$  is Planck constant, and  $m_e$  ,  $m_h$  are the electron hole effective masses. The current in the(E, E+dE) range is integrated by the tunnel probability T(E), which is given by the Wentzel-Kramers-Brillouin (WKB) approximation.  $E_{f,r}$  and  $E_{f,l}$  are the quasi-Fermi levels on either side of a tunnel junction.

In these models, calculation of each point recombination-generation rate uses field

value local to the point itself. That is why they are so called local models. In order to process more accurately, what should be taken into account are that the spatial variation of energy bands and that different carrier type generation/recombination are not spatially coincident.

Also, for every simulation, the mesh is defined through the whole structure. The mesh comprises a heap of vertical and horizontal lines according to define X, Y directions mesh, also between the lines, spacing exists. Meantime, the coarse mesh makes fast simulation. By contrast, the fine mesh is more time consuming. By the way, for defining the mesh, the statements are variable. There are many kinds of mesh type for defining structure. Just like periodic and discontinued mesh. Figure 4.15 is an example from SILVACO user's manual, in this structure, different parts are defined by different types of mesh.

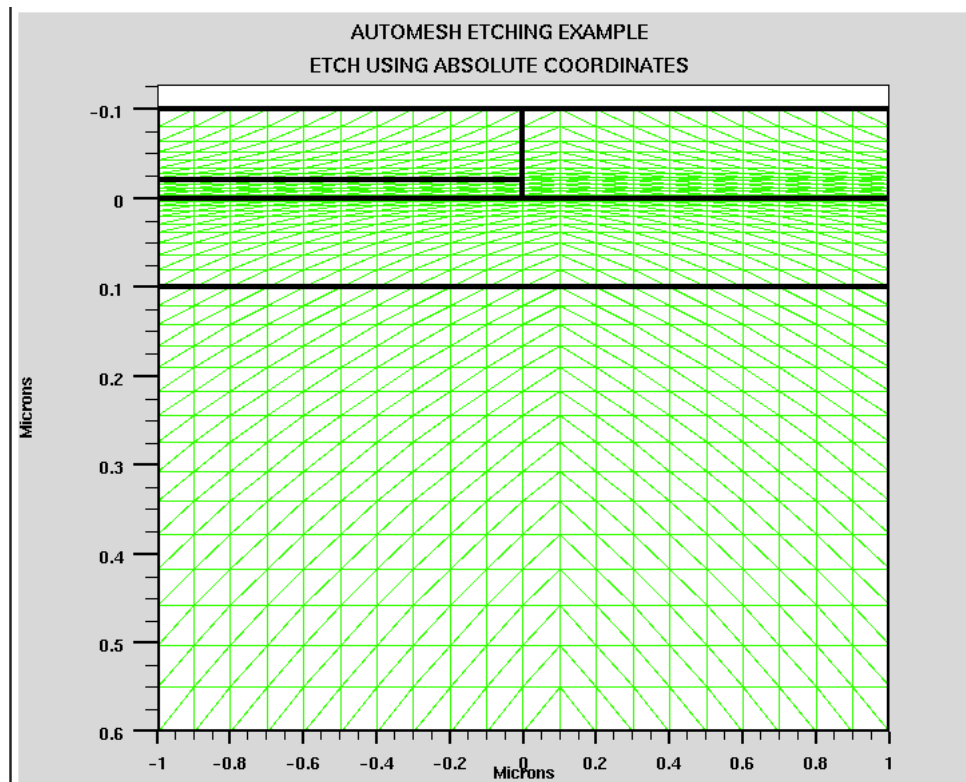


Figure 4.15. A sample of structure mesh in SILVACO (Different parts are defined with corresponding mesh by command language).<sup>167</sup>

## 4.5 Influence of GaAsPN absorbing layer thickness

Materials bandgaps are very important features for solar cells devices. After materials are selected, their thicknesses play an important role in light absorption and carriers transport as well. The light is absorbed, and the carriers are created. As described by Beer-Lambert law:

$$I_{(x)}=I_{in} e^{-\alpha x} \quad 4-15$$

Where  $I_{in}$  is top surface incident light intensity,  $\alpha$  is the absorption coefficient, it has a relationship with extinction coefficient ( $k$ ) and wavelength ( $\lambda$ ) as

$$\alpha =4\pi k/\lambda \quad 4-16$$

, like shown in Figure 4.14,  $x$  is the depth into material. From this equation, it is shown that light intensity exponentially decays with the depth away from the interface. When the light intensity values  $\frac{I_{in}}{e}$ , the depth into material ( $x$ ) is named absorbing depth: the inverse of the absorption coefficient.

In order to correctly convert the incident light into photocurrent, the thicker material thickness is, the better result will be got. Meanwhile the increase of thickness also leads to an increase of device parasitic series resistance. But for transporting the carriers out before they were recombined, the minority carrier diffusion length must be greater than absorbing depth. Above all, all these parameters should be balanced for getting good device performance.

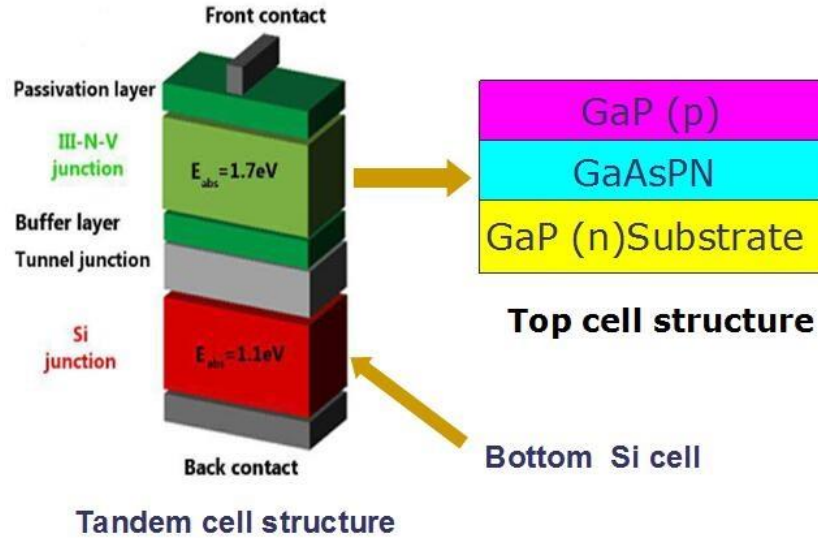


Figure 4.16. Schematic of tandem solar cell and top junction.

Our top cell consists of three layers (shown in Figure 4.16). The GaAsPN layer is used as active layer for absorbing light and creating electron-hole pairs and the two different doping types GaP layers form p-n junction, as a function of separating and collecting electron-hole pairs created by active layer.<sup>158</sup>

In our simulation, the structure parameters are shown in Table 4-1. In fact, because of the lack of GaAsPN material parameters from experiments, due to the different experiments' environment, the technologies and the substrates' quality, the GaAsPN material properties are not similar to each other, meanwhile the stability of GaAsPN is poor.<sup>168</sup> So according to that, the material data we used are based on GaInAsN material in earlier publications.<sup>141, 169, 170</sup>

Table 4-1: Top junction materials parameters

	Thickness( $\mu\text{m}$ )	Doping( $\text{cm}^{-3}$ )	Lifetime(s)	Mobility( $\text{cm}^2\text{V}^{-1}\text{s}^{-1}$ )	Bandgap(eV)
GaP	0.03	$N_A=10^{18}$	$\tau_n=\tau_p=1e-7$	$\mu_n=150, \mu_p=40$	2.26
GaAsPN	Variation	intrinsic	$\tau_n=\tau_p=1e-9$	$\mu_n=100, \mu_p=80$	1.75
GaP	400	$N_D=10^{18}$	$\tau_n=\tau_p=1e-7$	$\mu_n=150, \mu_p=40$	2.26

Figure 4.17 shows the simulated I-V curves for different GaAsPN thickness of top cell. The AM1.5G, wavelength range 305nm~1000nm, is used as incident light source. With the increase of GaAsPN thickness from 0.5 $\mu\text{m}$  to 2.0 $\mu\text{m}$ , the device's  $I_{sc}$  increases,

due to more absorbed light, which results in more electron-hole pairs created and collected. For thicknesses above  $1.5\mu\text{m}$ , the open circuit voltage keeps a constant value, but the fill factor decreases. Owing to the resistance effect induced by the increase of GaAsPN thickness. The optimum active layer thickness range is about  $1\sim 1.5\mu\text{m}$  which corresponds to:  $\text{Eff}\approx 10.7\%$ ;  $\text{Voc}\approx 1\text{ V}$ ;  $\text{Jsc}\approx 20\text{ mA/cm}^2$ .

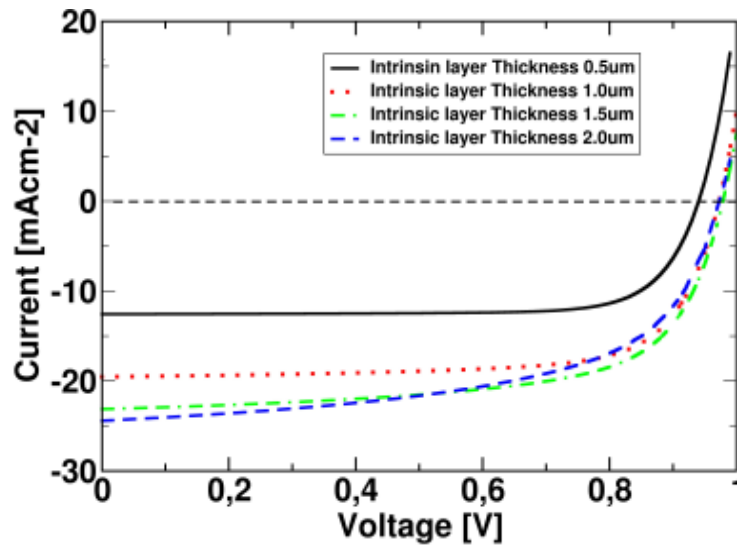


Figure 4.17. Current-voltage characteristics: simulation results for different GaAsPN thicknesses.

## 4.6 Influence of band offset

From former simulation results, even if the GaAsPN thickness is optimized, the top cell performance is not great. The low current value is the main factor of failing to theoretical efficiency<sup>17</sup>. It is well known that electrons flow in conduction band from p doping region to n doping region, while holes transport in valence band in reverse direction. For heterojunction, band offset appear at the interfaces formed by GaAsPN and GaPs layers. In the case of our structure, a band offsets exist at GaAsPN and GaPs interfaces. As described in former publication, the existence of band offset in heterojunction has a bad effect on device performance.<sup>171</sup>

In order to find the reasons depressing the efficiency and the ways to solve the problems, for conducting lab experiments, it is necessary to analyze top cell from energy band point of view. Figure 4.18 shows schematics of the top junction energy

band. <sup>172</sup> C.Robert used tight-binding model<sup>173, 174</sup> to calculate GaAsPN valence band and conduction band in his thesis. In his simulation, valence band of bulk GaP is used as energy reference. For the GaAsPN material we used, as the As and N contents are both too low, so the simulation result, it can be deduced that the energy barriers at the interfaces between GaPs and GaAsPN in valence band are small enough so that they can be ignored. That means no valence band offsets exists between GaPs and GaAsPN layers. But the barrier in conduction band is as high as 0.45eV at the interface formed by GaAsPN and n type GaP with bandgaps 1.75eV and 2.2eV respectively. Because the electrons flow from p type to n type GaP materials, so this high barrier is expected to decrease the electron transport in conduction band.

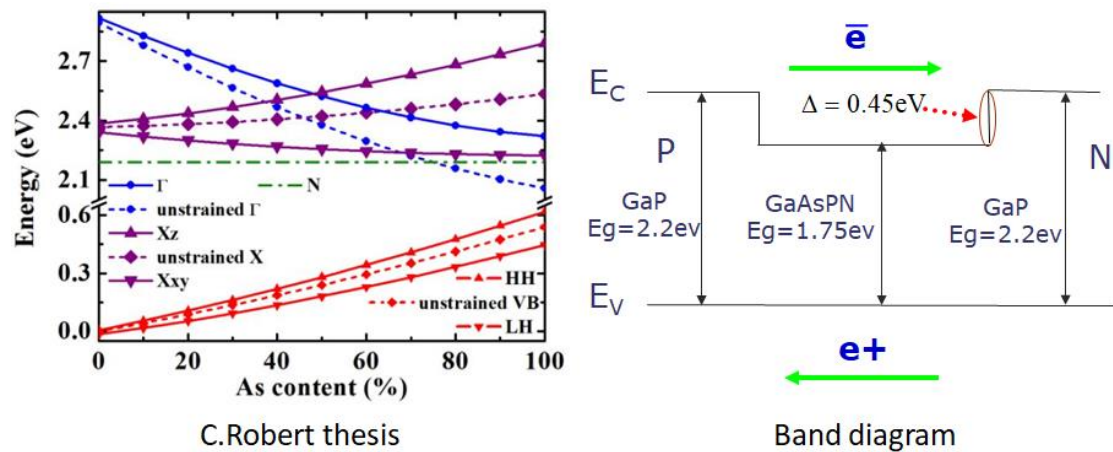


Figure 4.18. C.Robert simulation results and top junction band diagram(Left figure: GaAsPN conduction and valence bands with very low N content as a function of As content. <sup>172</sup> Right figure: our top junction band diagram).

For the sake of augmenting the current and reducing the barrier effect, inserting graded layers with different bandgaps in heterojunction is a good way to meet the goals. <sup>175</sup> Graded layers divide the band offset into small steps. That makes more carriers can flow over the barriers and be collected. As illustrated in Figure 4.19, in our simulation, two various styles of graded layer are placed between active layer GaAsPN and bottom GaP layer (described in following text). For these two kind of graded layers, their valence bands are at the same level, just have different bandgaps.

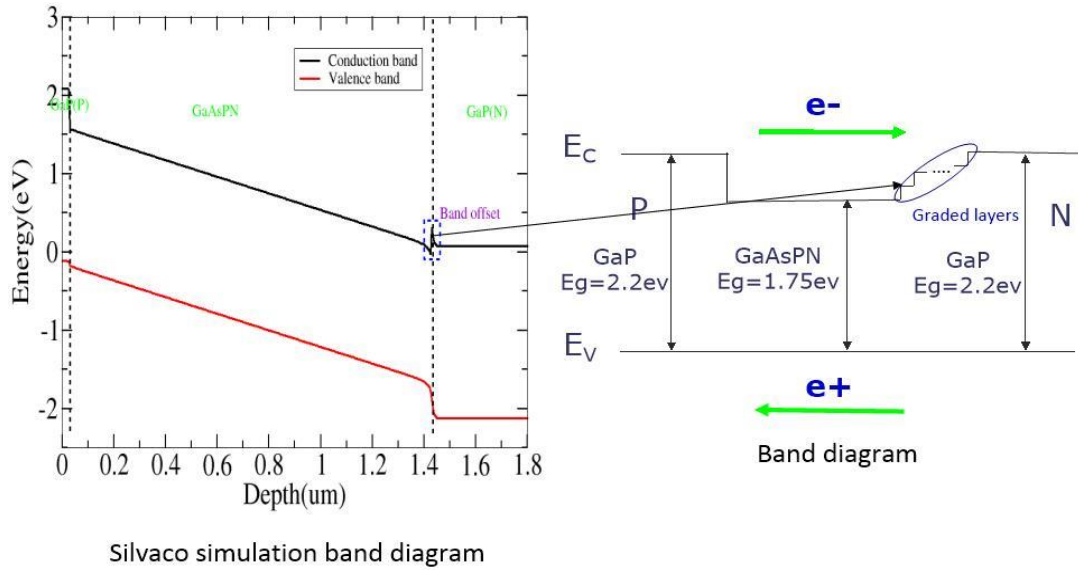


Figure 4.19. Band diagrams from Silvaco simulation and theory.

For the first type of graded layers, each layer has a 0.1eV bandgap interval, that means all graded layers have the same valence band level, but the bandgaps increase from 1.75eV to 2.15eV in 0.1eV step. And each of them with a 0.02 $\mu\text{m}$  thickness; In the same convention, for the other type of graded layers, each layer has a 0.025eV difference between each bandgap. This energy spacing derives from thermal limit  $k_0T \approx 0.026\text{eV}$  (where  $k_0$  is boltzmann constant, T is room temperature), so for this case, the bandgaps increase from 1.75eV to 2.175eV in 0.025eV step, and each of them with the same thickness value 0.02 $\mu\text{m}$ ; From simulation, above two graded layers are easy to realize, but for experiment, due to doping process, especially for the latter case, it is hard to apply, but at least, that can help us to analyze the results and for further understanding about the principle.

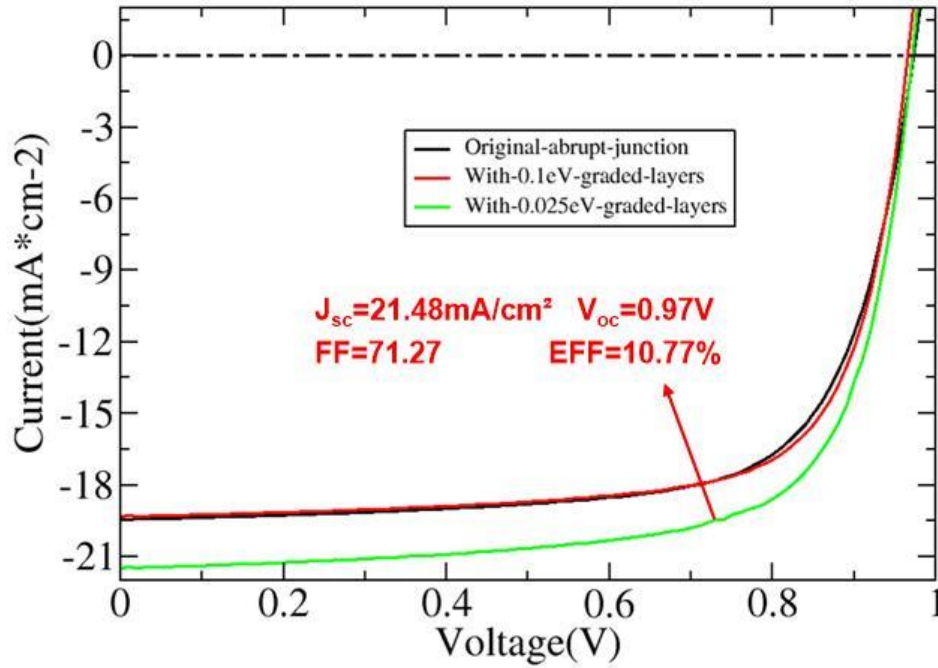


Figure 4.20. With and without graded layers simulation results.

Figure 4.20 shows the results of the two junctions with graded layers and the original abrupt junction. From the picture, it is observed that the performances of junctions with graded layers are superior to performances of the original abrupt junction. Meanwhile, for these junctions with graded layers, the smaller band steps are, the better performances the device has. The efficiency, open circuit voltage and other main according parameters of the better device are depicted in the figure as well. All of these manifest that the energy barrier between heterojunction stands on the way of electron transport.

Above all, for our structure, we can get a conclusion that the band offset existing at the interface formed by the active layer GaAsPN and bottom GaP absolutely hampers the electrons transport, meantime, more suitable graded layers with lower energy steps should be a sensible way to decrease the bad effect and promote the device performance. Just like find appropriate materials, their bandgaps are higher than GaAsPN bandgap but lower than GaP bandgap. Of course, their corresponding lattice constants should be taken into account.

## 4.7 Study of top cell EQE

External Quantum Efficiency (EQE) is one of the relevant parameters to evaluate solar cell device performance. It is defined as the proportion of number of collected charge carriers over number of incident photons,

$$EQE(\lambda) = \frac{\text{Collected charge carriers number}}{\text{Incident photon number}} \quad 4-17$$

EQE indexes the ratio of the collected carriers number. Figure 4.21 presents the theoretical solar cell quantum efficiency. The existence of deep traps and defects which cause carriers recombination makes the realistic quantum efficiency lower than ideal quantum efficiency.

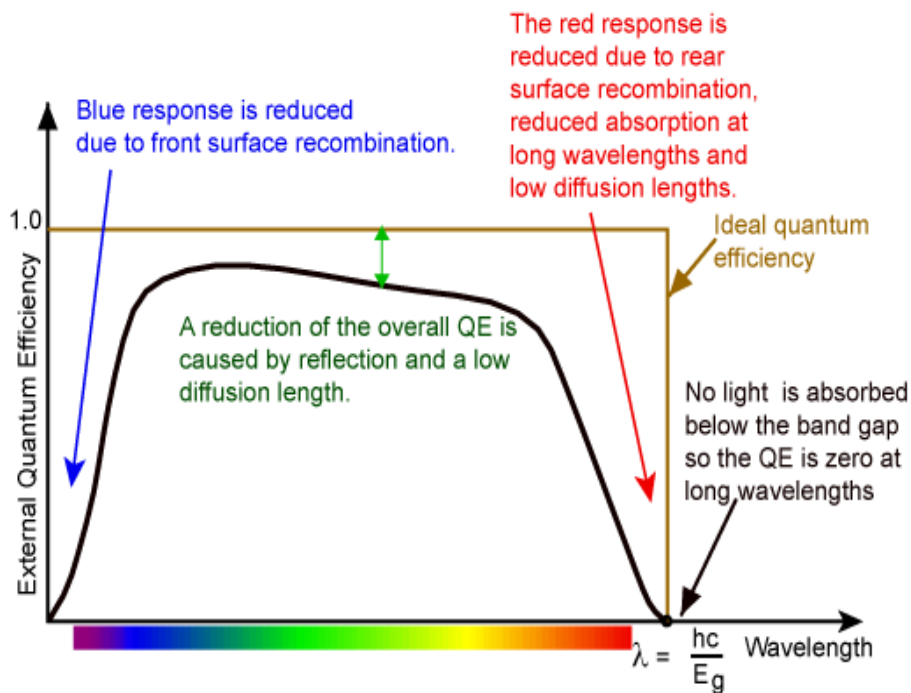


Figure 4.21. Theoretical quantum efficiency of solar cell device<sup>1</sup>.

In our simulations, the wavelength range 305nm~1000nm is used as solar spectrum. The band offset is not only affecting the device current, described as previous, but also acts on EQE result.<sup>176</sup> Just as the way of analyzing carriers transport, we simulate and analyze the top junction EQE from energy band viewpoint. In order to

further understand the function of band offset on EQE, we assume three cases of GaAsPN with different affinities: the corresponding materials' parameters are shown in Table 4-2. Active layer GaAsPN bandgap keeps constant for these simulations, that ensures the light and absorption and created carriers are the same, just change its affinity with values of 3.8eV, 4.0eV and 4.3eV respectively.

Table 4-2: Materials parameters for different active layer affinities EQE simulations.

	Thickness ( $\mu\text{m}$ )	Doping ( $\text{cm}^{-3}$ )	Lifetime (s)	Mobility ( $\text{cm}^2\text{V}^{-1}\text{s}^{-1}$ )	Bandgap (eV)	Affinity (eV)
GaP	0.03	$N_A=10^{18}$	$\tau_n=\tau_p=1e-7$	$\mu_n=150, \mu_p=40$	2.26	3.8
GaAsPN	1.4	Intrinsic	$\tau_n=\tau_p=1e-9$	$\mu_n=100, \mu_p=80$	1.75	3.8,4.0,4.3
GaP	200	$N_D=10^{18}$	$\tau_n=\tau_p=1e-7$	$\mu_n=150, \mu_p=40$	2.26	3.8

Of course, as the affinity is changed, the corresponding band offsets in conduction band and valence band are different. Figure 4.22 shows that there are two interesting cases when the affinity equals to 3.8eV and 4.3eV, in this case, there is no barrier in conduction band and valence band separately, as shown in Figure 4.22.

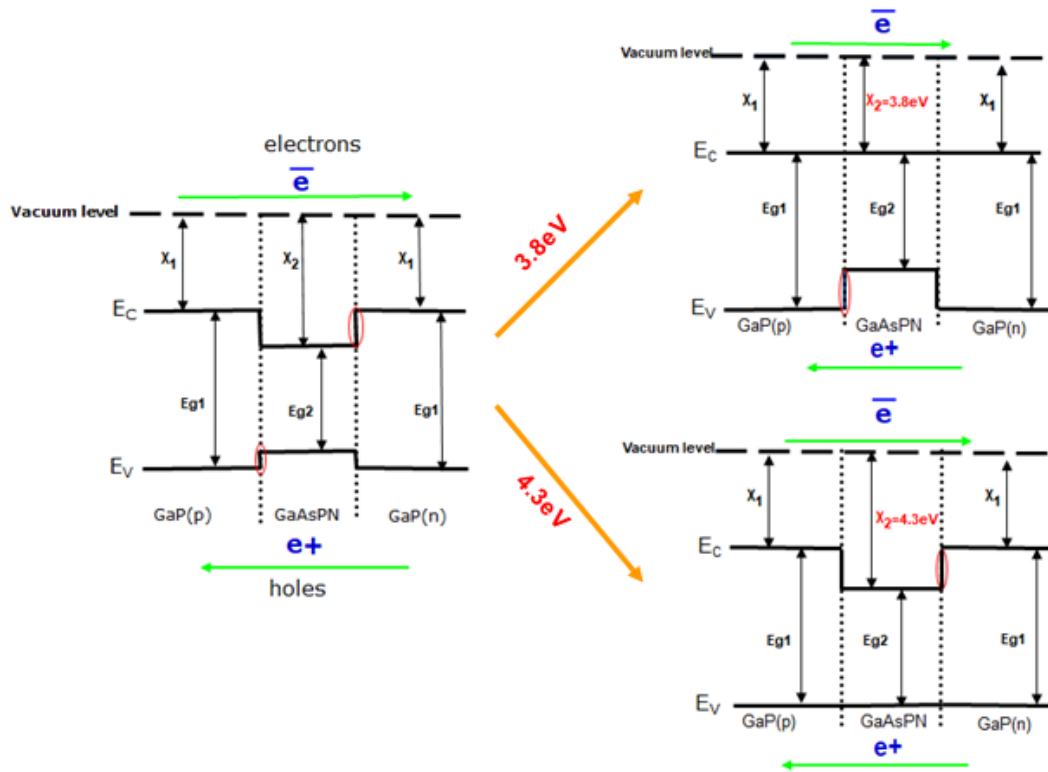


Figure 4.22. Top cell theoretical energy band diagram, where affinity( $x_1, x_2$ ), bandgap( $E_{g1}, E_{g2}$ ). The right top one is the affinity with 3.8eV energy band diagram; The right below one is the affinity with 4.3eV energy band diagram;

Red circles are band offset.

There is no doubt that band offsets transformation affects carriers transport and relevant EQE results. Figure 4.23 displays the simulation results. It shows that the EQE decreases when affinity increases. During all the simulation processes, just active layer affinity is changed. Then the energy band offsets will have corresponding changes in conduction band and in valence band. But the sum value of band offset in each model is constant, equaling 0.45eV. For further understanding, we calculate carriers density over barriers in energy bands for each case.

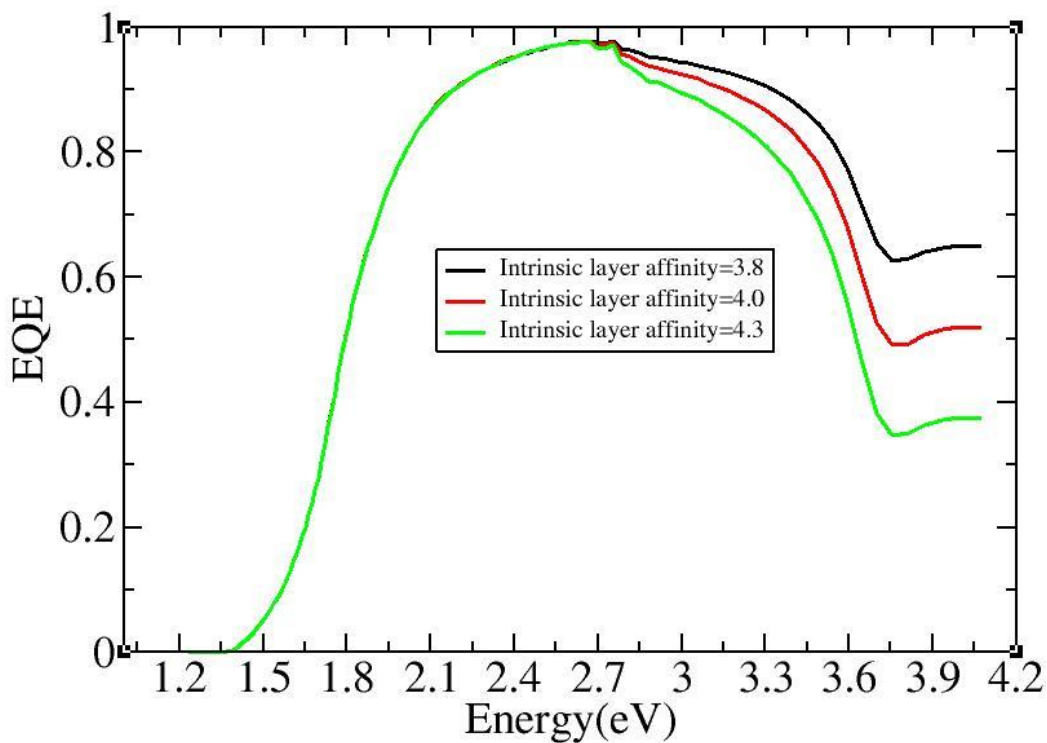


Figure 4.23. Top cell EQE simulation results with different active layer affinities. When photons energy bigger than 2.76eV, EQE difference of these three devices appears.

Table 4-3 shows the calculation results. As the active layer affinity increases, the holes density in valence band increases, simultaneously, the electrons density in conduction band decreases. This phenomenon is not hard to understand, because when the affinity increases, the band offset in conduction band increases, and the band offset in valence band decreases.

Table 4-3: Calculated carriers densities over barriers.

GaAsPN affinity	3.8(eV)	4.0(eV)	4.3(eV)
$h^+(\text{cm}^{-3})$	$7.5e11$	$5.1e14$	$4.7e15$
$e^-(\text{cm}^{-3})$	$2.3e16$	$2.3e15$	$2.8e11$

As previous mentioned, there is no barrier in conduction band and valence band as affinity equals to 3.8eV and 4.3eV. However for these two cases, they have the same band offset values existing in valence band and conduction band respectively as shown in Figure 4.22. After the electron-hole pairs are generated, electrons are transported in conduction band from p type GaP to n type GaP, by contrast, holes are transported in valence band from n type GaP to p type GaP. But from the calculation results, the former carriers (affinity=3.8eV) number over barrier is larger than latter case (affinity=4.3eV), finally, the number of collected carriers in former model are larger than the number of collected carriers in latter model. That is due to different density of states in conduction band ( $1.5e18\text{cm}^{-3}$ ) and valence band ( $8.75e18\text{cm}^{-3}$ ) and the different electron mobility and hole mobility. This result also follows the simulation results in Figure 4.23. We can conclude that conduction band barrier effect on carriers transport is more important than valence band barrier effect.

## 4.8 Study of tunnel junction

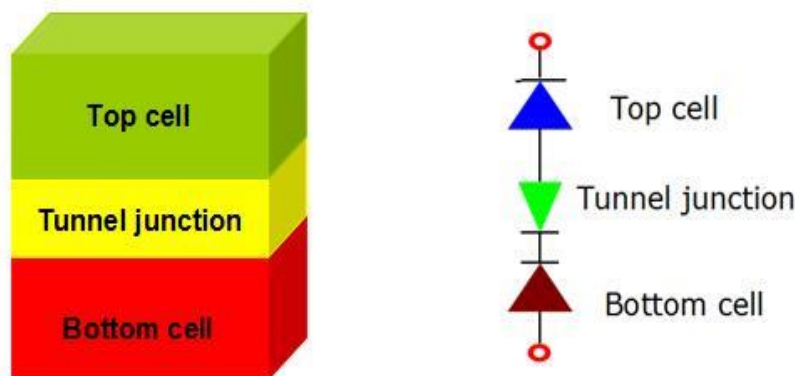


Figure 4.24. Tandem solar cell structure and simplified equivalent circuit diagram.

The function of tunnel is to realize electric connection of top and bottom junctions.<sup>158, 159</sup> If the top junction connects bottom junction directly, so diode (essentially it is a P-N junction) is under reverse voltage case. Due to diode performance, there is no current through the junction because of the existence of build-in electric field. That means it does not work, however, tunnel junction insertion can solve this problem. Figure 4.25 shows the performance of tunnel diode. It is apparent that even if the voltage over junction is negative, there is also current going through the total device.<sup>158,</sup>

177

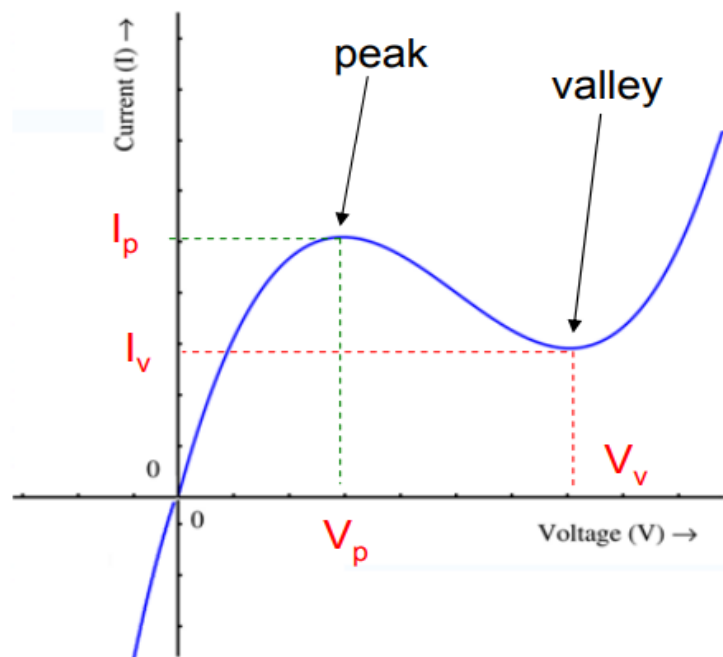


Figure 4.25. Tunnel diode characteristic of the current versus voltage.<sup>177</sup>

Considering the materials we used for tandem solar cells, the following four potential tunnel junction types, shown in Figure 4.26, are simulated:

GaP(n++)/GaP(p++), Si(n++)/Si(p++), GaP(n++)/Si(p++), GaP(p++)/Si(n++).

Otherwise, as described in Figure 4.11, GaP has a good lattice matching with Si. That can minimize the defects introduced by lattice mismatch. All the material parameters are default by SILVACO and the materials doping level are both as high as  $10^{20} \text{ cm}^{-3}$ , meanwhile, thicknesses of layers are 20nm.

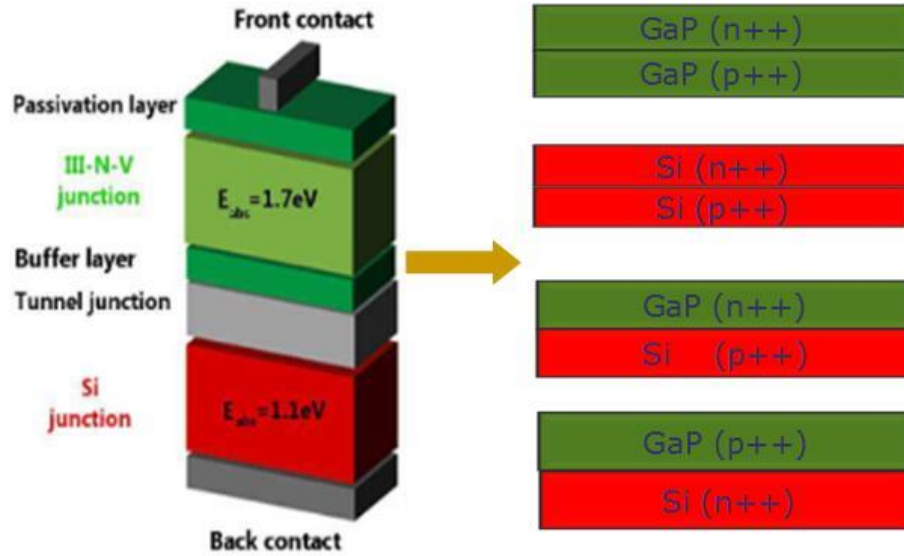


Figure 4.26. Tandem solar cell and potential tunnel junctions types.

From the Table 4-4 description, GaP(n++)/Si(p++), Si(n++)/Si(p++) present better results than the other two styles tunnel junction,<sup>158, 159</sup> and for the best GaP(n++)/Si(p++) tunnel junction, as illustrated in Figure 4.27, it has the narrowest barrier thickness, that makes carriers transport more efficient than the left structures, also has the highest peak current density. So finally, we choose GaP(n++)/Si(p++) as tunnel junction structure.

Table 4-4: Tunnel junction peak current densities.

Peak current densities  $I_p$ , barrier thickness  $L_B$ .

	GaP(n++)/Si(p++)	GaP(p++)/Si(n++)	GaP(n++)/GaP(p++)	Si(n++)/Si(p++)
$I_p(\text{mA}/\text{cm}^2)$	$8.4 \times 10^8$	$\sim 10^{-4}$	$\sim 10^{-3}$	$3.4 \times 10^5$
$L_B(\text{nm})$	3.3	6.9	5.9	4.4

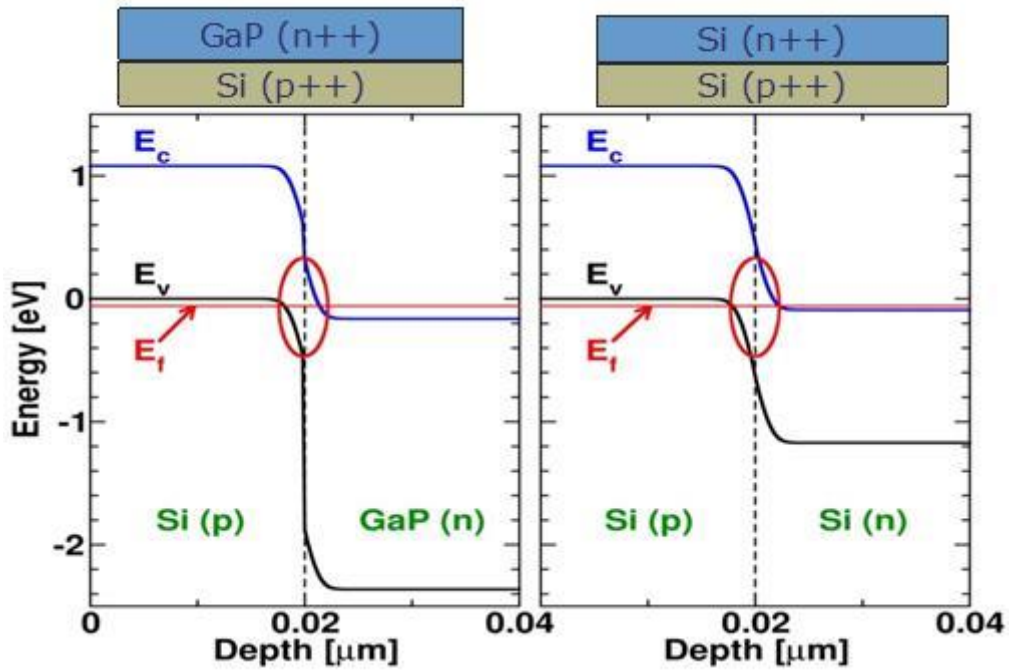
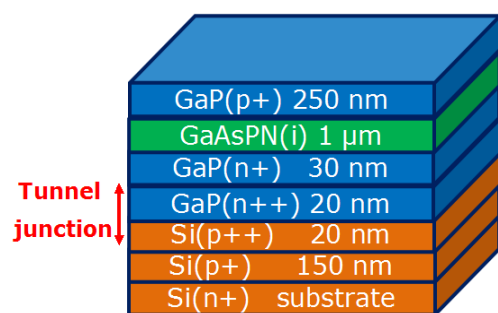


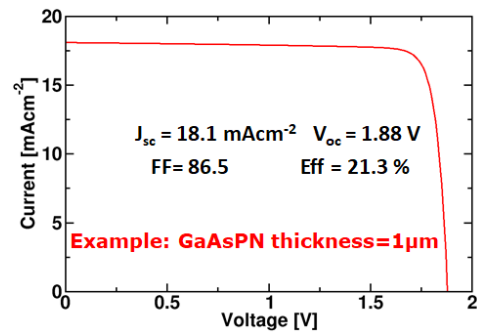
Figure 4.27. GaP(n++)/Si(p++), Si(n++)/Si(p++) tunnel junction simulated results. Si(p++) valence band is regarded as energy reference. Where  $E_c$ ,  $E_v$  are conduction band and valence band,  $E_f$  is Fermi level.

## 4.9 Tandem solar cell simulation

Based on all previous study, the tandem solar cell is simulated. All the relevant parameters used for simulation are shown in the tandem solar cell schematic structure. Active layer thickness is  $1\mu\text{m}$ , and GaP(n++)/Si(p++) structure is used for tunnel junction.



a



b

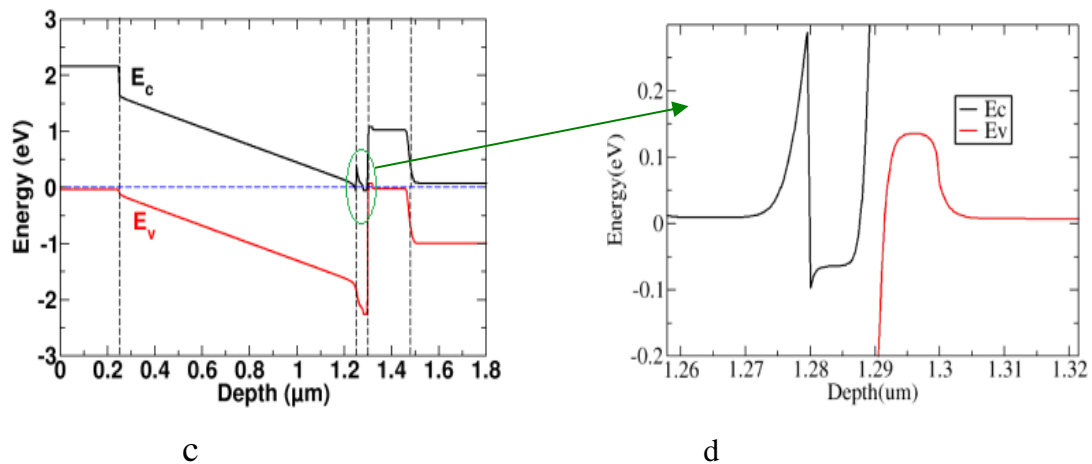
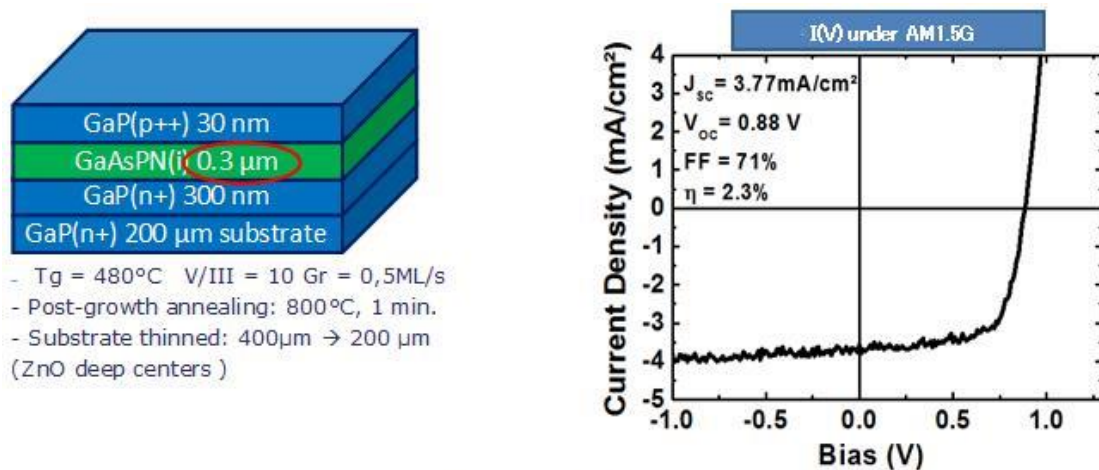


Figure 4.28. Tandem solar cell structure and attendant simulation results(a: The device structure diagram; b: The device I-V curve; c: The device energy band diagram; d: Partial energy band diagram magnification).

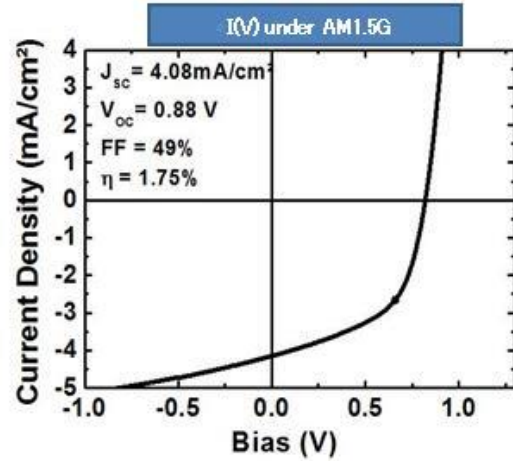
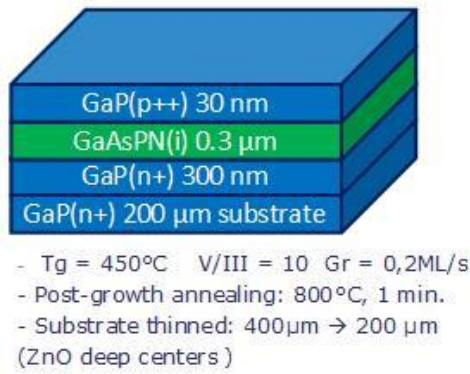
From the energy band diagram, Figure 4.28 c and d, we can observe the existence of band offset and tunnel junction. Although the simulated performance results don't express as high as calculated in Figure 4.10, it could provide a way to analyze and optimize the structure.

## 4.10 Fitting experimental results

For top cell fabrication, the structures and its parameters are presented in the following Figure 4.29. Also up to now, these two fabrications device performances are the best we got in lab. 200μm thickness n type GaP(n+) is used as substrate, then GaP(n+), GaAsPN and GaP(p++) layers are grown orderly, after that in order to obtain the optimal optical properties, annealing process is requested.



### Experiment 1



## Experiment 2

Figure 4.29. Top cell structure and attendant results of FOTON lab (Where  $T_g$ ,  $V/\text{III}$ ,  $Gr$  are the growth temperature, ratio of the III/V elements, beam equivalent pressures during the growth and growth rate).

For the primary step, in order to simplify the model, we assume the main deep traps are supposed in bulk GaAsPN active layer, and the most of carriers recombination also occurs in this layer. GaP layers parameters are default values by SILVACO. So bulk traps are introduced in active layer, and through adjusting other parameters, just like decreasing minority carriers lifetime and mobilities to fitting the results. For the present stage, the surface defects and other factors are not taken into account, that is why the simulation result is close to the experiment result, but does not fit very well as displayed in Figure 4.30. Also many elements should be mentioned, besides, further and better fitting simulation should be done and got.

Table 4-5: Fitting simulation materials' parameters

	Thickness ( $\mu\text{m}$ )	Doping ( $\text{cm}^{-3}$ )	Lifetime (s)	Mobility ( $\text{cm}^2\text{V}^{-1}\text{s}^{-1}$ )	Bandgap (eV)	Affinity (eV)
GaP	0.03	$N_A=2e19$	$\tau_n=\tau_p=1e-7$	$\mu_n=150, \mu_p=40$	2.2	3.8
GaAsPN	0.3	Intrinsic	$\tau_n=\tau_p=1.5e-13$	$\mu_n=100, \mu_p=80$	1.75	4.3
GaP	0.3	$N_D=2e18$	$\tau_n=\tau_p=1e-7$	$\mu_n=150, \mu_p=40$	2.2	3.8
GaP	200	$N_D=2e17$	$\tau_n=\tau_p=1e-7$	$\mu_n=150, \mu_p=40$	2.2	3.8

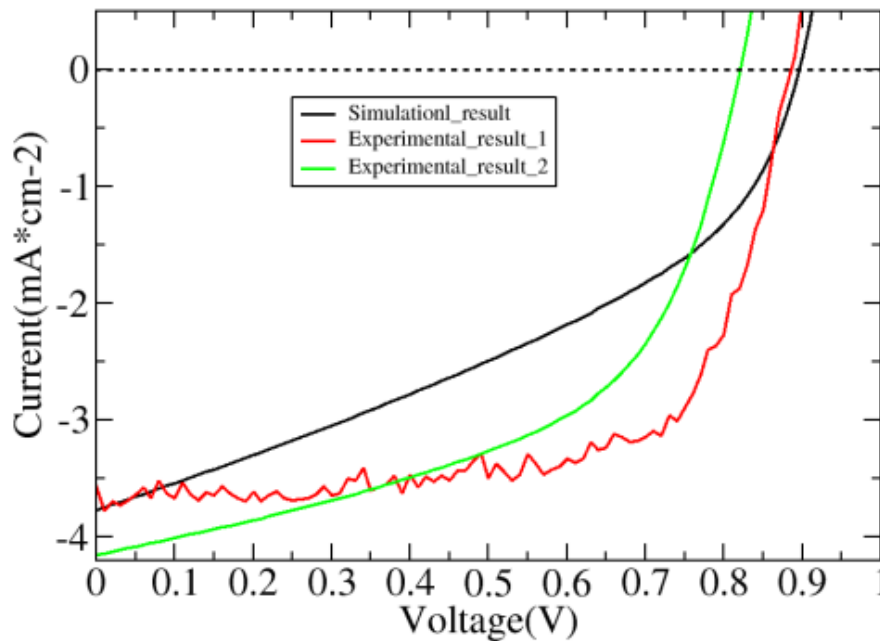


Figure 4.30. Fitting experimental results(The red and green lines are the previous experiment 1 and experiment 2 I-V curves, the black one is the simulated I-V curve based on the same structure parameters).

From the fitting results, it is obvious that simulation result is not very good in agreement with experimental results. Even there is some distance between them, but the good aspect is that they have the same tendency and the distance is not far away. Of course, further research simulation should be done for getting good fitting result based on more experimental measurement to extract material parameters.

## 4.11 Conclusion

In summary, the promising combination GaAsPN/Si tandem solar cell, in our simulation, the best absorber layer range 1-1.5 $\mu\text{m}$  range is confirmed but it has to be optimized. Indeed, we have shown that the graded layers insertion at the interface forming by GaAsPN and GaP(n) can increase carriers transport hindered by conduction band offset. Furthermore an appropriate graded material should be the final way to reach high efficiency close to the expected value. GaP(n $^{++}$ )/Si(p $^{++}$ ) structure used for tunnel junction shows the best performance among all the potential candidates. For further study of absorber layer, finding the reasons affecting its performances, simulation model and more material parameters should be refined.

## **Annex**

In SILVACO, EQE simulation can be done through defining LAMBDA on SOLVE statement to do this process. Take an SILVACO example:

```
solve b1=0.001 beam=1 lambda=0.3 wstep=0.02 wfinal=1.2
```

Here, solve is the solution specification; Intensity is set to 1 mW by b1 parameter. The BEAM parameter identifies the optical source. LAMBDA defines original wavelength in microns, WFINAL specifies the final wavelength in microns, and WSTEP specifies the wavelength step in microns.

## Conclusions

In the first part, the first 3 chapters, we present the origami W-shaped nanostructure corresponding knowledge.

The origin of W structure is from the origami idea. Fold the flat metal lay into W shape. And corresponding primary simulation results show that it possesses a good sensitivity.

Principle shows it is feasible to obtain W-structure. The subsequent fabrication of W structure is based on Si substrate covered with Si<sub>3</sub>N<sub>4</sub> mask layer due to Si anisotropic property. Experience indicates that crystal orientation alignment in EBL writing pattern process plays a critical role. So the circle reference method and edge reference method are introduced for solving this issue. Experiments also prove both of them work. And through optimization of parameters, different periods W-structures can be fabricated. Due to the bad adhesion between Si and Au layer, finally excellent metallic W-structure can be reached with Ormo-products.

Simulation tools differential method and chandezon method are used for extra analyze. At the beginning, a good agreement is observed between experimental and simulated transmission results. Based on that, far field and near field properties of different period W structures are studied under the help of simulation. Although some phenomena are beyond our knowledge, they own a strong dependence on structure periods and a promising future in applications.

In the first part, the forth chapter, we emphasis on tandem solar cell based on III-V(GaAsPN) and Si substrate, owing to its theoretical high efficiency and potential low cost. We study this tandem solar cell by Silvaco based on the mere parameters we have. Simulation results show that the relative active layer thickness is 1-1.5um. And the graded layers can suppress the negative effect of carriers transport induced by band offset in valence band and increase the device performance. Meanwhile, GaP(n++)/Si(p++), Si(n++)/Si(p++) are more eligible candidate of tunnel junctions by

the virtue of narrower barrier thickness which can make more carriers to be collected. The fitting results between experiments and simulations illustrate that because of lack of active layer parameters, they have the same tendency but there is still some space existence.

## **French summary**

# **Chapitre 1 Plasmonics: Nanostructure métallique en forme de W**

## **1.1 Plasmons de surface**

Comme d'habitude, l'oscillation collective des électrons de surface dans la bande de conduction métallique apparaît pendant que les électrons interagissent avec l'électromagnétique incident, tandis que sous la force de restauration des noyaux, les ions oscillants reviennent. Lorsque le champ électromagnétique incident a la même phase et la même fréquence que l'onde oscillante, la résonance se produit et le champ du champ d'ondes plasmatiques atteint le sommet.

Les plasmons de surface ont deux catégories principales: l'une d'entre elles est que la surface du métal est plate et longue portée, comme le montre la figure 1.1a, elle est toujours appelée polaritons de plasmon de surface (SPP); L'autre classe est que le métal est une nanoparticule dont la taille est inférieure à la longueur d'onde de la lumière incidente. Dans ce cas, les plasmons de surface sont souvent appelés plasmons de surface localisés (LSP), comme indiqué sur la figure 1. 1b.

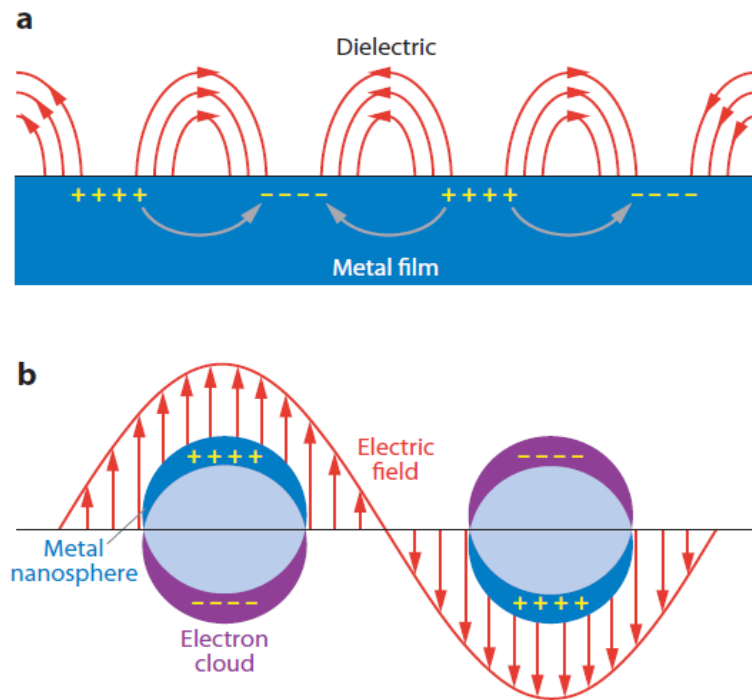


Figure 1.1. (a) Propagation de plasmons de surface sur une surface métal / diélectrique; (b) des plasmons de surface localisés d'une nanoparticule métallique.

## 1.2 Désintégration d'énergie des plasmons de surface localisés

L'énergie localisée des plasmons de surface se désintègre principalement selon trois processus: la désintégration radiative, la désintégration non radiative (absorption) et la désintégration dynamique de la dépolarisation. Les deux premiers processus sont illustrés à la figure 1.5.

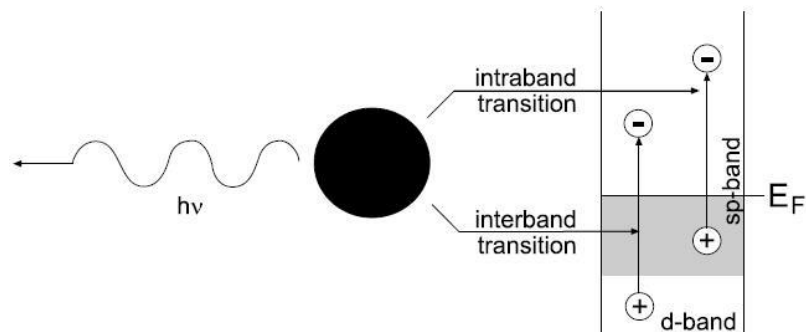


Figure 1.5. Décomposition radiative et non radiative des plasmons particuliers.

La désintégration radiative est une voie de transformation des plasmons de particules en photons. Elle prend la principale proportion de désintégration pour les nanoparticules à grand volume. Le processus de désintégration non radiative découle de

la création de paires électron-trou via une excitation intra-bande dans la bande de conduction ou des transitions entre bandes d'une bande à basse énergie à une bande haute.

### **1.3 Influence des facteurs sur la LSPR**

Le modèle d'analyse de la théorie de Mie nous indique que divers facteurs ont une relation avec le résultat de LSPR. Comme le matériau des nanoparticules, taille, forme, environnement et espacement des nanoparticules.

### **1.4 Applications de LSPR**

En raison des excellentes performances de LSPR, des chercheurs de différents domaines ont porté leur attention sur des études pertinentes. En conséquence, les nanoparticules métalliques sont utilisées dans une série d'applications, telles que les applications nanophotoniques, les biocapteurs, les dispositifs photovoltaïques, la détection biomoléculaire, les capteurs chimiques, la spectroscopie Raman à surface améliorée. etc.

### **1.5 Origine et motivation de la structure "W"**

La structure en "W" provient de la surface de propagation du plasmon. Comme indiqué dans le texte précédent, la surface de propagation qui se propage au plasmon est générée au niveau de l'interface longue et plate. Dans ce cas, nous proposons de remplacer l'interface plate par la structure en "W" présentée dans la figure 1.11 suivante.

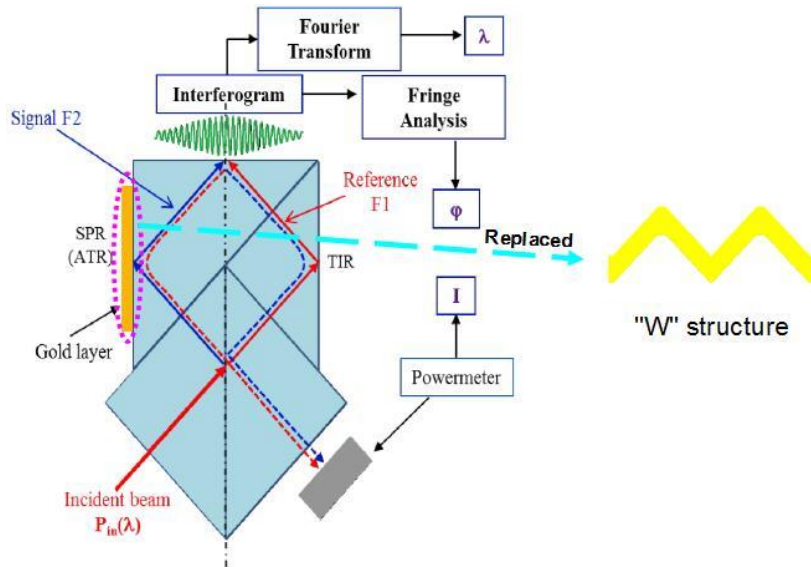


Figure 1.11 L'origine de la structure en "W" provient du schéma du spectromètre d'échantillonnage bidirectionnel couplé (CoBiSS).

## 1.6 Simulation de recherche de structure primaire "W"

La partie simulation est réalisée par Rohit. Les détails sont décrits dans sa thèse. Ici, nous venons d'en citer une partie. Au début, pour la recherche primaire, un ensemble de paramètres de structure "W" est défini comme suit: L'angle  $\alpha = 35,3^\circ$ . Et la lumière incidente a un angle fixe de  $45^\circ$ . Au départ, pour les besoins du test, le grand segment n'est pas défini comme constant; ses valeurs varient donc de 400 à 1000 nm par incréments de 200 nm. Pour l'épaisseur de la couche d'or, on utilise 10, 20, 30, 40, 50, 60 nm pour chaque grande structure de segment. Pendant ce temps, la longueur d'onde de la lumière est comprise entre 400 et 900 nm.

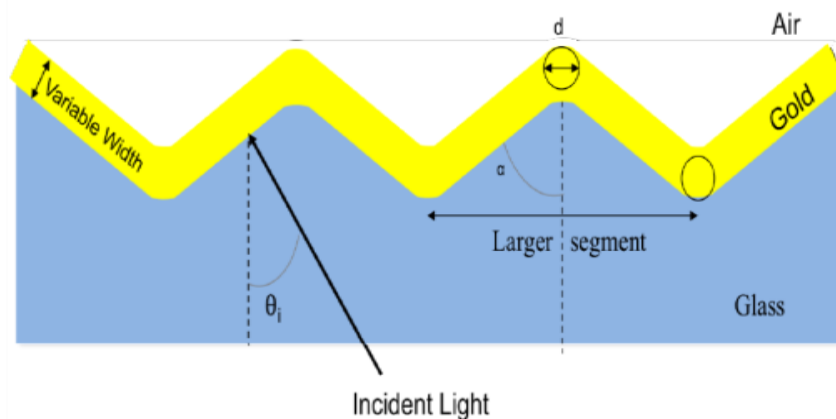


Figure 1. 12. CoBiSS modifié pour la détection de SPR avec structure modifiée en "W" avec  $2 \times \text{rayon} = \text{diamètre} = 10 \text{ nm}$ .

Enfin, les résultats de la simulation sont présentés à la figure 1.13. Les courbes de réflectance correspondant à différents indices de réfraction du matériau sont marquées avec des couleurs différentes.

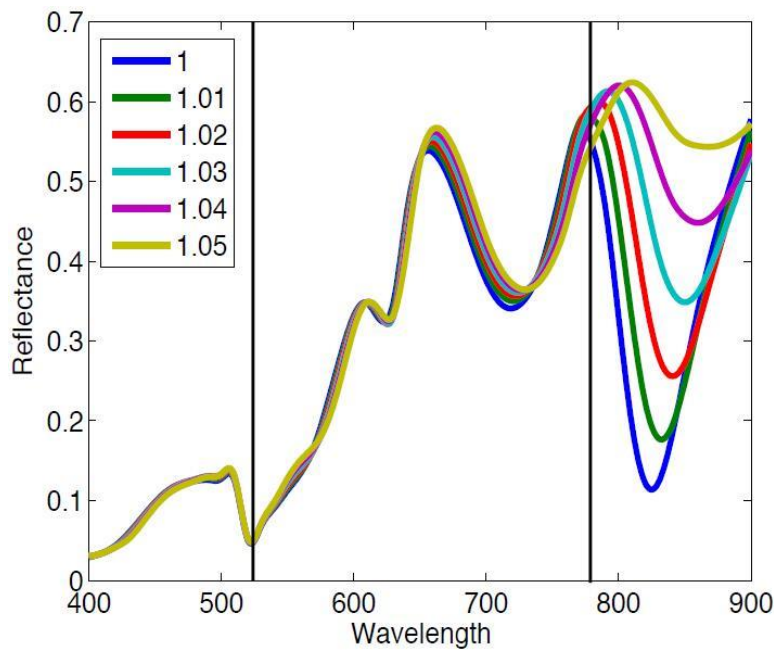


Figure 1. 13. Effet de la réflectance avec la variation de la longueur d'onde d'un indice de réfraction multiple de la structure de couche au-dessus de l'or "W" variant de 1 à 1,05, respectivement.

Les courbes de réflectance des matériaux commencent à se séparer avec une différence distincte, qui sont marquées par un cercle orange. Il ne fait aucun doute que cette partie avec une distinction remarquable est très importante pour la sensibilité du dispositif, et cette performance appliquée dans des applications pratiques peut faciliter les analyses. Cela signifie que la structure "W" possède une bonne sensibilité et que son application est prometteuse.

## Chapitre 2 Expérience

Afin d'atteindre l'objectif de la structure en "W", la fabrication comprend principalement deux parties: la fabrication du modèle de la structure "W" et les processus de fabrication de la structure en "W" métallique.

### 2.1 Principe du processus de formation de la structure en "W"

Le principe de fabrication est illustré à la figure 2.1. Le substrat (figure 2.1 (a)) est en Si recouvert de nitrure de silicium ( $\text{Si}_3\text{N}_4$ ) servant de couche de masque; Figure 2.1 (b), une partie de  $\text{Si}_3\text{N}_4$  est déplacée sous forme de rectangles espacés les uns des autres, de sorte que le Si inférieur est exposé. Figure 2.1 (c), en raison de la propriété anisotrope de Si, la vitesse dans le plan (100) (repère rouge) est supérieure à celle dans le (111) plans (repère bleu). Ainsi, au début de la gravure, des rainures trapézoïdales apparaissent; ensuite, les rainures trapézoïdales se transforment en rainures triangulaires, comme illustré à la figure 2.1 (d); Lorsque la gravure est appropriée, le sommet adjacent des rainures triangulaires se rencontrent et la structure en «W» est réalisée (figure 2.1 (e)); L'étape suivante consiste à quitter le calque de masque (Figure 2.1 (f)). Enfin, le modèle "W" est acquis.

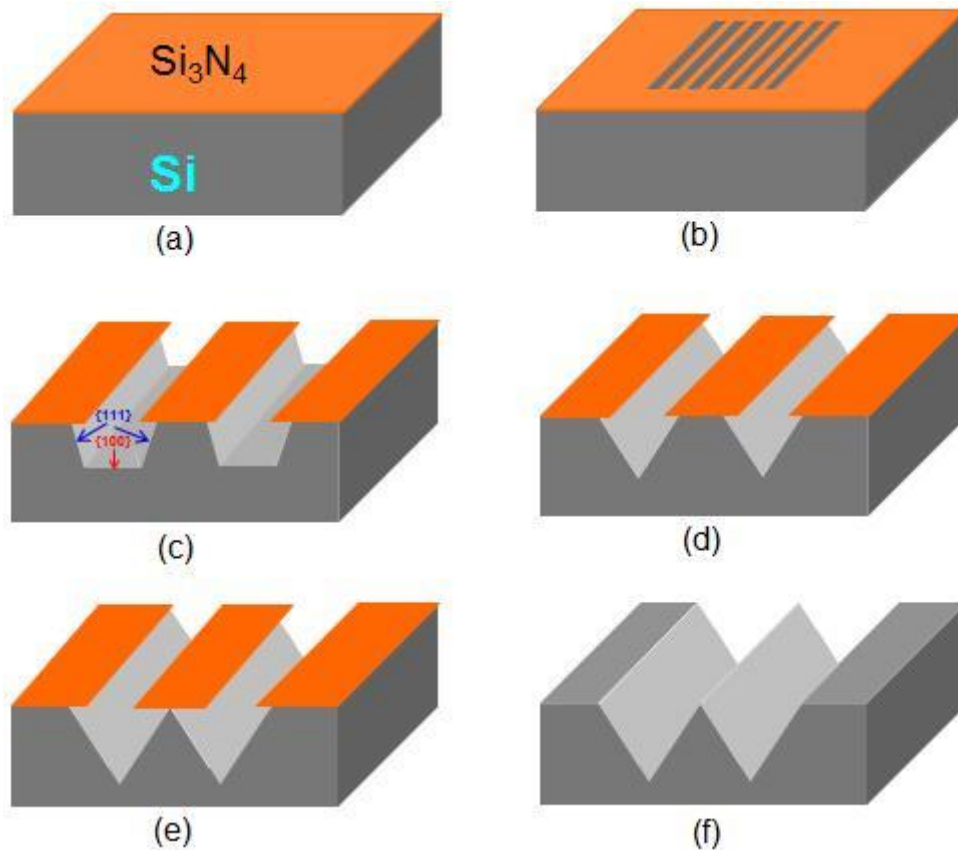


Figure 2.1. Principe du procédé de formation de structure en "W" à base de substrat de Si recouvert d'une couche de masque de Si<sub>3</sub>N<sub>4</sub>. (a) substrat de Si recouvert de Si<sub>3</sub>N<sub>4</sub>; (b) Éloignez une partie de Si<sub>3</sub>N<sub>4</sub> pour exposer Si; (c) Commencez à graver, des rainures trapézoïdales apparaissent; (d) des rainures triangulaires apparaissent; (e) la structure en "W" apparaît; (f) On acquiert un modèle de structure en forme de "W" avec déplacement de la couche de masque.

## 2.2 Fabrication de la structure en "W"

Les principales technologies microélectroniques de notre expérience consistent à adopter du poly (méthacrylate de méthyle) (PMMA) comme couche de masque, puis à utiliser la lithographie à faisceau électronique pour écrire le motif conçu sur du PMMA, puis à utiliser la gravure ionique réactive (RIE) pour éliminer Si<sub>3</sub>N<sub>4</sub> et PMMA afin d'exposer le Si après gravure humide. Ci-après, les processus de fabrication sont décrits.

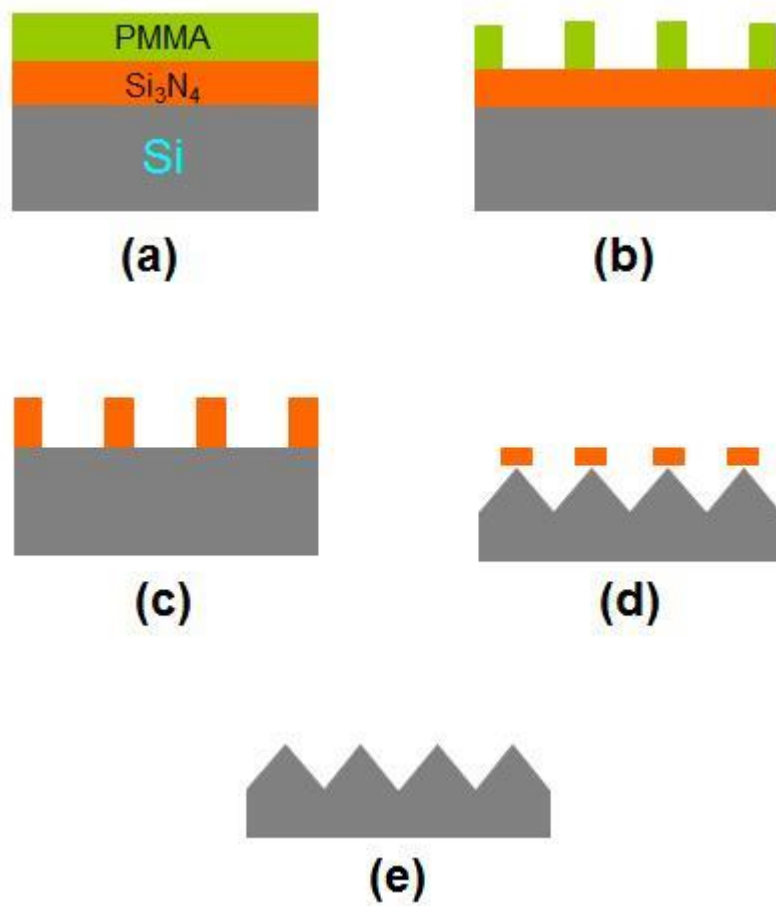


Figure 2.2. Procédés de fabrication de la structure en "W" à base de substrat de Si recouvert d'une couche de Si<sub>3</sub>N<sub>4</sub>. (a) revêtement de résine photosensible; (b) Photolithographie et processus de développement pour écrire les modèles conçus; (c) le processus de gravure RIE élimine la couche de masque à motif Si<sub>3</sub>N<sub>4</sub> et le PMMA afin d'exposer le Si; (d) procédé de gravure humide pour former une structure en "W"; (e) La couche de masque se déplace pour obtenir une structure en "W" nu.

## 2.3 Modèle de structure "W" final

Grâce aux explorations, analyses et tests expérimentaux précédents, nous obtenons enfin des paramètres de fabrication relativement importants. Enfin, nous le gagnons comme indiqué dans les images suivantes.

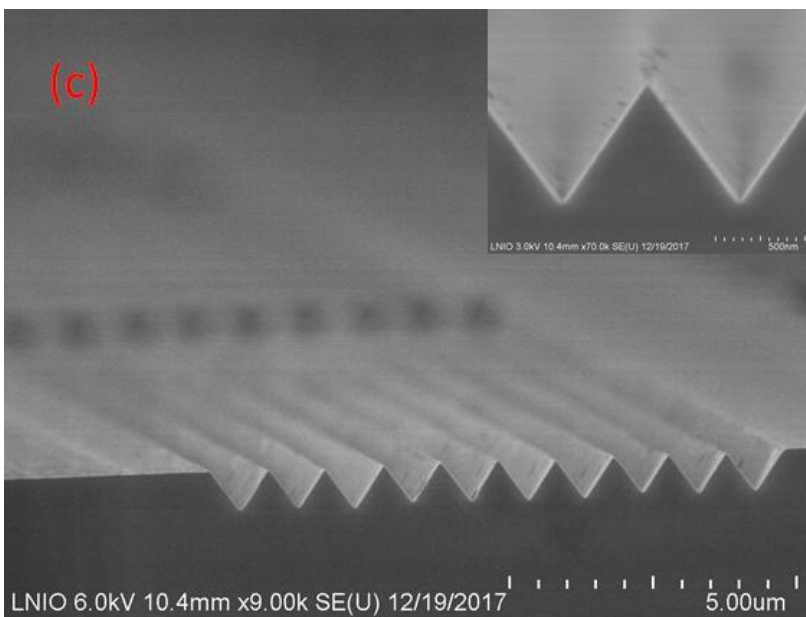
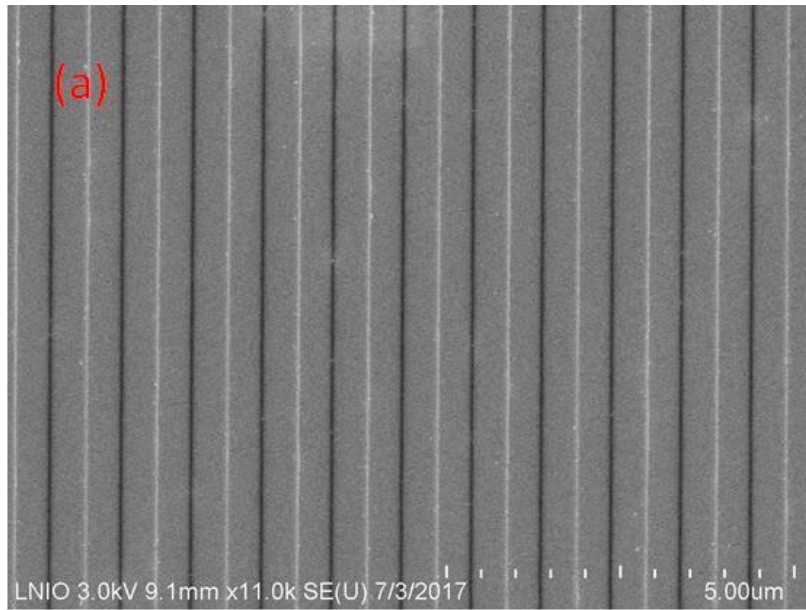


Figure 2.16 Images SEM de la structure Si "W". (a) image de vue d'ensemble; (b) image de zonage de la pointe; (c)

Image en coupe.

## 2.4 Fabrication de structures métalliques "W"

Une fois la fabrication du modèle de structure en "W" terminée, le métal est déposé sur la surface du modèle. L'enlèvement de matrice est utilisé pour soulever le métal, et le métal est facile à enlever en raison de la mauvaise adhérence entre la couche de métal et la surface de Si.

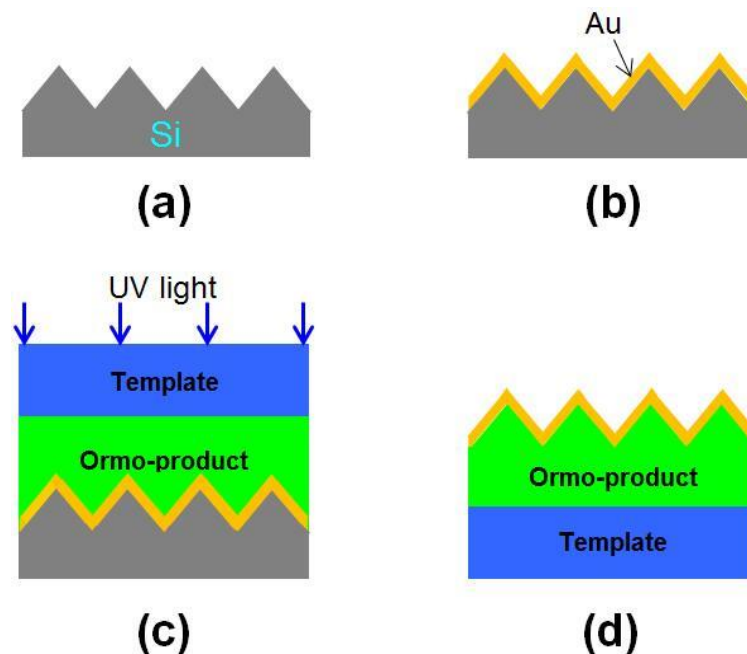


Figure 2.17 Schéma de dépouillement de la structure métallique en "W". (a). Bared Si "W" structure; (b). Au dépôt;

(c) Dépôt de polymère, couverture de modèle et exposition à la lumière UV; (d) Après le décapage du métal, on

obtient la structure métallique inversée en "W".

En même temps, après le stripping du métal, afin de vérifier le résultat du stripping, l'image au MEB de la surface du métal est prise, comme le montre la figure 2.20 (a). Il est nécessaire de revenir pour mesurer la surface de Si afin de vérifier s'il reste du métal collant au substrat de Si. La figure 2.20 (b) montre le résultat de la surface du substrat en Si après le processus de stripping du métal. Cela prouve que le décapage des métaux est réussi et complété.

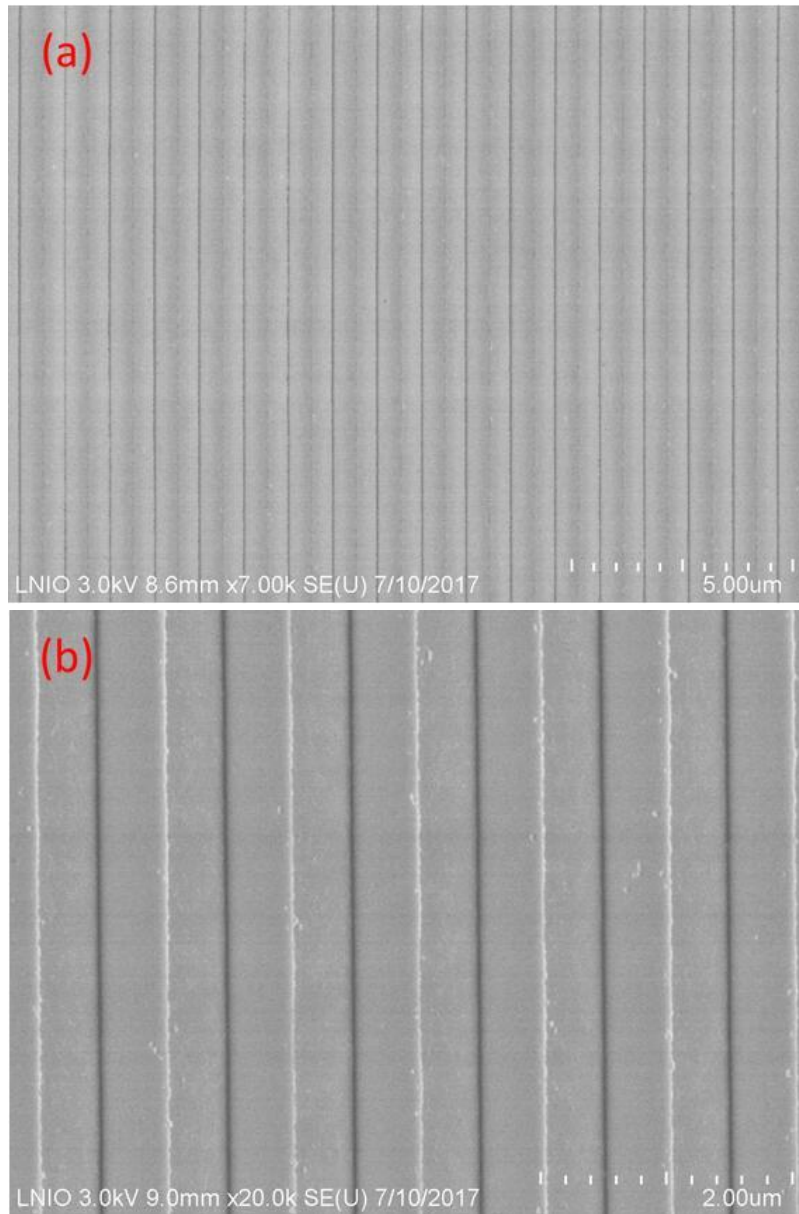


Figure 2.20 Les images au MEB du décapage du métal résultent: (a) de la structure en métal "W"; (b) surface de Si après décapage.

# Chapitre 3 Propriétés optiques des nanocouches métalliques pliées en 2D

Expérimentalement, les structures étudiées dans ce chapitre sont constituées de structures en or en forme de W déposées sur une surface de verre via un polymère d'indice de réfraction  $n = 1.55$ . Nous nous sommes concentrés sur deux échantillons avec une période de 400 nm et 600 nm. L'épaisseur des dépôts d'or est de 50 nm dans les deux cas. Le demi-angle des coins de la structure est de  $35.3^\circ$ . Plage de 400 à 950 nm pour l'angle d'incidence de  $0^\circ$  à  $50^\circ$  et pour les polarisations linéaires TM (p) et TE (s).

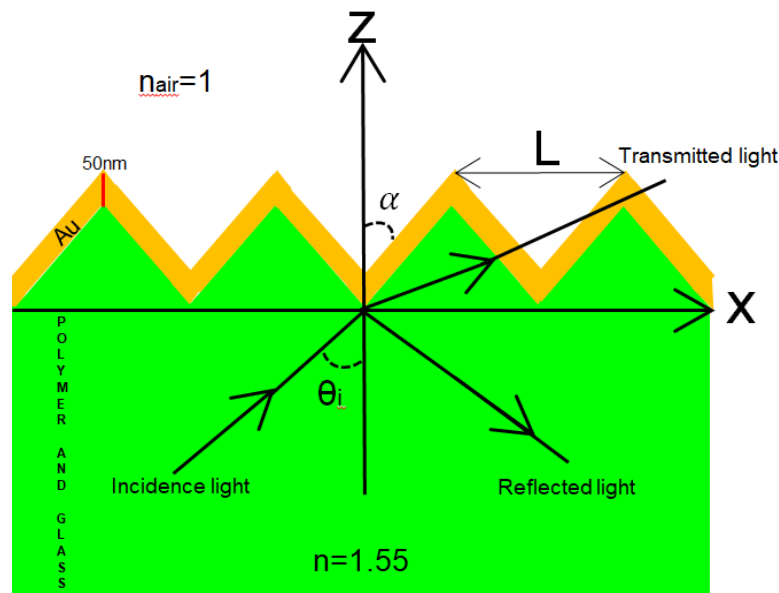


Figure 3.1 Schéma de la mesure de la structure en W. La lumière d'incidence provient du côté du verre et du polymère avec une permittivité de 1.55. L'épaisseur de la couche d'or est de 50 nm, comme indiqué sur la figure. Les périodes de structure L sont 400nm, 600nm. Le demi angle de coin  $\alpha = 35.3^\circ$ .

Nous utilisons la méthode Chandezon (également appelée méthode C) pour effectuer des simulations, introduites pour la première fois en 1980 par Chandezon et qui ont ensuite fait l'objet de nombreuses améliorations de la part de divers auteurs.

## 3.1 Description des résultats expérimentaux

Les figures 3.3 et 3.4 montrent des cartes du coefficient de transmission en fonction

de l'angle d'incidence et de la longueur d'onde. De bons accords sont observés entre les expériences et les théories tant pour la forme des variations en fonction de  $\theta$  et  $\lambda$  que pour les valeurs absolues des coefficients T (l'échelle de couleur est la même pour la théorie et la mesure et pour TE et TM).

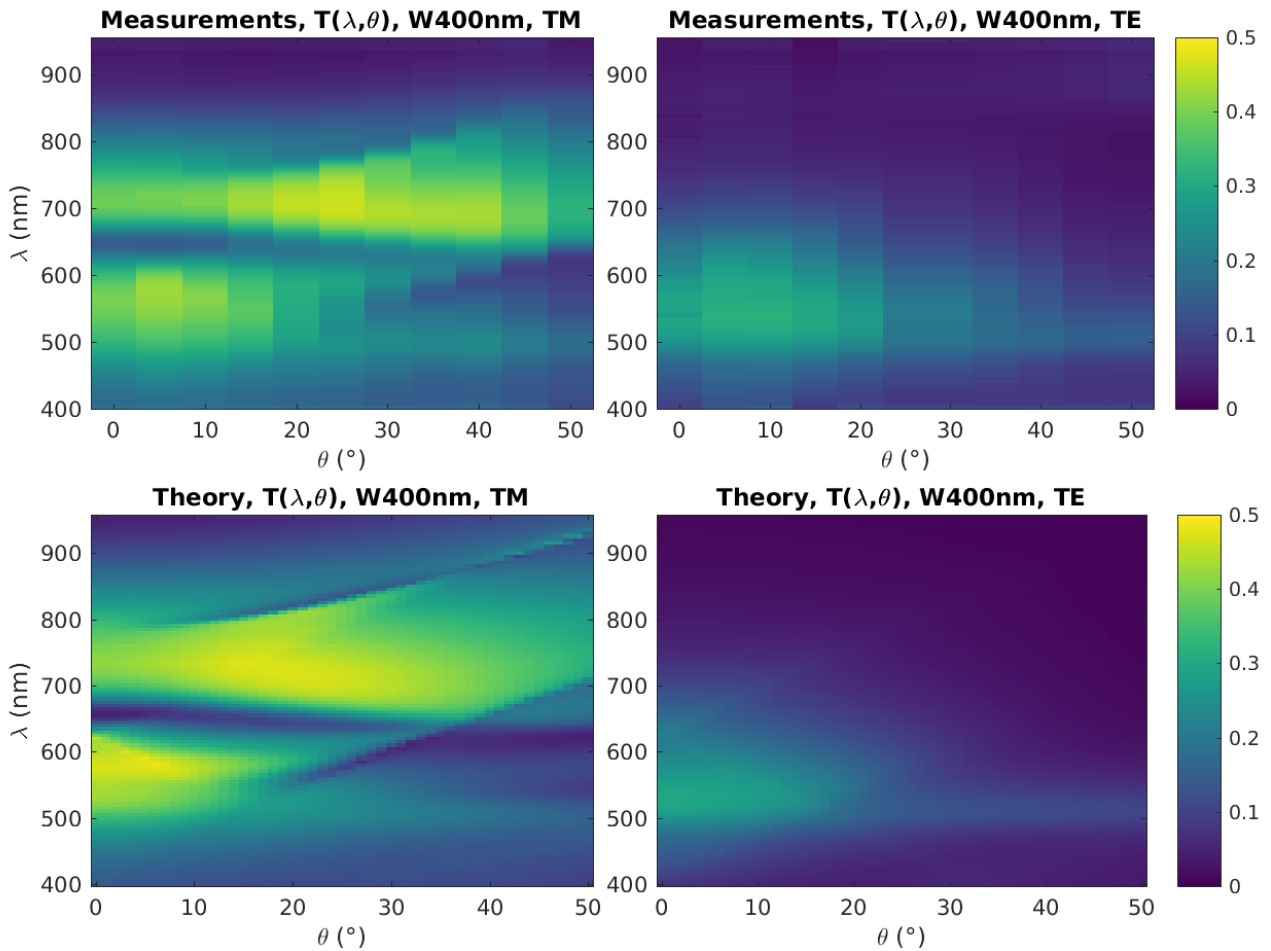


Figure 3.3 Coefficient de transmission d'une structure en or W avec une période de 400 nm et une épaisseur de 50 nm dans le domaine visible et proche IR (rayonnement infrarouge) (400 à 950 nm, axe vertical) et pour différents angles d'incidence de  $0^\circ$  à  $50^\circ$  (axe horizontal). Mesures (en haut) et calculs utilisant la méthode différentielle (en bas) pour les deux polarisations linéaires TM (p) à gauche et TE (s) à droite. L'échelle de couleur est la même pour les figures gauche et droite.

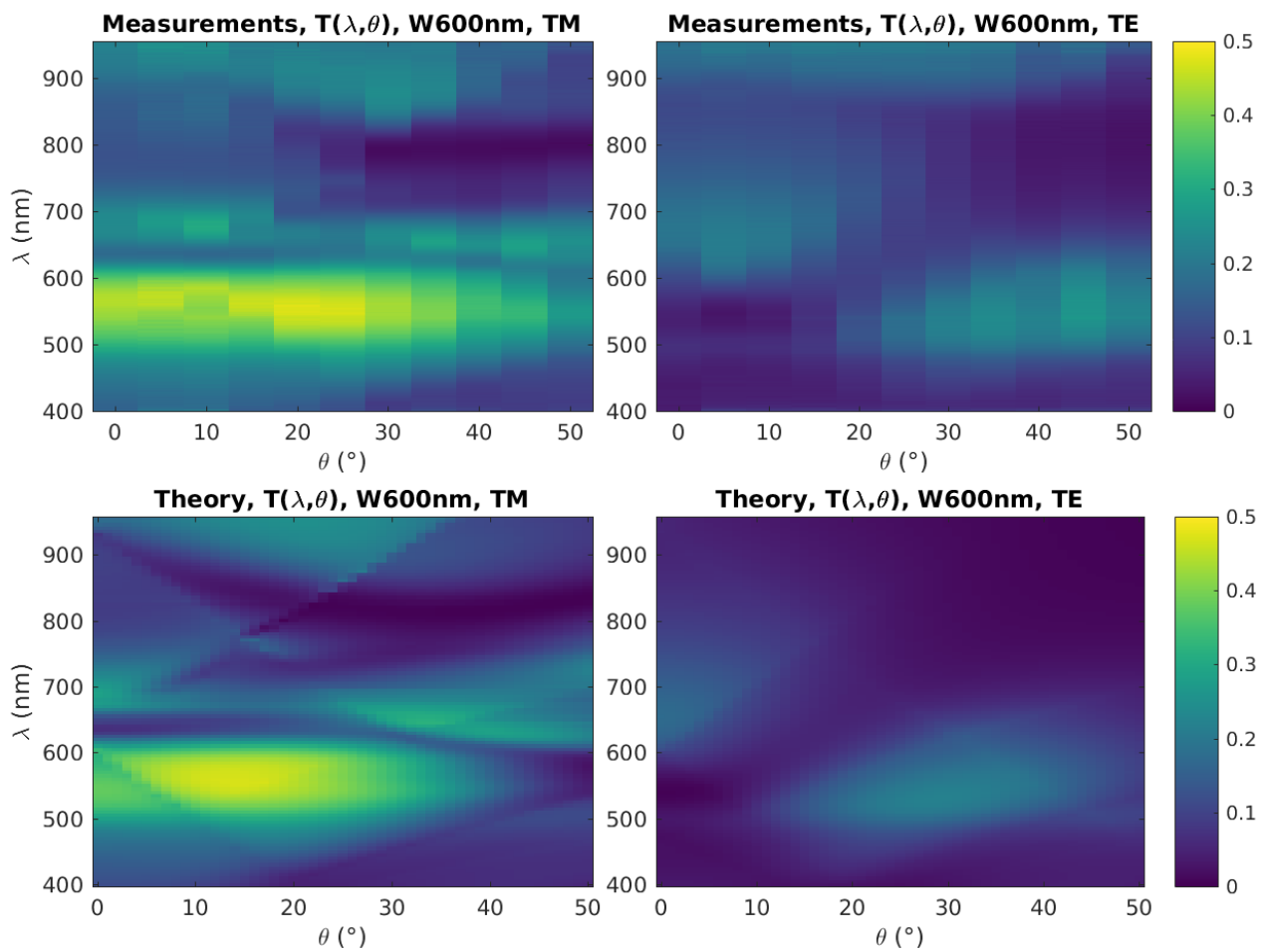


Figure 3.4 Identique à la figure 3.3, mais pour une structure W avec une période de 600 nm.

### 3.2 Effet de l'existence d'ordres de diffraction sur la variation des coefficients d'absorption, de réflexion et de transmission

D'après les résultats, il est évident que l'existence d'ordres de diffraction est sensible à l'angle d'incidence, à la longueur d'onde et à la période.

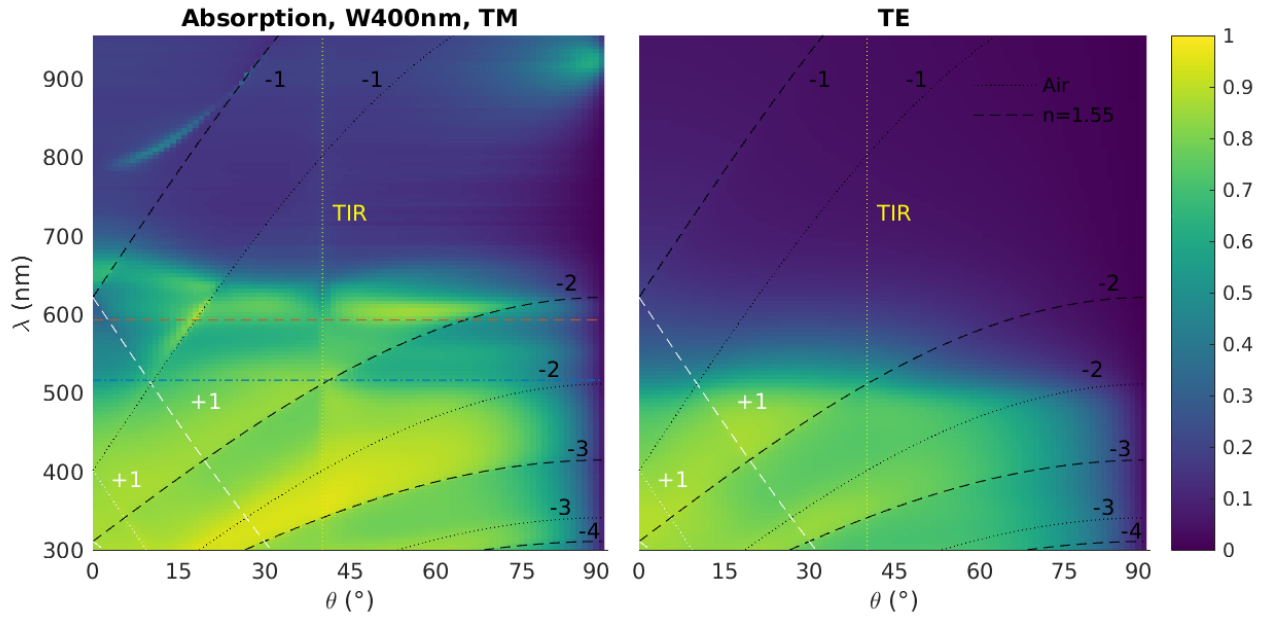


Figure 3.6 Absorption calculée pour la structure en or W avec une période de 400 nm pour les polarisations TM et TE. Les lignes noires et blanches, en pointillés et en pointillés correspondent à la limite d'existence des ordres de diffraction qui se superposent à la carte et correspondent à une variation dont il est question dans la partie 4.1. Les lignes horizontales bleues et rouges aux longueurs d'onde de 516nm et 593nm correspondent à des résonances théoriques approximatives de coin en or dans l'air et le verre, respectivement, qui seront discutés dans la partie 5.2. La ligne verticale jaune à  $40,2^\circ$  correspond à l'angle de réflexion interne total (TIR) du verre ( $n = 1,55$ ) à l'air.

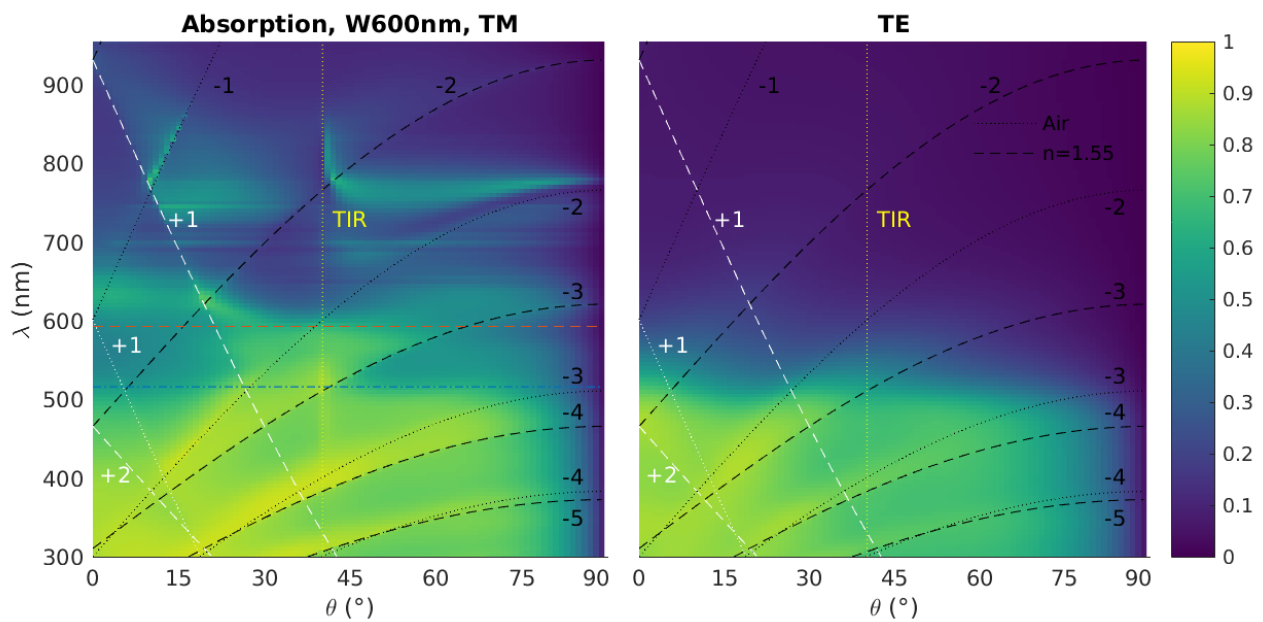


Figure 3.7 Identique à la figure 3.6. Pour une structure en or W avec une période de 600 nm.

### 3.3 Propriétés du champ local des structures en or W obtenues par modélisation électromagnétique

La performance de la structure sous différentes longueurs d'onde et angles d'incidence est simulée. Certains phénomènes intéressants sont présentés dans les résultats.

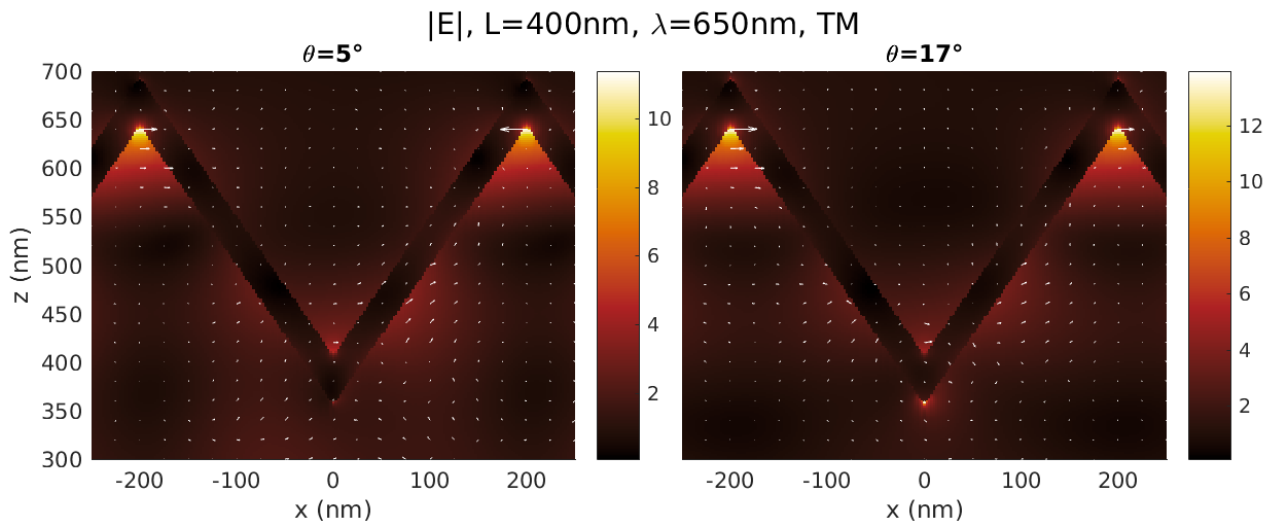


Figure 3.14 Amplitude et direction instantanée du champ électrique local pour une longueur d'onde de 650 nm et des angles d'incidence de  $5^\circ$  et  $17^\circ$  en polarisation TM. Remarquez l'amélioration du champ à l'extrémité inférieure et les directions des champs électriques dans le coin supérieur.

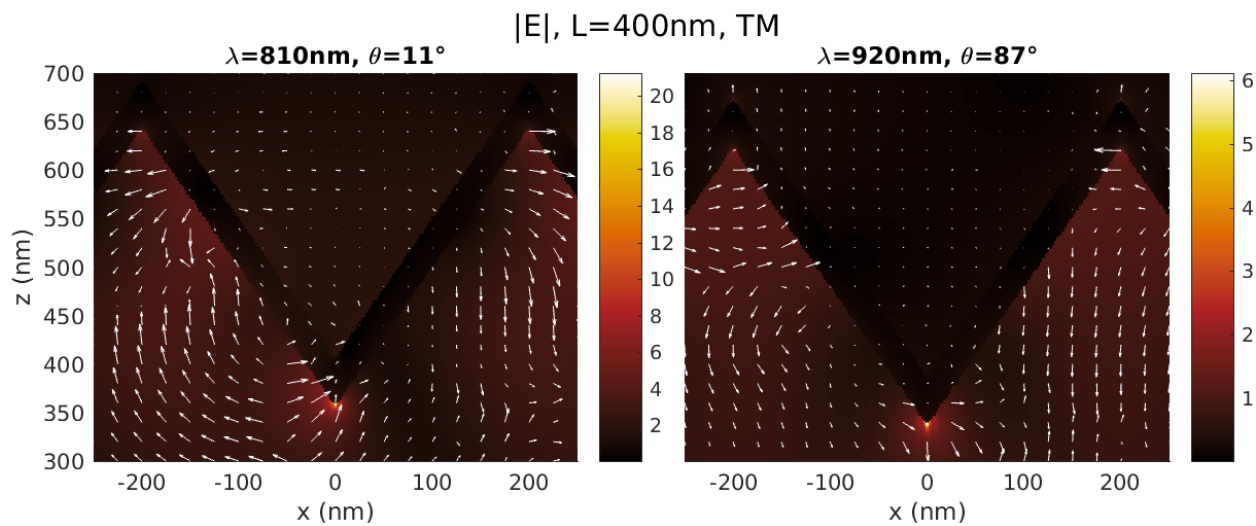


Figure 3.15 Amplitude et direction instantanée du champ électrique local pour une longueur d'onde de 810 nm et

une incidence de  $11^\circ$  et une longueur d'onde de 920 nm et une incidence de  $87^\circ$  en polarisation TM.

# Chapitre 4 Simulation numérique de cellules solaires tandem sur silicium

Ce chapitre est consacré à la simulation de cellules solaires tandem de III-V (GaAsPN) sur silicium.

## 4.1 Structure de cellule solaire tandem

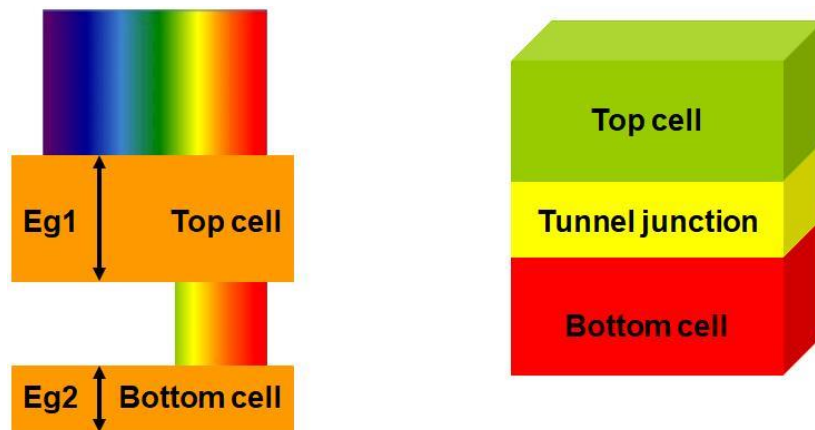


Figure 4-6 Schéma du diagramme et de la structure de la bande de cellules solaires tandem.

La figure 4-6 présente le schéma de cellule et de structure de la cellule solaire tandem. La cellule solaire tandem est composée de trois parties: cellule supérieure cell cellule inférieure et jonction tunnel. Pour notre structure de cellules solaires tandem, GaAs<sub>0.09</sub>P<sub>0.87</sub>N<sub>0.04</sub>, ci-après GaAsPN et Si sont appliqués aux matériaux absorbant les cellules supérieures et inférieures. Il est basé sur les raisons suivantes:

Premièrement, le plus important est le substrat Si, beaucoup moins coûteux, comparé à GaAs, Ge ou à d'autres substrats traditionnels.

La figure 4-7 montre que ces sous-cellules doivent avoir une correspondance parfaite du courant et une efficacité théorique élevée.

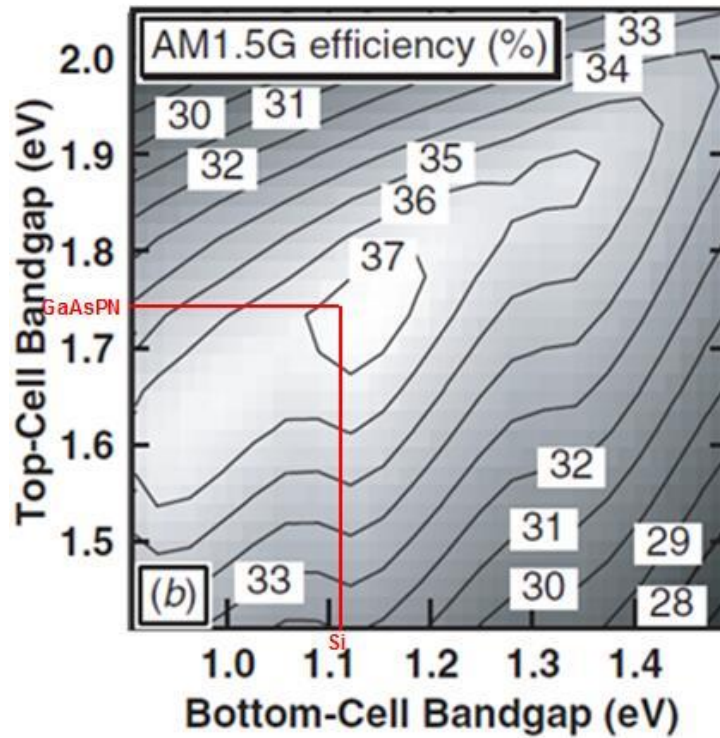


Figure 4-7: Efficacité théorique de la cellule solaire tandem en fonction des bandes interdites des cellules supérieures et inférieures utilisant le spectre global standard AM1.5. Les lignes rouges qui se croisent représentent l'efficacité de la cellule solaire tandem GaAsPN / Si. D'après la figure, la valeur d'efficacité de la cellule solaire en tandem tombe dans le cercle le plus élevé, soit 37%.

Comme le montre la figure 4-8, GaAsPN présente une bonne correspondance de réseau avec Si. Cela réduit les défauts: densité de dislocation par filetage, les microtwins, les failles d'empilement et les domaines d'antiphases qui sont induits par un désadaptation des réseaux et réduisent considérablement les performances des cellules solaires.

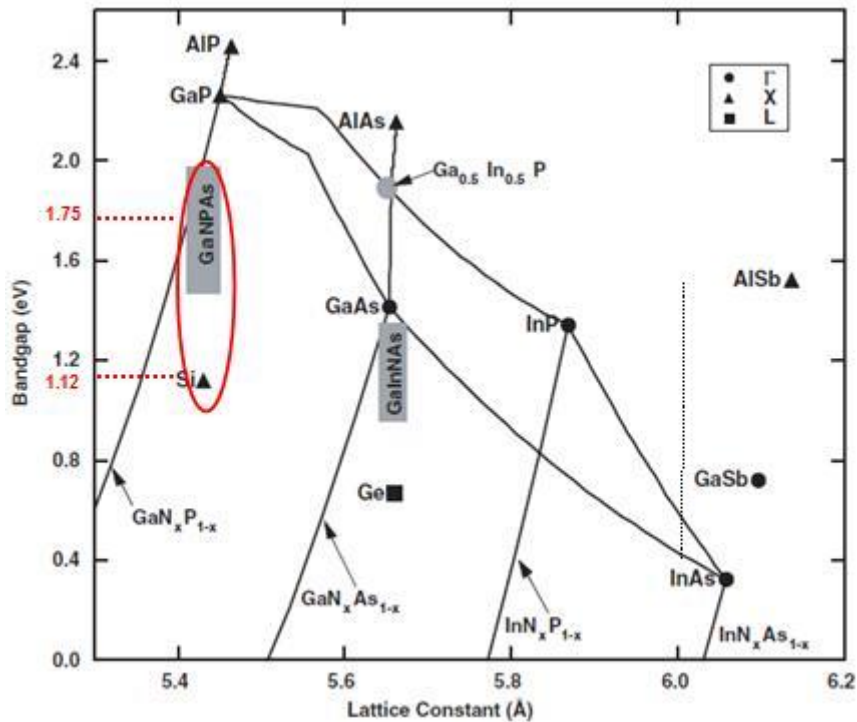


Figure 4-8: Matériaux semi-conducteurs et constante de réseau. Comme le cercle rouge le souligne, la constante de réseau de GaAsPN est presque identique à la constante de réseau de Si. Cela signifie que le mauvais effet induit par le désaccord du réseau sur les performances des cellules solaires est faible.

## 4.2 Outil de simulation numérique de cellules solaires

SILVACO est utilisé pour simuler et analyser des cellules solaires. Avec cet outil, des simulations numériques 1D ou 2D peuvent être effectuées. Paramètres de structure: Épaisseur des couches / Niveaux / types de dopage et paramètres de matériau: Bandgap / Mobilités des porteurs / Affinités / Durée de vie / n.k (où n est l'indice de réfraction, k est le coefficient d'extinction), peuvent être entrés. Ensuite, le logiciel résout les trois équations précédentes, après quoi de nombreux paramètres peuvent être générés, tels que I-V (sombre et sous illumination) / Efficacité quantique / Bande de conduction / Bande de Valence / Concentrations de porteurs / Pièges /.

### 4.3 Influence de l'épaisseur de la couche absorbante de GaAsPN

Les résultats de la simulation montrent que la plage d'épaisseur optimale de la couche active (GaAsPN) est d'environ 1 à 1,5  $\mu\text{m}$ , ce qui correspond à: Eff 10,7%;  $V_{oc} \approx 1 \text{ V}$ ;  $J_{sc} \approx 20 \text{ mA} / \text{cm}^2$  peut être obtenu.

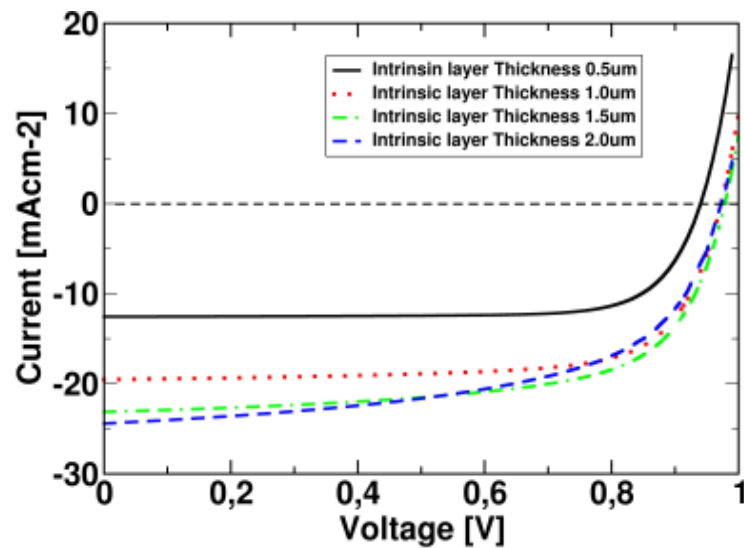


Figure 4-12: Caractéristiques courant-tension: résultats de simulation pour différentes épaisseurs de GaAsPN.

### 4.5 Influence du décalage de bande

La barrière en bande de conduction atteint 0,45 eV à l'interface formée de GaAsPN et de GaP de type n avec des bandes interdites de 1,75 eV et 2,2eV séparément. Cette barrière élevée devrait réduire le transport d'électrons dans la bande de conduction.

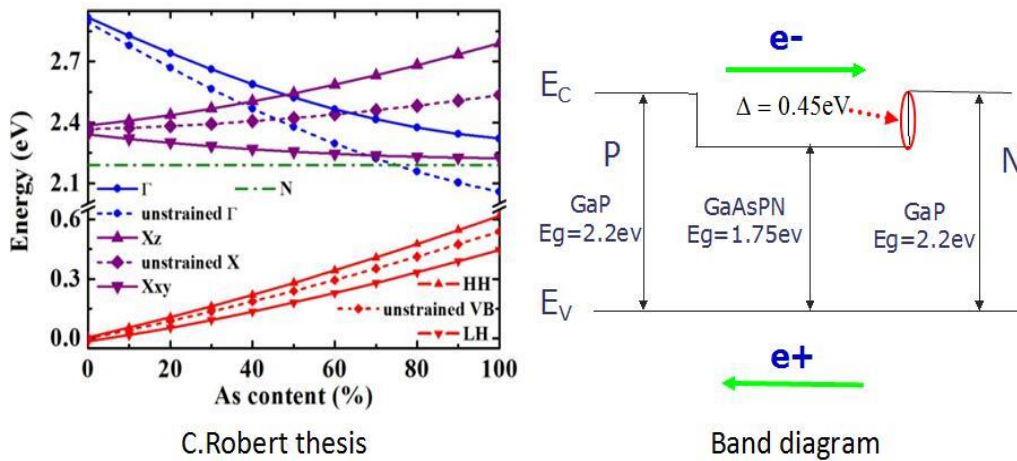


Figure 4-13: Résultats de la simulation C.Robert et diagramme de la bande de jonction supérieure (figure de gauche: bandes de conduction et de valence GaAsPN à très faible teneur en N en fonction du contenu As). Figure de droite: notre diagramme de bande de jonction supérieure).

Ainsi, deux couches différentes de styles sont placées entre la couche active GaAsPN et la couche inférieure de GaP. Pour le premier type de couches graduées, chaque couche a un intervalle de bande interdite de 0,1 eV, l'autre type de couches dégradées. La seconde, chaque couche a une différence de 0,025 eV entre chaque bande interdite.

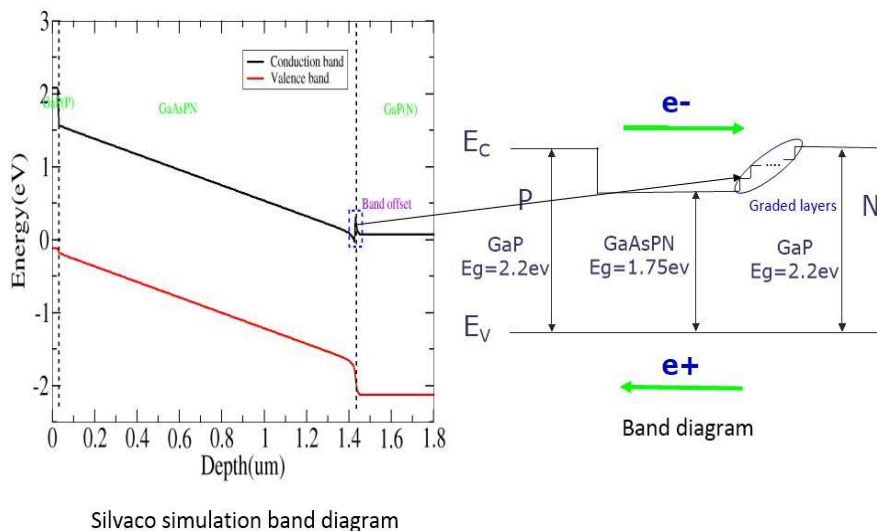


Figure 4-14: Diagrammes de bandes issus de la théorie et de la simulation Silvaco.

La Figure 4.15 montre que les priorités des jonctions avec des couches graduées sont supérieures aux priorités de la jonction abrupte d'origine. Pendant ce temps, lors

de ces jonctions avec des couches graduées, plus le pas de la bande est petit, meilleures sont les performances du dispositif.

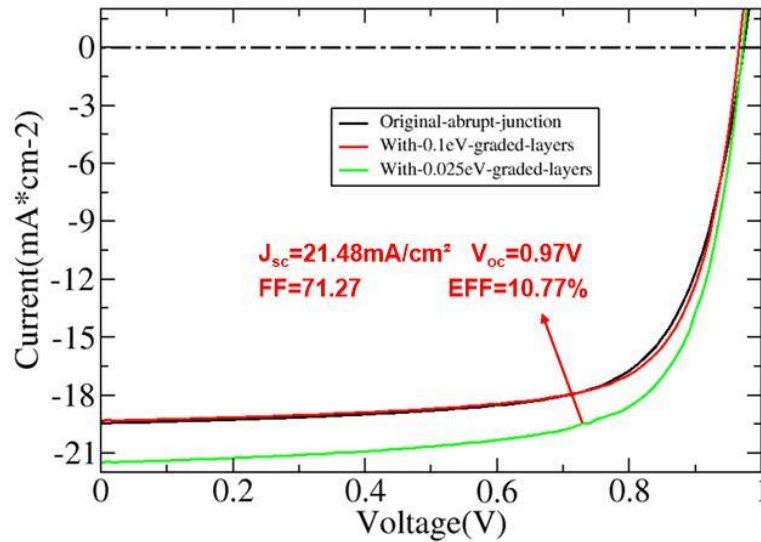


Figure 4-15: Résultats de la simulation avec et sans couches graduées.

## 4.6 Etude d'EQE de cellules supérieures

L'efficacité quantique externe est l'un des paramètres importants permettant d'évaluer les performances des dispositifs à cellules solaires. Elle est égale à la proportion du nombre de porteurs de charge collectés par rapport au nombre de photons incidents.

$$EQE_{(\lambda)} = \frac{\text{Collected charge carriers number}}{\text{Incident photons number}}$$

Dans deux cas intéressants, lorsque l'affinité est égale à 3,8 eV et à 4,3 eV, il n'y a pas de barrière entre la bande de conduction et la bande de valence séparément, comme le montre la Figure 4-19.

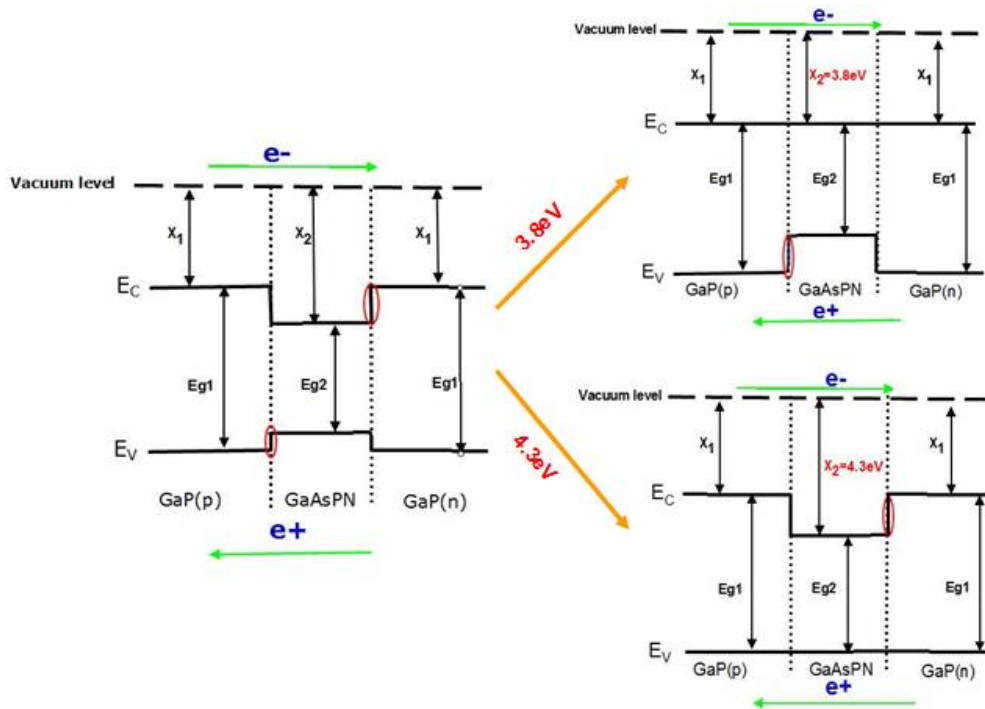


Figure 4-19: Diagramme de la bande d'énergie théorique de la cellule du haut, où l'affinité ( $\chi_1, \chi_2$ ) est une bande interdite ( $E_{g1}, E_{g2}$ ). En haut à droite, l'affinité avec le diagramme de bande d'énergie de 3.8 eV; La droite en dessous de l'un est le diagramme d'affinité avec une bande d'énergie de 4.3 eV; Les cercles rouges sont décalés.

La Figure 4-20 affiche les résultats de la simulation. Cependant, dans ces deux cas, ils ont les mêmes valeurs de décalage de bande existant respectivement dans la bande de valence et dans la bande de conduction, comme illustré à la Figure 4-19. Nous pouvons conclure que l'effet de barrière de bande de conduction sur le transport des transporteurs est plus important que l'effet de barrière de bande de valence.

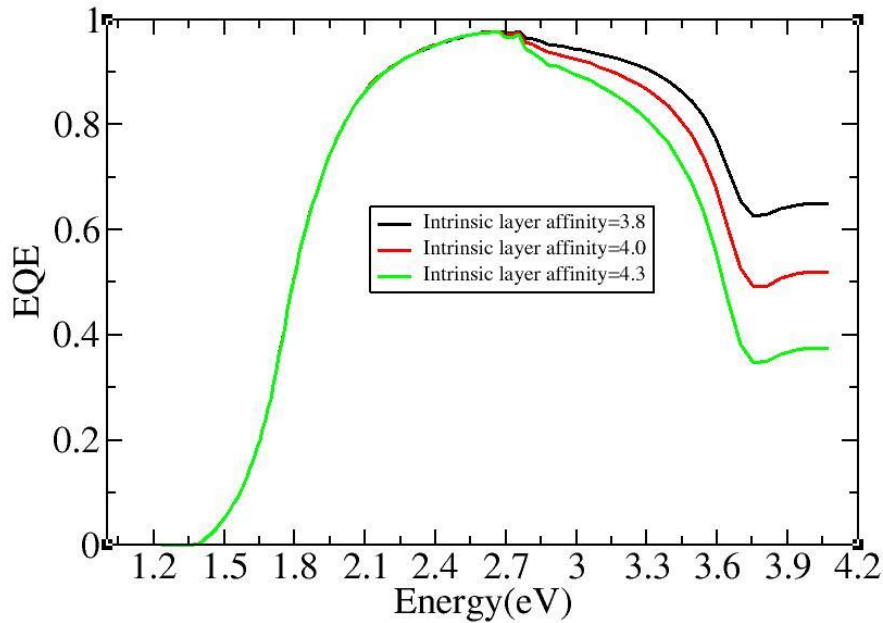


Figure 4-20: Résultats de la simulation EQE de cellules supérieures avec différentes affinités de couche active.

Lorsque l'énergie des photons dépasse 2.7 eV, la différence EQE de ces trois dispositifs apparaît.

## 4.7 Etude de jonction tunnel

Considérant les matériaux que nous avons utilisés pour les cellules solaires tandem, nous simulons les quatre types de jonctions tunnel potentiels suivants: GaP (n++) / GaP (p++), Si (n++) / Si (p++), GaP (n++) / Si (p++) , GaP (p++) / Si (n++).

D'après la description du tableau 4-5, GaP (n++) / Si (p++), Si (n++) / Si (p++) présentent de meilleurs résultats que les deux autres jonctions tunnel, et pour le meilleur GaP (n++) / Si (p++) ) La jonction tunnel, illustrée à la Figure 4-24, présente l'épaisseur de barrière la plus étroite qui rend le transport des porteurs plus efficace que les structures de gauche, ainsi que la densité de courant de pointe la plus élevée. Nous avons donc finalement choisi GaP (n++) / Si (p++) comme structure de jonction tunnel.

Tableau 4-5: Densités des courants de crête des jonctions de tunnels.

Densité de courant maximale  $I_p$ , épaisseur de la barrière  $L_B$

	GaP(n++)/Si(p++)	GaP(p++)/Si(n++)	GaP(n++)/GaP(p++)	Si(n++)/Si(p++)
$I_p(\text{mA}/\text{cm}^2)$	$8.4 \times 10^8$	$\sim 10^{-4}$	$\sim 10^{-3}$	$3.4 \times 10^5$
$L_B(\text{nm})$	3.3	6.9	5.9	4.4

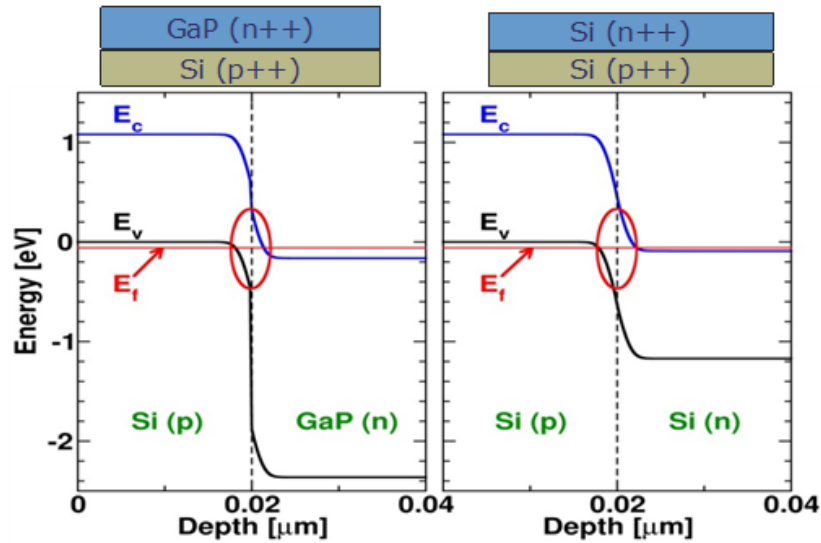


Figure 4-24: Résultats simulés des jonctions tunnel GaP (n++) / Si (p++), Si (n++) / Si (p++). La bande de valence Si (p++) est considérée comme référence d'énergie. Où  $E_c$ ,  $E_v$  sont une bande de conduction et une bande de valence,  $E_f$  est le niveau de Fermi.

## 4.8 Simulation de cellules solaires en tandem et ajustement des résultats expérimentaux

Sur la base de toutes les études précédentes, la cellule solaire tandem est simulée afin d'adapter les résultats de l'expérimentation. Comme le montre la figure 4-27, le résultat de la simulation est proche du résultat de l'expérience, mais ne cadre pas très bien. Il faut mentionner de nombreux éléments. En outre, une meilleure et plus précise simulation de simulation devrait être faite et obtenue.

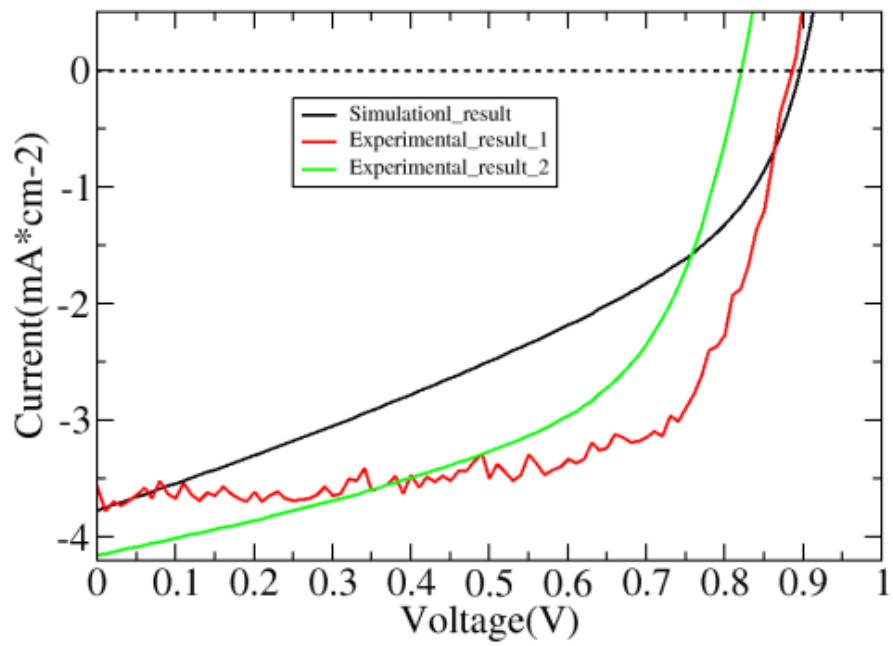


Figure 4-27: Ajustement des résultats expérimentaux (les lignes rouge et verte représentent les courbes I-V des expériences 1 et 2, les lignes noires correspondent aux courbes I-V simulées basées sur les mêmes paramètres de structure).

## Reference

1. Sanz, J.; Ortiz, D.; Alcaraz De La Osa, R.; Saiz, J.; González, F.; Brown, A.; Losurdo, M.; Everitt, H.; Moreno, F. *The Journal of Physical Chemistry C* **2013**, 117, (38), 19606-19615.
2. Truong, P. L.; Ma, X.; Sim, S. J. *Nanoscale* **2014**, 6, (4), 2307-2315.
3. Verma, S.; Sekhon, J. S. *Journal of Optics* **2012**, 41, (2), 89-93.
4. Haber, J.; Gascoyne, P.; Sokolov, K. *Lab on a Chip* **2017**, 17, (16), 2821-2830.
5. Funari, R.; Bhalla, N.; Chu, K.-Y.; Soderstrom, B.; Shen, A. Q. *ACS sensors* **2018**, 3, (8), 1499-1509.
6. Acímović, S. S.; Šípová, H.; Emilsson, G.; Dahlin, A. B.; Antosiewicz, T. J.; Käll, M. *Light: Science & Applications* **2017**, 6, (8), e17042.
7. Lagos, L. K.; Veliz, L.; Hernandez, Y.; Galarreta, B. C. In *Label-free SERS and LSPR gold nanoaptasensors of mycotoxins in solution: solvent assessment*, Latin America Optics and Photonics Conference, 2018; Optical Society of America: p Tu2C. 2.
8. Khansili, N.; Rattu, G.; Krishna, P. M. *Sensors and Actuators B: Chemical* **2018**, 265, 35-49.
9. Lu, X.; Rycenga, M.; Skrabalak, S. E.; Wiley, B.; Xia, Y. *Annual review of physical chemistry* **2009**, 60, 167-192.
10. Zayats, A. V.; Smolyaninov, I. I. *Journal of Optics A: Pure and Applied Optics* **2003**, 5, (4), S16.
11. Kretschmann, E.; Raether, H. *Zeitschrift für Naturforschung A* **1968**, 23, (12), 2135-2136.
12. Otto, A. *Zeitschrift für Physik A Hadrons and nuclei* **1968**, 216, (4), 398-410.
13. Park, S.; Lee, G.; Song, S. H.; Oh, C. H.; Kim, P. S. *Optics letters* **2003**, 28, (20), 1870-1872.
14. Hecht, B.; Bielefeldt, H.; Novotny, L.; Inouye, Y.; Pohl, D. *Physical review letters* **1996**, 77, (9), 1889.
15. Maier, S. A., *Plasmonics: fundamentals and applications*. Springer Science & Business Media: 2007.
16. Mie, G. *Annalen der physik* **1908**, 330, (3), 377-445.
17. Kerker, M., *The scattering of light and other electromagnetic radiation*. Elsevier: 2016.
18. Bohren, C. F.; Huffman, D. R. *Light by Small Particles* **1983**, 209.
19. Link, S.; El-Sayed, M. A., Spectral properties and relaxation dynamics of surface plasmon electronic oscillations in gold and silver nanodots and nanorods. ACS Publications: 1999.
20. Das, P.; Chini, T. K.; Pond, J. *The Journal of Physical Chemistry C* **2012**, 116, (29), 15610-15619.
21. Brioude, A.; Jiang, X.; Pileni, M. *The Journal of Physical Chemistry B* **2005**, 109, (27), 13138-13142.
22. Moreno, E.; Erni, D.; Hafner, C.; Vahldieck, R. *JOSA A* **2002**, 19, (1), 101-111.
23. Zhao, L.; Kelly, K. L.; Schatz, G. C. *The Journal of Physical Chemistry B* **2003**, 107, (30), 7343-7350.
24. Dahmen, C.; Schmidt, B.; von Plessen, G. *Nano letters* **2007**, 7, (2), 318-322.
25. Teperik, T.; Popov, V.; de Abajo, F. G. *Physical Review B* **2004**, 69, (15), 155402.
26. Sönnichsen, C.; Franzl, T.; Wilk, T.; von Plessen, G.; Feldmann, J.; Wilson, O.; Mulvaney, P. *Physical review letters* **2002**, 88, (7), 077402.
27. Lermé, J.; Baida, H.; Bonnet, C.; Broyer, M.; Cottancin, E.; Crut, A.; Maioli, P.; Del Fatti, N.; Vallée, F.; Pellarin, M. *The Journal of Physical Chemistry Letters* **2010**, 1, (19), 2922-2928.

28. Meier, M.; Wokaun, A. *Optics letters* **1983**, 8, (11), 581-583.
29. Tamm, K. *Berichte der Bunsengesellschaft für physikalische Chemie* **1980**, 84, (11), 1190-1191.
30. Safarov, V.; Kosobukin, V.; Hermann, C.; Lampel, G.; Peretti, J.; Marliere, C. *Physical review letters* **1994**, 73, (26), 3584.
31. Hermann, C.; Kosobukin, V.; Lampel, G.; Peretti, J.; Safarov, V.; Bertrand, P. *Physical Review B* **2001**, 64, (23), 235422.
32. González-Díaz, J.; García-Martín, A.; Armelles, G.; García-Martín, J.; Clavero, C.; Cebollada, A.; Lukaszew, R.; Skuza, J.; Kumah, D.; Clarke, R. *Physical Review B* **2007**, 76, (15), 153402.
33. Clavero, C.; Yang, K.; Skuza, J.; Lukaszew, R. *Optics express* **2010**, 18, (8), 7743-7752.
34. Clavero, C.; Yang, K.; Skuza, J.; Lukaszew, R. *Optics letters* **2010**, 35, (10), 1557-1559.
35. Liz-Marzán, L. M. *Langmuir* **2006**, 22, (1), 32-41.
36. Brockman, J. M.; Nelson, B. P.; Corn, R. M. *Annual review of physical chemistry* **2000**, 51, (1), 41-63.
37. Nath, N.; Chilkoti, A. *Analytical chemistry* **2002**, 74, (3), 504-509.
38. Sun, Y.; Xia, Y. *Analytical Chemistry* **2002**, 74, (20), 5297-5305.
39. Thanh, N. T. K.; Rosenzweig, Z. *Analytical chemistry* **2002**, 74, (7), 1624-1628.
40. Aizpurua, J.; Bryant, G. W.; Richter, L. J.; De Abajo, F. G.; Kelley, B. K.; Mallouk, T. *Physical Review B* **2005**, 71, (23), 235420.
41. Kelly, K. L.; Coronado, E.; Zhao, L. L.; Schatz, G. C., The optical properties of metal nanoparticles: the influence of size, shape, and dielectric environment. ACS Publications: 2003.
42. Jain, P. K.; Lee, K. S.; El-Sayed, I. H.; El-Sayed, M. A. *The journal of physical chemistry B* **2006**, 110, (14), 7238-7248.
43. McFarland, A. D.; Van Duyne, R. P. *Nano letters* **2003**, 3, (8), 1057-1062.
44. Schmid, G., *Clusters and colloids: from theory to applications*. Wiley Online Library: 1994; Vol. 112.
45. Jensen, T. R.; Malinsky, M. D.; Haynes, C. L.; Van Duyne, R. P. *The Journal of Physical Chemistry B* **2000**, 104, (45), 10549-10556.
46. Jensen, T. R.; Duval, M. L.; Kelly, K. L.; Lazarides, A. A.; Schatz, G. C.; Van Duyne, R. P. *The Journal of Physical Chemistry B* **1999**, 103, (45), 9846-9853.
47. Sepúlveda, B.; Angelomé, P. C.; Lechuga, L. M.; Liz-Marzán, L. M. *nano today* **2009**, 4, (3), 244-251.
48. Lee, S. J.; Guan, Z.; Xu, H.; Moskovits, M. *The Journal of Physical Chemistry C* **2007**, 111, (49), 17985-17988.
49. Lamprecht, B.; Schider, G.; Lechner, R.; Ditlbacher, H.; Krenn, J.; Leitner, A.; Aussenegg, F. *Physical review letters* **2000**, 84, (20), 4721.
50. Jensen, T. R.; Schatz, G. C.; Van Duyne, R. P. *The Journal of Physical Chemistry B* **1999**, 103, (13), 2394-2401.
51. Duval Malinsky, M.; Kelly, K. L.; Schatz, G. C.; Van Duyne, R. P. *The Journal of Physical Chemistry B* **2001**, 105, (12), 2343-2350.
52. Pinchuk, A.; Hilger, A.; von Plessen, G.; Kreibig, U. *Nanotechnology* **2004**, 15, (12), 1890.
53. Sherry, L. J.; Chang, S.-H.; Schatz, G. C.; Van Duyne, R. P.; Wiley, B. J.; Xia, Y. *Nano letters* **2005**, 5, (10), 2034-2038.

54. Gramotnev, D. K.; Bozhevolnyi, S. I. *Nature photonics* **2010**, 4, (2), 83.
55. Storhoff, J. J.; Elghanian, R.; Mucic, R. C.; Mirkin, C. A.; Letsinger, R. L. *Journal of the American Chemical Society* **1998**, 120, (9), 1959-1964.
56. Elghanian, R.; Storhoff, J. J.; Mucic, R. C.; Letsinger, R. L.; Mirkin, C. A. *Science* **1997**, 277, (5329), 1078-1081.
57. Mirkin, C. A.; Letsinger, R. L.; Mucic, R. C.; Storhoff, J. J. *Nature* **1996**, 382, (6592), 607.
58. Atwater, H. A.; Polman, A. *Nature materials* **2010**, 9, (3), 205.
59. Menezes, J. W.; Ferreira, J.; Santos, M. J.; Cescato, L.; Brolo, A. G. *Advanced Functional Materials* **2010**, 20, (22), 3918-3924.
60. Brolo, A. G. *Nature Photonics* **2012**, 6, (11), 709.
61. Pan, G.; Kesavamoorthy, R.; Asher, S. A. *Journal of the American Chemical Society* **1998**, 120, (26), 6525-6530.
62. Weissman, J. M.; Sunkara, H. B.; Albert, S. T.; Asher, S. A. *Science* **1996**, 274, (5289), 959-963.
63. Camden, J. P.; Dieringer, J. A.; Wang, Y.; Masiello, D. J.; Marks, L. D.; Schatz, G. C.; Van Duyne, R. P. *Journal of the American Chemical Society* **2008**, 130, (38), 12616-12617.
64. Le Ru, E.; Blackie, E.; Meyer, M.; Etchegoin, P. G. *The Journal of Physical Chemistry C* **2007**, 111, (37), 13794-13803.
65. Chapin, D. M.; Fuller, C.; Pearson, G. *Journal of Applied Physics* **1954**, 25, (5), 676-677.
66. Green, M. A. *Physica E: Low-dimensional Systems and Nanostructures* **2002**, 14, (1-2), 65-70.
67. Green, M. A. **1982**.
68. Yablonovitch, E.; Cody, G. D. *IEEE Transactions on Electron Devices* **1982**, 29, (2), 300-305.
69. Deckman, H.; Roxlo, C.; Yablonovitch, E. *Optics letters* **1983**, 8, (9), 491-493.
70. Rand, B. P.; Peumans, P.; Forrest, S. R. *Journal of Applied Physics* **2004**, 96, (12), 7519-7526.
71. Catchpole, K.; Polman, A. *Applied Physics Letters* **2008**, 93, (19), 191113.
72. Pillai, S.; Catchpole, K.; Trupke, T.; Zhang, G.; Zhao, J.; Green, M. *Applied Physics Letters* **2006**, 88, (16), 161102.
73. Fujimori, S.; Dinyari, R.; Lee, J.; Peumans, P. *Nano Lett* **2009**.
74. Mertz, J. *JOSA B* **2000**, 17, (11), 1906-1913.
75. Borisov, S. M.; Wolfbeis, O. S. *Chemical reviews* **2008**, 108, (2), 423-461.
76. Pickup, J. C.; Hussain, F.; Evans, N. D.; Rolinski, O. J.; Birch, D. J. *Biosensors and Bioelectronics* **2005**, 20, (12), 2555-2565.
77. Homola, J. *Analytical and bioanalytical chemistry* **2003**, 377, (3), 528-539.
78. Yakovleva, J.; Davidsson, R.; Bengtsson, M.; Laurell, T.; Emnéus, J. *Biosensors and Bioelectronics* **2003**, 19, (1), 21-34.
79. Kabashin, A.; Evans, P.; Pastkovsky, S.; Hendren, W.; Wurtz, G.; Atkinson, R.; Pollard, R.; Podolskiy, V.; Zayats, A. *Nature materials* **2009**, 8, (11), 867.
80. Xu, X.; Han, M. S.; Mirkin, C. A. *Angewandte Chemie* **2007**, 119, (19), 3538-3540.
81. Marinakos, S. M.; Chen, S.; Chilkoti, A. *Analytical chemistry* **2007**, 79, (14), 5278-5283.
82. Murphy, C. J.; Sau, T. K.; Gole, A. M.; Orendorff, C. J.; Gao, J.; Gou, L.; Hunyadi, S. E.; Li, T., Anisotropic metal nanoparticles: synthesis, assembly, and optical applications. ACS Publications: 2005.
83. McNay, G.; Eustace, D.; Smith, W. E.; Faulds, K.; Graham, D. *Applied spectroscopy* **2011**, 65, (8), 825-837.

84. Cialla, D.; März, A.; Böhme, R.; Theil, F.; Weber, K.; Schmitt, M.; Popp, J. *Analytical and bioanalytical chemistry* **2012**, 403, (1), 27-54.
85. Sharma, B.; Frontiera, R. R.; Henry, A.-I.; Ringe, E.; Van Duyne, R. P. *Materials today* **2012**, 15, (1-2), 16-25.
86. Bantz, K. C.; Meyer, A. F.; Wittenberg, N. J.; Im, H.; Kurtuluş, Ö.; Lee, S. H.; Lindquist, N. C.; Oh, S.-H.; Haynes, C. L. *Physical Chemistry Chemical Physics* **2011**, 13, (24), 11551-11567.
87. Raman, C. V.; Krishnan, K. S. *Nature* **1928**, 121, (3048), 501.
88. Fleischmann, M.; Hendra, P. J.; McQuillan, A. J. *Chemical Physics Letters* **1974**, 26, (2), 163-166.
89. Jeanmaire, D. L.; Van Duyne, R. P. *Journal of electroanalytical chemistry and interfacial electrochemistry* **1977**, 84, (1), 1-20.
90. Zeman, E.; Carron, K.; Schatz, G.; Van Duyne, R. *The Journal of chemical physics* **1987**, 87, (7), 4189-4200.
91. Lombardi, J. R.; Birke, R. L.; Lu, T.; Xu, J. *The Journal of chemical physics* **1986**, 84, (8), 4174-4180.
92. Moskovits, M. *The Journal of Chemical Physics* **1982**, 77, (9), 4408-4416.
93. Hadjar, Y.; Renault, M.; Blaize, S.; Bruyant, A.; Vincent, R.; Hmima, A. *JOSA A* **2015**, 32, (5), 771-777.
94. Sherry, L. J.; Jin, R.; Mirkin, C. A.; Schatz, G. C.; Van Duyne, R. P. *Nano letters* **2006**, 6, (9), 2060-2065.
95. Zhang, J.; Liu, H.; Wang, Z.; Ming, N. *Applied physics letters* **2007**, 90, (16), 163122.
96. Lindquist, N. C.; Johnson, T. W.; Nagpal, P.; Norris, D. J.; Oh, S.-H. *Scientific reports* **2013**, 3, 1857.
97. Bozhevolnyi, S. I.; Volkov, V. S.; Devaux, E.; Ebbesen, T. W. *Physical review letters* **2005**, 95, (4), 046802.
98. Johnson, T. W.; Lapin, Z. J.; Beams, R.; Lindquist, N. C.; Rodrigo, S. G.; Novotny, L.; Oh, S.-H. *ACS nano* **2012**, 6, (10), 9168-9174.
99. Pillai, S.; Catchpole, K.; Trupke, T.; Green, M. *Journal of applied physics* **2007**, 101, (9), 093105.
100. Novikov, I.; Maradudin, A. *Physical Review B* **2002**, 66, (3), 035403.
101. PRASAD, R. Device integration of the CoBiSS spectrometer, and modelisation of (L)SPR chip for detection through CoBiSS. August 22, 2017.
102. Shuai, Y.; Wu, C. G.; Zhang, W. L.; Li, Y. R.; Liu, X. Z.; Zhu, J. In *Optimization of (100)-Si TMAH etching for uncooled infrared detector*, International Symposium on Photoelectronic Detection and Imaging 2009, 2009, Beijing, China, 2009.
103. Lee, M. H.; Lin, J. Y.; Odom, T. W. *Angewandte Chemie* **2010**, 122, (17), 3121-3124.
104. Pryce, I. M.; Aydin, K.; Kelaita, Y. A.; Briggs, R. M.; Atwater, H. A. *Nano letters* **2010**, 10, (10), 4222-4227.
105. Lee, K. J.; Fosser, K. A.; Nuzzo, R. G. *Advanced Functional Materials* **2005**, 15, (4), 557-566.
106. Bowen, A. M.; Nuzzo, R. G. *Advanced Functional Materials* **2009**, 19, (20), 3243-3253.
107. Atmaja, B.; Frommer, J.; Scott, J. C. *Langmuir* **2006**, 22, (10), 4734-4740.
108. Popov, E.; Loewen, E. G., *Diffraction gratings and applications*. Marcel Dekker, New York: 1997.
109. Popov, E., *GratinGs: theory and numeric applications*. Popov, Institut Fresnel: 2012.
110. Maystre, D.; Neviere, M.; Petit, R., *Electromagnetic Theory of Gratings*. In *Topics in Current*

- Physics*, Springer-Verlag Berlin: 1980; Vol. 22, p 98.
111. Maystre, D., I Rigorous Vector Theories of Diffraction Gratings. In *Progress in optics*, Elsevier: 1984; Vol. 21, pp 1-67.
  112. Arnaud, L. Diffraction et diffusion de la lumière: modélisation tridimensionnelle et application à la métrologie de la microélectronique et aux techniques d'imagerie sélective en milieu diffusant. Aix-Marseille 3, 2008.
  113. Nevrière, M.; Popov, E., *Light propagation in periodic media: differential theory and design*. CRC Press: 2002.
  114. Li, L. *JOSA A* **1996**, 13, (5), 1024-1035.
  115. Popov, E.; Nevrière, M. *JOSA A* **2000**, 17, (10), 1773-1784.
  116. Li, L. *JOSA A* **1996**, 13, (9), 1870-1876.
  117. Chandezon, J.; Raoult, G.; Maystre, D. *Journal of Optics* **1980**, 11, (4), 235.
  118. Chandezon, J.; Dupuis, M.; Cornet, G.; Maystre, D. *JOSA* **1982**, 72, (7), 839-846.
  119. Popov, E.; Mashev, L. *Journal of optics* **1986**, 17, (4), 175.
  120. Elston, S.; Bryan-Brown, G.; Sambles, J. *Physical Review B* **1991**, 44, (12), 6393.
  121. Li, L. *JOSA A* **1994**, 11, (11), 2816-2828.
  122. Popov, E.; Nevriere, M. *JOSA B* **1994**, 11, (9), 1555-1564.
  123. Granet, G.; Chandezon, J.; Coudert, O. *JOSA A* **1997**, 14, (7), 1576-1582.
  124. Li, L.; Chandezon, J.; Granet, G.; Plumey, J.-P. *Applied Optics* **1999**, 38, (2), 304-313.
  125. <https://mcgrating.com/>.
  126. Oliverio, M.; Perotto, S.; Messina, G. C.; Lovato, L.; De Angelis, F. *ACS applied materials & interfaces* **2017**, 9, (35), 29394-29411.
  127. Raether, H., Surface plasmons on gratings. In *Surface plasmons on smooth and rough surfaces and on gratings*, Springer: 1988; pp 91-116.
  128. Tellez-Limon, R.; Fevrier, M.; Apuzzo, A.; Salas-Montiel, R.; Blaize, S. *Photonics Research* **2014**, 2, (1), 24-30.
  129. Vincent., R. P. Electronic excitations, energy loss and electron emission in the interaction of charged particles with metallic materials and plasmon modes localized at surface singularities. 2009.
  130. R. Vincent, J. J., and P. Apell. *arXiv:1103.2086* **2011**.
  131. Yakubovsky, D. I.; Arsenin, A. V.; Stebunov, Y. V.; Fedyanin, D. Y.; Volkov, V. S. *Optics express* **2017**, 25, (21), 25574-25587.
  132. <https://pveducation.org/>
  133. Archer, M. D.; Green, M. A., *Clean electricity from photovoltaics*. Imperial College Press: 2001.
  134. Goetzberger, A.; Hebling, C. *Solar energy materials and solar cells* **2000**, 62, (1-2), 1-19.
  135. <https://www.nrel.gov/pv/assets/pdfs/pv-efficiency-chart.20181221.pdf>.
  136. Yamane, K.; Sato, K.; Sekiguchi, H.; Okada, H.; Wakahara, A. *Journal of Crystal Growth* **2017**, 473, 55-59.
  137. Deshpande, V.; Djara, V.; O'Connor, E.; Hashemi, P.; Morf, T.; Balakrishnan, K.; Caimi, D.; Sousa, M.; Fompeyrine, J.; Czornomaz, L. *Japanese Journal of Applied Physics* **2017**, 56, (4S), 04CA05.
  138. Robert, C.; Bondi, A.; Thanh, T. N.; Even, J.; Cornet, C.; Durand, O.; Burin, J.-P.; Jancu, J.-M.; Guo, W.; Létoublon, A. *Applied Physics Letters* **2011**, 98, (25), 251110.
  139. Almosni, S.; Robert, C.; Nguyen Thanh, T.; Cornet, C.; Létoublon, A.; Quinci, T.; Levallois, C.;

- Perrin, M.; Kuyyalil, J.; Pedesseau, L. *Journal of applied physics* **2013**, 113, (12), 123509.
140. Hsieh, M.-H.; Wu, Y.-R. In *Numerical modeling of In x Ga 1– x n silicon multi-junction tandem solar cell*, Photovoltaic Specialists Conference (PVSC), 2012 38th IEEE, 2012; IEEE: pp 002052-002055.
141. Geisz, J.; Friedman, D. *Semiconductor Science and Technology* **2002**, 17, (8), 769.
142. Kojima, A.; Teshima, K.; Shirai, Y.; Miyasaka, T. *Journal of the American Chemical Society* **2009**, 131, (17), 6050-6051.
143. <https://www.pveurope.eu/News/Solar-Generator/New-record-for-perovskite-silicon-tandem-solar-cell>.
144. Razza, S.; Castro-Hermosa, S.; Di Carlo, A.; Brown, T. M. *APL Materials* **2016**, 4, (9), 091508.
145. [http://www.solar-frontier.com/eng/news/2017/1220\\_press.html](http://www.solar-frontier.com/eng/news/2017/1220_press.html).
146. Kazmerski, L.; White, F.; Morgan, G. *Applied Physics Letters* **1976**, 29, (4), 268-270.
147. Wang, Y.-C.; Shieh, H.-P. D. *Applied Physics Letters* **2014**, 105, (7), 073901.
148. Powalla, M.; Dimmler, B. *Thin Solid Films* **2000**, 361, 540-546.
149. Green, M. A.; Hishikawa, Y.; Dunlop, E. D.; Levi, D. H.; Hohl- Ebinger, J.; Yoshita, M.; Ho-Baillie, A. W. *Progress in Photovoltaics: Research and Applications* **2019**, 27, (1), 3-12.
150. Shockley, W.; Queisser, H. J. *Journal of applied physics* **1961**, 32, (3), 510-519.
151. Verlinden, P.; Swanson, R.; Crane, R. *Progress in Photovoltaics: Research and Applications* **1994**, 2, (2), 143-152.
152. Taguchi, M. *proc. of Fifth PVSEC, 1990, Florida* **1990**.
153. Mishima, T.; Taguchi, M.; Sakata, H.; Maruyama, E. *Solar Energy Materials and Solar Cells* **2011**, 95, (1), 18-21.
154. Hoex, B.; Schmidt, J.; Pohl, P.; Van de Sanden, M.; Kessels, W. *Journal of Applied Physics* **2008**, 104, (4), 044903.
155. Hoex, B.; Gielis, J.; Van de Sanden, M.; Kessels, W. *Journal of Applied Physics* **2008**, 104, (11), 113703.
156. You, J.; Dou, L.; Yoshimura, K.; Kato, T.; Ohya, K.; Moriarty, T.; Emery, K.; Chen, C.-C.; Gao, J.; Li, G. *Nature communications* **2013**, 4, 1446.
157. Bush, K. A.; Palmstrom, A. F.; Zhengshan, J. Y.; Boccard, M.; Checharoen, R.; Mailoa, J. P.; McMeekin, D. P.; Hoyer, R. L.; Bailie, C. D.; Leijtens, T. *Nature Energy* **2017**, 2, (4), 17009.
158. Rolland, A.; Pedesseau, L.; Kepenekian, M.; Katan, C.; Huang, Y.; Wang, S.; Cornet, C.; Durand, O.; Even, J. *Optical and Quantum Electronics* **2018**, 50, (1), 21.
159. Rolland, A.; Pedesseau, L.; Even, J.; Almosni, S.; Robert, C.; Cornet, C.; Jancu, J. M.; Benhlal, J.; Durand, O.; Le Corre, A. *Optical and Quantum Electronics* **2014**, 46, (10), 1397-1403.
160. Geisz, J.; Olson, J.; Friedman, D.; Jones, K.; Reedy, R.; Romero, M. In *Lattice-matched GaNPAs-on-silicon tandem solar cells*, Photovoltaic Specialists Conference, 2005. Conference Record of the Thirty-first IEEE, 2005; IEEE: pp 695-698.
161. Grassman, T. J.; Brenner, M. R.; Gonzalez, M.; Carlin, A. M.; Unocic, R. R.; Dehoff, R. R.; Mills, M. J.; Ringel, S. A. *IEEE Transactions on Electron Devices* **2010**, 57, (12), 3361-3369.
162. King, R.; Bhusari, D.; Boca, A.; Larrabee, D.; Liu, X. Q.; Hong, W.; Fetzer, C.; Law, D.; Karam, N. *Progress in Photovoltaics: Research and Applications* **2011**, 19, (7), 797-812.

163. Kunert, B.; Nemeth, I.; Reinhard, S.; Volz, K.; Stolz, W. *Thin Solid Films* **2008**, 517, (1), 140-143.
164. Grassman, T.; Brenner, M.; Rajagopalan, S.; Unocic, R.; Dehoff, R.; Mills, M.; Fraser, H.; Ringel, S. *Applied Physics Letters* **2009**, 94, (23), 232106.
165. Volz, K.; Beyer, A.; Witte, W.; Ohlmann, J.; Németh, I.; Kunert, B.; Stolz, W. *Journal of Crystal Growth* **2011**, 315, (1), 37-47.
166. King, R.; Sherif, R.; Fetzer, C.; Colter, P.; Cotal, H.; Paredes, A.; Edmondson, K.; Law, D.; Stavrides, A.; Yoon, H. In *Advances in high-efficiency multijunction terrestrial concentrator cells and receivers*, Proceedings NCPV and Solar program review meeting, Denver (CO), USA, 2003; pp 211-214.
167. Silvaco ATLAS user's manual.
168. Deutsch, T. G.; Koval, C. A.; Turner, J. A. *The Journal of Physical Chemistry B* **2006**, 110, (50), 25297-25307.
169. Fahy, S.; Lindsay, A.; O'Reilly, E. *IEE Proceedings-Optoelectronics* **2004**, 151, (5), 352-356.
170. Kaschner, A.; Lüttgert, T.; Born, H.; Hoffmann, A.; Egorov, A. Y.; Riechert, H. *Applied Physics Letters* **2001**, 78, (10), 1391-1393.
171. Seif, J. P.; Menda, D.; Descoeudres, A.; Barraud, L.; Özdemir, O.; Ballif, C.; De Wolf, S. *Journal of Applied Physics* **2016**, 120, (5), 054501.
172. <https://tel.archives-ouvertes.fr/tel-01078470/>.
173. Harris, C.; Lindsay, A.; O'Reilly, E. *Journal of Physics: Condensed Matter* **2008**, 20, (29), 295211.
174. Lindsay, A.; O'Reilly, E. P. *Physical review letters* **2004**, 93, (19), 196402.
175. Schetzina, J. F., Integrated heterostructures of group III-V nitride semiconductor materials including epitaxial ohmic contact comprising multiple quantum well. Google Patents: 2000.
176. Hori, H.; Tanaka, K.; Oda, Y.; Minemoto, T.; Takakura, H. *Journal of Crystal Growth* **2009**, 311, (3), 727-730.
177. <http://www.ee.sc.edu/personal/faculty/simin/ELCT563/08%20Tunnel%20Diodes.pdf>.

# Shijian WANG

Doctorat : Matériaux, Mécanique, Optique, Nanotechnologie

Année 2019

## Nanostructure métallique en forme de W pour la nano-optique et simulation numérique des cellules solaires tandem sur silicium

Ce travail porte sur deux sujets. La première partie traite d'une structure plasmonique originale basée sur une nouvelle approche de la nanostructuration. La géométrie est décrite comme une couche d'or « pliée » en forme de « W ». Nous l'appelons Origami à cause des mots japonais : 'ori', plier ; « Gami », papier. Les structures sont fabriquées pour une couche d'or de 50 nm d'épaisseur avec une périodicité de 400 à 1000 nm à partir de matrice de silicium. La complexité et l'originalité de la réponse proviennent de la présence d'ondulations régulières avec des facteurs d'exaltation de champ locaux élevés qui peuvent être couplées à un mode de chaîne plasmonique. Les résultats de mesure optique et de simulation sont en bon accord. La deuxième partie traite de la simulation numérique de cellules solaires tandem III-V / Si constituées d'une couche active de GaAsPN. Ce type de cellule solaire possède un rendement théorique élevé et un faible coût. Le travail principal est axé sur l'étude de la couche supérieure de la cellule solaire en raison de la parfaite maîtrise de la fabrication de la couche inférieure des cellules solaires au Si. Les résultats de simulation garantissent la meilleure épaisseur de couche active et indiquent que les couches graduées peuvent réduire l'effet de décalage de bande existant entre les couches GaAsPN et N-GaP. Nous avons constaté que GaP (n++) / Si (p++) est la meilleure jonction tunnel dans cette configuration."

Mots clés : nanostructures – silicium – or – simulation par ordinateur – résonance plasmonique de surface – cellules solaires organiques – semi-conducteurs, jonctions.

## Metallic Nanostructure W-shaped for Nano-optic and Numerical Simulation of Tandem Solar Cells on Silicon

This work focuses on two subjects. The first part deals with an original plasmonic structure based on a new approach of nanostructuration. The geometry is described as a gold layer <<folded>> into a "W" shape. We named it as Origami because of the Japanese words: 'ori', fold; 'gami', paper. structures are fabricated for a 50-nm thickness gold layer with a periodicity of 400 to 1000 nm based on Silicon matrix. The complexity and originality of the response comes from the presence of regular ripples with high local field enhancement factors that may couple into a plasmonic chain mode. Meanwhile optical measurement and simulation results are in good agreement. The second part deals with Numerical simulation of III-V/Si tandem solar cells consisting of an active layer of GaAsPN. This type of solar cell owns high theoretical efficiency and low cost. The main work focuses on top cell study due to the mature bottom Si solar cell fabrication. Simulation results assure of the best active layer thickness and indicate that graded layers can decrease the band offset effect existing between GaAsPN and N-GaP layers, meanwhile we have found that the GaP(n++)/Si(p++) is the relative better tunnel junction in this configuration.

Keywords: nanostructures – silicon – gold – computer simulation – surface plasmon resonance – tandem solar cell – tunnel junctions.

Thèse réalisée en partenariat entre :

